Structural Dynamics of DNA Hydration Shell Studied by 2D IR and Pump-Probe Technique

Dissertation

Zur Erlangung des akademischen Grades

Dr. rer. nat.

in Fach Chemie

eingereicht an der

Mathematisch-Naturwissenschaftlichen Fakultät

Humboldt-Universität zu Berlin

von

Dipl.-Chem. Yingliang Liu

Präsident der Humboldt-Universität zu Berlin

Prof. Dr.-Ing. Dr. Sabine Kunst

Dekan der Mathematisch-Naturwissenschaftlichen Fakultät

Prof. Dr. Elmar Kulke

Gutachter:

1. Thomas Elsässer
2. Klaus Rademann
3. Kannan Balasubramanian

Eingereicht am. 30th. Mai 2017

Tag der Disputation: 24th. Juli 2017

Acknowledgment

First, I want to thank Prof. Thomas Elsaesser for giving me a chance to study and work in Max-Born-Institute so I can get access to the laboratory and research facilities, and Prof. Klaus Rademann so I can get a degree of Chemistry in Humboldt University of Berlin. Their patience, motivation, and immense knowledge impress me a lot. Guidance from Prof. Elsaesser helped me in all the time of research and writing of this thesis. I could not have imagined having a better advisor and mentor for my Ph.D study.

Secondly, besides my advisers, I also would like to thank Dr. Torsten Siebert for the instruction on the theory and experiment on femtosecond laser, together with the transient 2D IR and pump probe spectroscopy. I want to thank Dr. Eric T. J. Nibbering, Dr. Benjamin P. Fingerhut and Dr. Eva-Maria Brüning for the discussion of the data on the group seminar and other time, it is pretty helpful to understand the physics behind the experimental data. I would like to thank Dr. Micheal Woerner for the discussion with the 2D IR setup. The tough questions and insightful comments from all the people mentioned above is very helpful for me to understand the nature behind the experimental phenomenon. The instruction of Dr. Rene Costard and Dr. Christian Greve to the OPA system is very helpful. Regina and Rene 's helping to turn on the laser system in the morning is a great support and saved me lots of time and efforts. I would like to thank other colleagues in MBI like Dr. Martin Richter, Dr. Ruediger Grunwald, Yicheng Wang, Dr. Jingming Long for their kindly help and discussions.

It is not easy to study abroad here in Berlin for a foreigner from a country with different culture, tradition and language. Kindly help from Torsten, Ms. Alexandra Westin, Dr. Yan Qiao, and Biswajit is a great support when I was sick in the first winter here. The secretary Ms. Claudia Brigel and Ms. Alexandra Westin give me lots of support for the apartment and some paper works in the MBI.

Fourthly, I would like to thank Debo Zhou and Dr. Gaolei Hou's help when I need some documents for the registration in Humboldt University of Berlin in 2014.

Last but not the least, I would like to thank my family: my parents, my brother, uncles and other relatives for supporting me spiritually throughout writing this thesis and my my life in general.

Thanks and best wishes to all the people mentioned above.

KURZFASSUNG

Biochemische Prozesse treten in wässriger Umgebung auf und Wechselwirkungen der Wasserhülle mit Biomolekülen spielt eine Schlüsselrolle für deren Struktur und Funktion. In dieser Arbeit wird die Strukturdynamik der Wassermoleküle und Gegenionen in der umgebenden Wasserhülle der DNA mit der Methode der zweidimensionalen Infrarotspektroskopie (2D IR) sowie Anrege-Abfrage-Spektroskopie untersucht.

2D IR Spektroskopie ist eine sehr leistungsfähige Technik, mit der man molekulare Kopplungen zwischen verschiedenen Schwingungsmoden sowie strukturelle Fluktuationen der chemischen Umgebung auf einer Femto- bis Pikosekundenskale beobachten kann. In der vorliegenden Arbeit dienen die Schwingungsmoden des DNA-Rückgrats als Sonde, die an der Grenzfläche zwischen DNA und Wasser lokalisiert ist.

Die 2D IR Experimente basieren auf der heterodyn detektierten 3-Puls-Photonecho-Messung, in der die passive Phasenstabilisierung basierend auf diffraktiver Optik angewendet wird, um phasengekoppelte Pulspaare zu generieren. Der Einfluss von Dispersionseffekten in einer Vier-wellen-Mischung Geometrie (FWM) auf das heterodyn detektierte Signal wird im Detail diskutiert. Als Ergebnis wird eine Strategie zur Verbesserung von Zweifarben - und Breitband-2D Experimenten entwickelt.

Für die DNA Rückgrat-Moden von nativer Lachs DNA und kurzer künstlicher doppelsträngiger DNA mit 23 Adnenin-Thymin-Basenpaaren werden eine umfangreiche Anzahl von 2D IR Spektren bei unterschiedlichen Wartezeiten vorgestellt. Der Datensatz umfasst einen breiten Bereich von Hydratisierungsstufen von weniger als 2 Wassermoleküle pro Basenpaar bis hin zu einer vollen Hydratisierung der DNA in einer Flüssigwasserumgebung. Die 2D Spektren der Rückgratschwingungen im Bereich von 900 cm^{-1} bis 1100 cm^{-1} zeigen inhomogen verbreiterte Diagonalbanden, die strukturelle Unordnung und Heterogenität in den hydratisierten Bereichen mit moderater homogener Verbreiterung widerspigeln. Eine 2D Linienformanalyse basierend auf der Dichtematrixtheorie und der Kubo-Näherung für die Frequenz-Fluktuations-Korrelationsfunktion zeigt einen Korrelationsab-

fall von 300 fs gefolgt von einer langsamen Komponente mit einer Abfallzeit von über 10 ps. Die theoretischen Berechnungen reproduzieren den vollständigen 2D Datensatz unter Verwendung dieser zwei Korrelationskomponenten und verschiedenen Fluktuationsamplituden für die unterschiedlichen Moden des Rückgrates.

Die Rückgratmoden zeigen ein reichhaltiges Schema von intermodalen Schwingungskopplungen, was durch die komplexe Struktur von Außerdiagonal-Signalen in den 2D Spektren ersichtlich wird. Die Amplitude der Außerdiagonal-Signalen ändert sich mit ansteigender Wartezeit durch Energieübertragung der Moden bei höherer zu Moden bei niedrigeren Frequenzen und Populationszerfällen. Man erhält intermodale Kopplungen in der Größenordnung von 10 cm^{-1} und Energietübertragunszeiten von etwa 2 ps.

Der Einfluss der Hydratisierung auf die Populationsrelaxation der DNA Rückgratmoden wurden durch ein Anrege-Abfrage Experiment im Bereich von 9-11 μm analysiert. Es zeigt sich, dass die Hydratisierung die Populationsrelaxation der angeregten Zustände der DNA Rückgratmoden begünstigt, was in einer Verkürzung der Pikosekunden-Schwingungslebensdauer resultiert.

Die Antwort des DNA Rückgrats auf die Anregung des Hydratwassers wurde mit Zweifarben-Anrege-Abfrage Experimenten auf der fs-Skala untersucht, in der ein 3 μm Pumppuls OH-Streckoszillatoren in der Wasserhülle anregt und von 9 bis 1.1 μm Abfragepulse die Antwort der Rückgratmoden abbilden. Durch den Vergleich der Ergebnisse für DNA bei verschiedenen Hydratationsstufen können Wasser-DNA-Kopplungen und Zeitskalen des Energietransfers bestimmt werden. Die Sub-Pikosekunden Realaxation der Wasserschwingungen etabliert einen heißen Wasser-Grundzustand auf einer Zeitskala von einigen wenigen Pikosekunden, in der sich die Wassermoleküle leicht umordnen und Wasserstoffbrückenbindungen zwischen Wassermolekülen schwächer werden. Diese Strukturänderung wird auf die DNA Rückgratmoden durch Änderungen des lokalen elektrischen Feldes, das die Wasserhülle auf das Rückgrat ausübt, abgebildet. Infolgedessen zeigen alle Rückgratmoden eine ähnliche Antwort im Pikosekundenbereich auf die Wassererhitzung unabhängig von ihrer lokalen Wasserstoffstruktur. Die Übertragung von Energie aus der erhitzten Wasserhülle in die DNA tritt auf einer langsameren Zeitskala von mehr als 10 ps auf.

Die Ergebnisse der vorliegenden Arbeit zeigt das starke Potenzial von Schwingungsmoden an Grenzflächen für die Abbildung und das Verständnis von Wechselwirkungen zwischen Biomolekülen und ihrer Wasserhülle. In Zukunft soll dieses Konzept auch auf andere Biomoleküle angewendet werden.

Schlüsselwörte: 2D IR Spektroskopie, Anrege-Abfrage Spektroskopie, DNA, Wasserdynamik

ABSTRACT

Biochemical processes occur in an aqueous environment and interactions of the water shell with biomolecules play a key role for their structure and function. In this thesis, the structural dynamics of water molecules and counterions in the hydration shell of DNA is investigated by two-dimensional infrared (2D IR) spectroscopy and pump-probe transient spectroscopy. 2D IR spectroscopy is a powerful technique that can track molecular couplings between different vibrational modes and structural fluctuations of the chemical environment on a femto- to picosecond time scale. In the present study, vibrational modes of the DNA backbone serve as probes located at the DNA-water interface.

The 2D IR experiments are based on heterodyne-detected 3-pulse photon echo measurements in which passive phase stabilization techniques based on diffractive optics are applied to generate phase-locked pulse pairs. The influence of dispersion effects in a four-wave mixing (FWM) geometry on the heterodyne detected signal is discussed in detail. As a result, a strategy for improving on two-color and broadband 2D experiments is developed.

An extensive set of 2D IR spectra at different waiting times is presented for backbone modes of native salmon testes DNA and short artificial DNA double strands containing 23 adenine-thymine base pairs. The data set covers a broad range of hydration levels from less than 2 water molecules per base pair up to full hydration in a liquid water environment. The backbone modes in a range from 900 to 1100 cm^{-1} display inhomogeneously broadened lineshapes of diagonal peaks, reflecting structural disorder and a heterogeneity of hydration sites, and a moderate homogeneous broadening. A 2D lineshape analysis based on density matrix theory and a Kubo approach for the frequency fluctuation correlation functions provides a 300 fs correlation decay, followed by a slow component with a decay time beyond 10 ps. The theoretical calculations reproduce the full 2D data set with these two correlation components and different fluctuation amplitudes for the different backbone modes.

The backbone modes display a rich scheme of intermode vibrational couplings as is evident from the complex cross peak patterns in the 2D spectra. The amplitudes of cross peaks change with increasing waiting times, due to energy transfer from the modes at higher to modes at lower frequencies

and population decays. One derives intermode couplings on the order of 10 cm^{-1} and energy transfer times of some 2 ps.

The influence of hydration on the population relaxation of DNA backbone modes is analyzed by pump-probe experiment in 9 to 11 μm region. It is found that hydration facilitates the population relaxation of the excited states of DNA backbone modes, resulting in a shortening of the picosecond vibrational lifetimes.

The response of the DNA backbone to excitation of the hydration water is investigated in femtosecond two-color pump-probe experiments where a 3 μm pump pulse excites OH stretch oscillators in the water shell and 9 to 11 μm probe pulses map the response of the backbone modes. By comparing results for DNA at different hydration levels, water-DNA couplings and time scales of energy transfer are determined. The subpicosecond relaxation of water vibrations establishes a hot water ground state on a time scale of a few picoseconds, in which water molecules slightly rearrange and hydrogen bonds between water molecules are weakened. This structure change is mapped onto the DNA backbone modes by changes in the local electric field the water shell exerts on the backbone. As a result, all backbone modes show a similar picosecond response to water heating, independent of their local hydrogen patterns. Energy transfer from the heated water shell into DNA occurs on a slower time scale of tens of picoseconds.

The results of this thesis demonstrate the strong potential of interfacial vibrational modes for mapping and understanding interactions between biomolecules and their water shell. In future, this concept will be applied to other biomolecular systems.

Keywords: 2D IR spectroscopy, Pump-probe spectroscopy, DNA, Water dynamics

CONTENTS

List of Abbreviations

2D IR	Two Dimensional Infrared
b.p.	Base Pair
CTMA	Cetyltrimethylammonium
CLS	Center Line Slope
DC	Direct Current
DFG	Difference Frequency Generation
DOPC	1,2-dioleoyl-sn- glycero-3-phosphocholine
EXISD	Excitation Transfer Induced Spectral Diffusion
ESA	Excited States Absorption
ESE	Excited States Emission
FFCF	Frequency Fluctuation Correlation Function
FT IR	Fourier Transform Infrared
FWHM	Full Width at Half Maximum
FWM	Four Wave Mixing
LO	Local Oscillator
GSB	Ground States Bleach
OPA	Optical Parametric Amplifier
OPCPA	Optical Parametric Chirped Pulse Amplification
PES	Potential Energy Surface
PED	Potential Energy Distribution
POPC	1-palmitoyl-2-oleoyl-sn-glycero-3-phosphocholine
r.h.	Relative Humility
THF	Tetrahydrofuran
TDSE	Time-Dependent Schrödinger Equation
TISE	Time-Independent Schrödinger Equation

LIST OF FIGURES

LIST OF TABLES

1. INTRODUCTION

Deoxyribonucleic acid (DNA) is the carrier of genetic information for life. Its structure was first proposed by James Watson and Francis Crick in 1953,[1] based on X-ray diffraction data from Rosalind E. Franklin.[2] DNA consists of two strands coiled around each other, thus forming a double helix. The DNA structure consists of two deoxyribose-phosphodiester backbone strands and hydrogen-bonded base pairs. There are four kinds of different bases in DNA: adenine (A), thymine (T), guanine (G), and cytosine (C), forming AT and GC pairs as shown in Figure 1.1. The sequence of base pairs along the DNA helix encodes the genetic information.

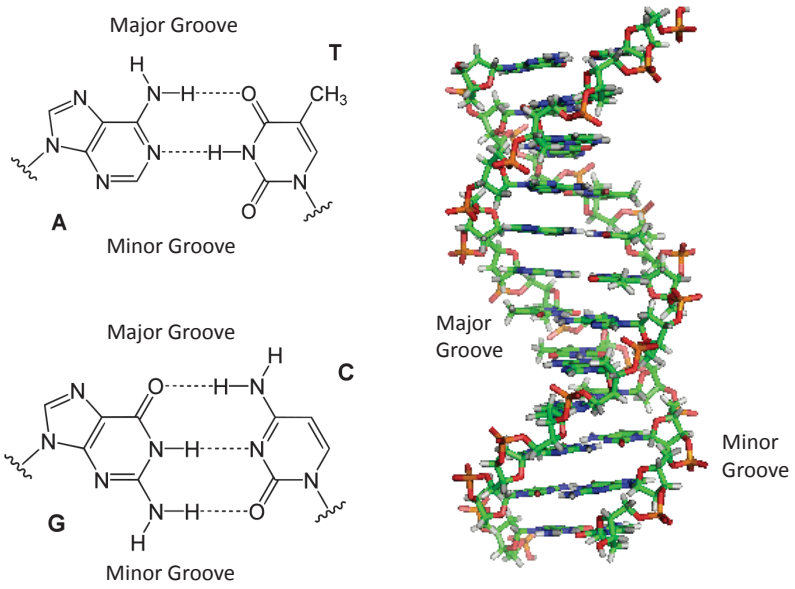

Fig. 1.1: Base pairs in DNA and minor and major grooves

As a result of the particular geometry of the glycosidic bonds linking the nucleic bases and the sugar rings in the backbone strands, the double helix structure displays a wide major and a narrow minor groove as shown in Figure 1.1. Due to the presence of the negatively charged phosphate groups, the minor groove is more hydrophilic than the major groove.

1.1 Conformation of DNA

As a result of the flexibility of the backbone, DNA can take different conformations, as indicated in Figure 1.2. The water concentration in the environment of the double helix strongly influences the occurrence of different conformations. At a high water level, DNA tends to assume the B conformation. When the water concentration decreases, DNA will change to the A or Z conformation. Both A and B DNA belong to the right-handed helices, while Z DNA is a left-handed helix. A significant difference between A, B and Z DNA is their diameter: A DNA, 2.3 nm; B DNA, 2.0 nm; Z DNA, 1.8 nm. The rise per base pair (b.p.) for A DNA is 0.26 nm, which is shorter than the value of 0.34 nm for B DNA. In biological systems, the hydration water is removed when DNA interacts with certain types of protein. As a result, it tends to assume the A conformation. It was revealed that A conformation of DNA plays a role in the protection mechanism of the DNA double helix and predominates in the most adverse environments, like high temperature (80 °C) and low pH values (pH=3)[3] or in an extremely dry environment.[4] It has also been proposed that the transition between A DNA and B DNA may drive the genome into capsids of a virus.[5] Z DNA is believed to provide torsional strain relief that facilitates DNA transcription to RNA.[6]

The five-membered sugar rings are nonplanar and display a different puckering in A and B DNA.In A DNA, the sugar units take a C3′-*endo* conformation, while a C2′-*endo* conformation is assumed in B-DNA. The latter case makes the 5′ and 3′ hydroxyl groups separated further apart than in the C2′-endo conformation. The distance between neighboring phosphate groups is enlarged by about 0.1 nm when changing from A to B conformation. The shortest distance between free phosphate oxygen atoms changes from 0.54 nm to 0.66 nm.[7] So, in A DNA, one water molecule can bridge the neighboring phosphate groups. In other words, the neighboring phosphate groups share one water molecule in the first hydration layer of A DNA. But as a result of the larger distance, it is impossible for one water molecule bridging them in B DNA. In other words, neighboring phosphate groups in B DNA are hydrated separately.

There are several microscopic interactions that determine the conformation of DNA, in particularly Coulomb interactions between the negatively charged phosphate groups and with counterions and water dipoles in the environment, as well as hydrogen bonds interaction with water.[8] It was found that the solvent polarity has a great influence on DNA conformation.[9, 10] In the simulation work of B. Gu and coworkers, they modified water molecules with a scaled charge to investigate the influence of solvent polarity on DNA conformation.[9] They discovered that DNA will change from B

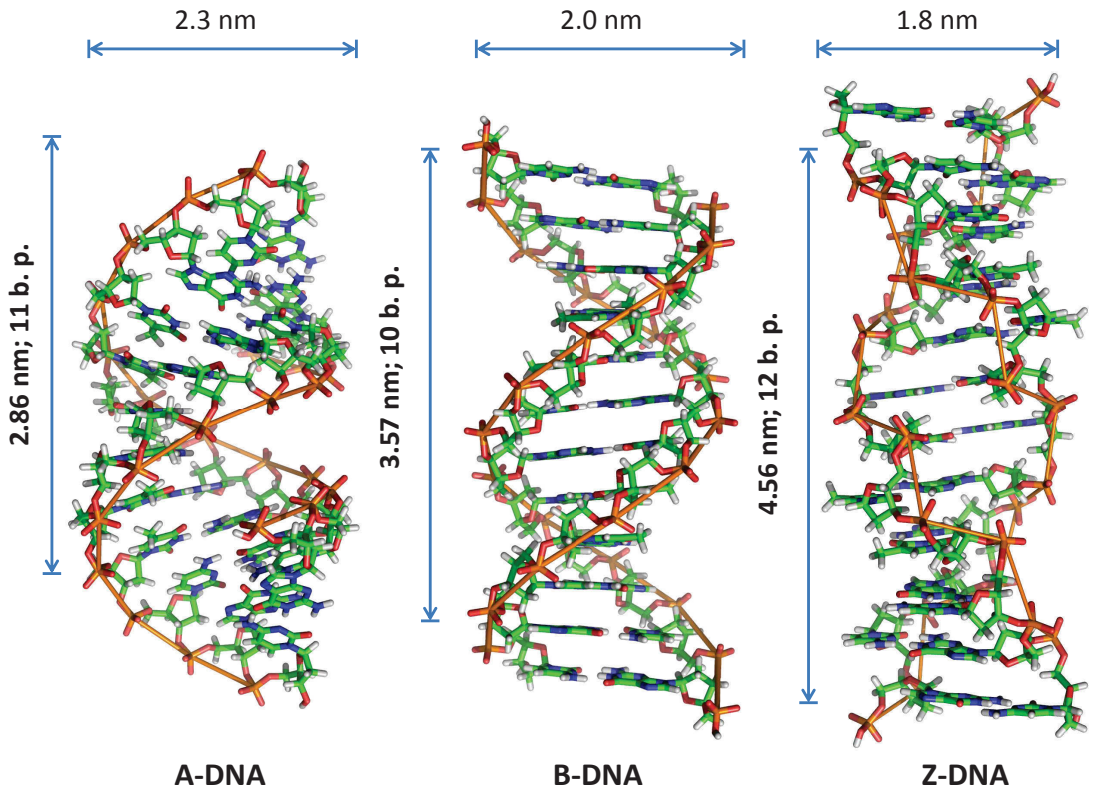

Fig. 1.2: Side view of A-, B-, and Z-DNA, from Wikipedia: The Free Encyclopedia.

conformation to A-B mixed and then A conformation when the polarity of water molecule decreases from normally polarized to less polarized. A. Yildrim and coworkers found that an environment with a reduced dielectric constant favors the occurrence of A relative to B DNA.[10]

1.2 Hydration of DNA

Gravimetric measurements give the weight of water absorbed by a thin DNA film exposed to an atmosphere with a defined relative humidity (r.h.). Falk et al. found that DNA is hydrated with more than 20 water molecules per base pair (b.p.) at 92% r.h.[11]

Numerous X-ray and neutron diffraction experiments have addressed the hydration structure of DNA.[12, 13, 14, 15, 16] Different groups at the DNA surface have different affinity with water molecules, with the negatively charged free phosphate oxygen atoms O1′ and O2′ being the strongest hydrogen-bonding acceptors in DNA. They can form intermolecular hydrogen bonds[17] with up to 6 hydrating water molecules. It is very hard to remove the hydration water from the phosphate groups

totally. The hydrophilic oxo groups of purine and pyrimidine have the next highest affinity, followed by the nitrogen atom N in the base.[18] Then comes the oxygen atom O4′ of the furanose ring. The other atoms like phosphate ester oxygen O3′ and O5′ belong to the weakest hydrogen-bonding acceptors in DNA.[12, 18, 19]

The hydration water in the minor and major grooves has an unusual structure. A chain-like arrangement of water molecules, the so-called spine of water, exists in the minor groove of B DNA. The precise structure of hydration pattern in the minor groove of B DNA is related to the groove width. Wide minor grooves contain two water ribbons, while narrow grooves one hydration spine. The water in the hydration spine alternatively bridge base pairs and phosphate groups. A hexagonal hydration network was observed in the minor groove of the AT-tract sequence, and the hydration water molecules in the first hydration shell make well ordered interstrand bridges.[16]

X-ray data suggest that the major groove of B DNA AATT region have four interconnected parallel water ribbons, following the sugar backbone direction in the first hydration shell.[15] In this network, six and seven numbered rings of water molecules were observed. In B DNA, water molecules solvating neighboring phosphate groups can be linked through second layer water molecules.[19] This is quite different from the case of A and Z DNA, where the first hydration shell water molecules frequently bridge anionic phosphate oxygen atoms of neighboring residues.

In the hydration shell of DNA, the counterions condense on the DNA surface to neutralizeng the negative charge of the phosphate groups. Different types of calculations have been carried out to investigate the distribution of counterions around DNA, including molecular dynamics simulation and Poisson-Boltzmann calculations.[20, 21, 22] A fraction of some 75% of the counterions are located at radial distances of less than 20 Å from the axis of the DNA helix. The adsorption pattern on the DNA surface is highly dependent on the local geometric shape. A minor fraction of counterions is located in the minor and major grooves while their majority is part of a counterion atmosphere in the water shell.

X-ray diffraction results for DNA crystals suggest that the counterions interact with DNA most frequently via water in their first hydration shell, while a direct-ion DNA contact is very rare for the case of hard ions like Mg^{2+} and Ca^{2+}.[23, 24] The average distance between Mg^{2+} and phosphate oxygen is found to be 2.03 Å.[23] The counterion distribution around DNA in solution was studied by L. Pollack and coworkers using small-angle x-ray scattering.[25] They found that the condensed monovalent counterion layer is two times thicker than the divalent counterion atmosphere and derived

screening lengths of 4.9 and 2.9 Å for single and double charged counterions.

When the radius of the counterions is increased, more counterions will go into the major groove, while the ion occupation will decrease in the minor groove. It was also confirmed that the diameter of the counter ions also has an influence on the stability of DNA double helix. The melting temperature of DNA double helix decreases as the increase of the cation radius.[26] This is because large cations are less effective at the charged phosphate groups in B DNA for that they cannot approach the negatively charged phosphate groups as close as the small ones.

1.3 Structural dynamics of DNA hydration

The highly heterogeneous structure of the DNA surface is reflected in highly heterogeneous dynamics of hydrating water, covering a very broad range in time. The fastest librational motions of individual water molecules in the first few water layers occur in the femtosecond time domain while slow motions of water molecules in the minor groove extend to hundreds of picoseconds. Water dynamics at the DNA surface and in the first few water layers has been studied by numerous experimental methods, including dielectric spectroscopy, different types of nuclear magnetic resonance, and steady-state terahertz spectroscopy. In the following, methods that can grasp processes at a femto- to picosecond time scale are discussed briefly.

Dielectric relaxation spectroscopy (DRS) has been applied to study the structural dynamics of water.[27] The dynamics of water has been derived from the frequency dependent complex dielectric constant

$$\hat{\varepsilon}(\nu) = \varepsilon'(\nu) - i\varepsilon''(\nu) \tag{1.1}$$

In an elementary approach, the frequency dependence of ε' and ε'' is analyzed by a Debye model to get the dynamics of collective, diffusion, and reorientation motion of solvent molecules. According to the Debye model, the complex dielectric response is given by

$$\hat{\varepsilon}(\nu) = \varepsilon_\infty + \sum_{j=1}^{n} \frac{S_j}{1 + i2\pi\nu\tau_j} \tag{1.2}$$

Here, ε_∞ is dielectric constant at high frequency; τ_j is relaxation time for j-th degree of freedom and S_j is the magnitude of induced polarization. A recent dielectric relaxation study of the hydration dynamics of natural DNA provided relaxation times of the hydration shell not much different from bulk water.[28] However, the concentration of DNA base pair used there was only 2 mM (≈1.3 mg/ml), i.e., more than 27000 water molecules per base pair, most of them not interacting with DNA.

A trend of increasing of τ_1 from 9.4 ps to 9.7 ps has been derived from data for high-concentration samples when the concentration of DNA is increased from 0.5 mg/ml to 20 mg/ml.[29] Up to now, no dielectric relaxation study has been carried out for the close hydration layer of DNA.

Time-resolved Stocks shift (TRSS) experiments apply chromophores attached to or incorporated in the DNA double helix as probes of water dynamics.[30, 31] Electronic excitation of the chromophore results in a change of its dipole moment, to which the surrounding water responds by reorientation processes in order to minimize the solvation energy of the excited-state dipole. Water reorientation is followed in time by measuring the momentary spectral position of emission from the S_1 state, i.e. the transient Stokes shift of emission relative to the initial position of the S_0–S_1 transition. This concept has been implemented by inducing stimulated emission from the S_1 state with a probe pulse or by time-resolved detection of fluorescence. In the regime of linear response, the normalized time-dependent Stokes shift is proportional to the frequency fluctuation correlation function of the water shell.[32, 33]

TRSS experiments have been interpreted in terms of a substantial slowing down of water dynamics with kinetic components extending into the regime of a few nanoseconds. Such conclusions are highly controversial and, in particular, inconsistent with NMR work and theory, both suggesting a much more limited slowing-down compared to bulk water. Central issues of the TRSS approach are the invasive character of the chromophores, which changes the genuine hydration structure around DNA, and the sensitivity of the Stokes shift to other mechanisms, e.g., the structural dynamics of the biomolecule itself.

Several experiments in the mid-infrared (MIR) region have been implemented to study vibrational dynamics of DNA and its water shell. A two-color pump-probe experiment has been carried out to investigate the coupling between the NH stretching modes of DNA bases and the anti-symmetric phosphate stretching mode of DNA backbone.[34] It was discovered that the NH stretching mode of DNA bases and antisymmetric phosphate stretching mode is coupled excitonically. Besides, the water shell around the phosphate groups was found to serve as a heat sink for excessive vibrational energy.

In the past 20 years, 2D IR spectroscopy has emerged as a powerful technique to investigate the structural dynamics of molecules in the condensed phase.[35] This nonlinear method allows for identifying correlations and couplings between vibrational excitations, including processes of population transfer. The lineshape of the nonlinear signals gives insight into spectral diffusion processes caused by fluctuating forces from the environment and the predominant line broadening mechanisms. The

time resolution of 2D IR experiments can be on the order of 100 fs, orders of magnitude higher than of multidimensional NMR techniques.

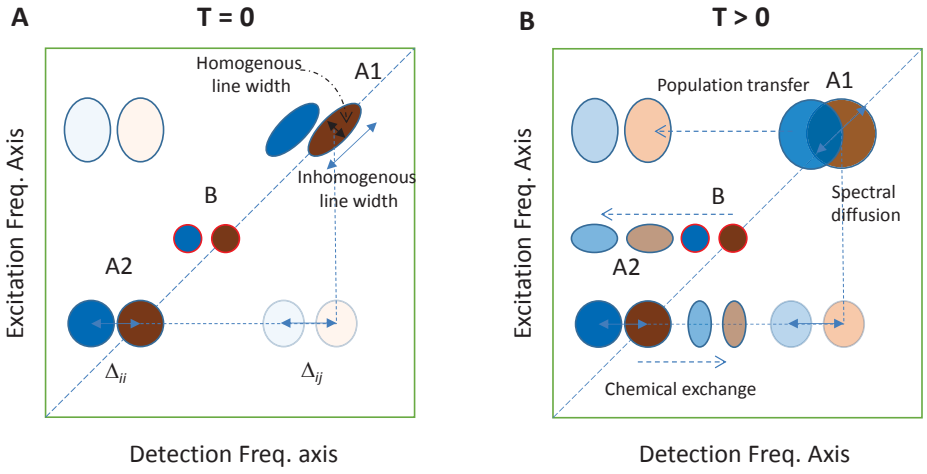

Fig. 1.3: Schematic illustration of the information in 2D IR spectra. (A) At T = 0, Correlation spectrum reveals homogeneous and inhomogeneous linewidths of the diagonal peak pairs, and off-diagonal cross peak pairs from excitonic coupling between related vibrators. (B) At T > 0, the broadening of the peaks in the diagonal direction reflects spectral diffusion. The growth of the cross peaks is from population transfer or chemical exchange.

Several 2D IR experiments have been performed on the structural dynamics of water around DNA at different hydration levels by using NH and OH stretching modes of DNA and hydration water as probes. Fluctuating thermal motions of the dipolar water molecules generate a fluctuating electric force which gives rise to spectral diffusion of vibrational excitations, both of DNA and water molecules. The dynamics of spectral diffusion in the hydrated DNA system is moderately slowed down compared to the case of pure water.[36, 37] For OH stretch excitations, resonant energy transfer between water molecules makes an additional contribution to spectral diffusion which is difficult to discern from structure fluctuations. More importantly, the 2D spectra of OH stretch excitations are not spatially selective as water molecules close to and far away from the DNA contribute to the spectra, representing an ensemble average. Thus, there is substantial interest in finding and demonstrating other vibrational probes, preferably those located at the DNA-water interface. This issue is addressed in this thesis by using DNA backbone modes as probes.

In parallel to the extensive experimental work, theory and simulation have dealt with hydration of biomolecules. Water dynamics in the DNA grooves has been studied through hydrogen bond lifetimes and orientational relaxation in atomistic molecular dynamics simulations.[38] Water dynamics are

slowed down in both major and minor grooves compared to bulk water. Furthermore, the average lifetime of hydrogen bonds is much longer in the minor groove than in the major groove. The solvation time correlation function of DNA native bases was deduced from molecular dynamics simulations to understand the TRSS results for DNA.[39] Several processes with time constants from tens of femtoseconds to tens of picoseconds were obtained.

Reorientation dynamics of water molecules in the bulk and close to biomolecules have received strong attention.[40, 41, 42, 43, 44] A. Tokmakoff and coworkers reported a short lived (about 200 fs) nonhydrogen-bonded configuration of water molecules in the bulk liquid, derived from the lineshape of the 2D IR spectra of HOD in D_2O.[45] More recently, the so-called jump mechanism of water reorientation has been introduced as a basic concept by Laage and Hynes.[41] and meanwhile been applied to the hydration water around B DNA.[46] It was found that there is a pronounced distribution of the reorientation times, reflecting the spatial heterogeneity of the DNA-water interface. The simulation work shows that water in the minor groove has the biggest temporal heterogeneity. The results also show that DNA dynamics are not slaved by water. Quite to the opposite, fluctuations of the DNA structure facilitate water motions in the minor groove.

Another important aspect of DNA hydration dynamics are the strong fluctuating electric fields occurring at the DNA-water interface. In general, the phosphate ions in the DNA backbone, the counter ions, and the dipolar water molecules represent sources of electric fields. Although addressed in a number of simulations, there is no consistent picture of the field amplitudes and the frequency spectrum of such fields. From the experimental side, Stark spectroscopy has been performed on particular vibrations to determine frequency shifts of vibrational transitions as a function of an external DC field. Such work has included studies of the asymmetric phosphate stretching vibration.[47]

1.4 Outline of the thesis

Ultrafast processes in hydrated DNA represent the topic of this thesis, which reports results from ultrafast infrared spectroscopy, in particular, 2D IR and pump-probe spectroscopy of DNA backbone modes. Chapter 2 summarizes the theoretical framework for describing anharmonic vibrational oscillators, followed by the time-dependent quantum description of 2D IR spectroscopy. Chapter 3 describes the experimental setup used in 2D IR spectroscopy, including both frequency domain and time domain methods. This includes a discussion of methods for reducing the influence of scattered light on the measured 2D signals. At the end of this chapter, some comments are presented on 2D

setups based on diffractive optics.

Chapter 4 presents the FT-IR spectra of DNA backbone modes at different hydration levels, together with the assignment of the IR peaks in 8 to 11 μm region. A temperature variation FT-IR experiment has been conducted, the data are discussed at the end of this chapter.

Chapters 5 and 6 contain the main body of 2D IR data measured with salmon testes DNA and short artificial double-stranded DNA oligomers in a wide range of hydration levels. The spectra are analyzed using the theoretical framework of Chapter 2 and Kubo lineshape theory. Chapters 7 and 8 are devoted to different types of femtosecond pump-probe studies, addressing vibrational lifetimes and energy exchange between DNA and its hydration shell. Conclusions are presented in Chapter 9.

2. TWO-DIMENSIONAL INFRARED SPECTROSCOPY OF ANHARMONIC VIBRATIONAL OSCILLATORS

In this chapter, the basic quantum-mechanical description of anharmonic molecular oscillators is introduced first, followed by the theoretical framework of 2D IR spectroscopy. The latter is based on density matrix theory treating the nonlinear light-matter interaction on the level of perturbation theory.[48, 49]

The time evolution of a quantum system is described by the time-dependent Schrödinger equation (TDSE):

$$i\hbar\frac{\partial}{\partial t}\psi(\mathbf{r},t) = \hat{H}(\mathbf{r},\mathrm{t})\psi(\mathbf{r},t) \tag{2.1}$$

Here $\hat{H}(\mathbf{r},\mathrm{t})$ is the total Hamiltonian operator containing the kinetic and potential energies plus additional time-dependent terms describing, e.g., the interaction with an external light field, and $\psi(\mathbf{r},t)$ is the total wavefunction of the system.

For a time-independent Hamiltonian $\hat{H} = \hat{H}(\mathbf{r})$, the solution is given by

$$\psi(r,t) = \varphi(r)T(t) \tag{2.2}$$

This ansatz leads to the time-independent Schrödinger equation

$$\hat{H}(\mathbf{r})\varphi(\mathbf{r}) = E\varphi(\mathbf{r}). \tag{2.3}$$

with the energy E of the quantum state described by $\phi(\mathbf{r})$ and the propagation term

$$T(t) = \exp\left(\frac{-iEt}{\hbar}\right) = \exp(-i\omega t) \tag{2.4}$$

2.1 Anharmonic vibrational oscillators

The Born-Oppenheimer (BO) approximation separates the wave function of a molecular system into two parts, the nuclear wavefunction and the electronic wavefunction depending parametrically

on the nuclear coordinates:

$$\Psi_{molecule}(\mathbf{r};\mathbf{R}) = \Psi_{electron}(\mathbf{r};\mathbf{R}) \times \Psi_{nuclear}(\mathbf{R}) \tag{2.5}$$

Here, $\mathbf{r}$ stands for all electron coordinates and $\mathbf{R}$ for all nuclear coordinates. Solving the electronic Schrödinger equation with fixed nucleus coordinates provides the electronic energy $E_e(\mathbf{R})$ at this specific nucleus coordinate:

$$\hat{H}_e\psi_e(\mathbf{r};\mathbf{R}) = \left\{-\frac{\hbar^2}{2m_e}\sum_i \nabla_i^2 - \sum_{A,i}\frac{Z_A e^2}{r_{Ai}} + \sum_{i>j}\frac{e^2}{r_{ij}}\right\}\psi_e(\mathbf{r};\mathbf{R}) = E_e(\mathbf{R})\psi_e(\mathbf{r};\mathbf{R}) \tag{2.6}$$

The potential energy surface (PES) function $V_e(R)$ is constructed by combining the electronic energy $E_e(\mathbf{R})$ with the repulsive Coulomb energy between the atomic nuclei:

$$V_e(\mathbf{R}) = E_e(\mathbf{R}) + \frac{1}{2}\sum_{A=1}^{N}\sum_{B=1,B\neq A}^{N}\frac{e^2}{4\pi\epsilon_0}\frac{Z_A Z_B}{R_{AB}} \tag{2.7}$$

The Schrödinger equation for the nuclear wavefunctions then reads as

$$\hat{H}_N\psi_N(\mathbf{R}) = \left(\hat{T}_N + \hat{V}_e\right)\psi_N(\mathbf{R}) = E_{tot}\psi_N(\mathbf{R}) \tag{2.8}$$

In the following, we use mass-weighted Cartesian coordinates $q_1 = \sqrt{m_1}x_1$, $q_2 = \sqrt{m_1}y_1$, $q_3 = \sqrt{m_1}z_1$, etc. and rewrite the PES function in the form of $V_e(\mathbf{q})$. At any point on the PES, the PES function can be expanded into the Taylor series

$$\begin{aligned} V_e(\mathbf{q}) = V_e(\mathbf{q}_0) &+ \sum_{i=1}^{3N}\frac{\partial V_e(q_1,\cdots,q_{3N})}{\partial q_i}(q_i - q_0) \\ &+ \frac{1}{2!}\sum_{i=1}^{3N}\sum_{j=1}^{3N}\frac{\partial^2 V_e(q_1,\cdots,q_{3N})}{\partial q_i \partial q_j}(q_i - q_{i0})\left(q_j - q_{j0}\right) \\ &+ \frac{1}{3!}\sum_{i=1}^{3N}\sum_{j=1}^{3N}\sum_{k=1}^{3N}\frac{\partial^3 V_e(q_1,\cdots,q_{3N})}{\partial q_i \partial q_j \partial q_k}(q_i - q_{i0})\left(q_j - q_{j0}\right)(q_k - q_{k0}) + \cdots \end{aligned} \tag{2.9}$$

At minima on the PES, there is no force action on the nuclei and the first derivatives are zero. The second derivatives determine the force constants of the vibrations. In the harmonic approximation, the second derivatives are used to solve the nuclear Schrödinger equation of the nuclei motion. The second derivatives can be written in form of a matrix called the Hessian:

$$\textbf{Hessian} = \begin{pmatrix} \frac{\partial^2 V}{\partial q_1 q_1} & \frac{\partial^2 V}{\partial q_1 q_2} & \cdots & \frac{\partial^2 V}{\partial q_1 q_{3N}} \\ \frac{\partial^2 V}{\partial q_2 q_1} & \frac{\partial^2 V}{\partial q_2 q_2} & \cdots & \frac{\partial^2 V}{\partial q_2 q_{3N}} \\ \vdots & \vdots & \ddots & \vdots \\ \frac{\partial^2 V}{\partial q_{3N} q_1} & \frac{\partial^2 V}{\partial q_{3N} q_2} & \cdots & \frac{\partial^2 V}{\partial q_{3N} q_{3N}} \end{pmatrix} \tag{2.10}$$

The Hessian matrix **H** can be diagonalized by a unitary matrix **U**.

$$\left(\mathbf{U}^T\mathbf{H}\mathbf{U}\right)_{k,l} = \delta_{k,l}\lambda_k \tag{2.11}$$

Here, one obtains the eigenvalues λ_k. For molecules consisting of n atoms in a non-linear arrangement, 3n-6 of the eigenvalues will be nonzero, while for linear molecules, 3n-5. The left zero eigenvalues of Hessian matrix **H** have eigenvectors describing the translation and rotation of the molecule as a whole. They are zero for the reason that there is no change to the PES when the molecule rotates or translates. Multiplying **U** from the left sides of equation 2.11, we will have

$$\sum_{\mathrm{l}} \mathbf{H}_{\mathrm{k,l}}\mathbf{U}_{\mathrm{l,m}} = \lambda_m \mathbf{U}_{k,m} \tag{2.12}$$

Then we will have the normal modes,

$$Q_m = \sum_k U^T_{m,k} q_k \tag{2.13}$$

From the eigenvalue λ_m, the vibration frequency of Q_m is obtained by

$$\nu_m = \frac{\sqrt{\lambda_m}}{2\pi} \tag{2.14}$$

The discrete energy levels of harmonic normal modes are equally spaced with $\Delta n = \pm 1$ as the selection rule for electric dipole transitions.

In general, the vibration potential is anharmonic and can be written in the normal mode basis as follows:

$$\begin{aligned} V(\mathbf{Q}) = V_0 + &\sum_{i=1}^{N}\left(\frac{\partial V}{\partial Q_i}\right)_0 Q_i + \frac{1}{2!}\sum_{i=1}^{N}\sum_{j=1}^{N}\left(\frac{\partial^2 V}{\partial Q_i \partial Q_j}\right) Q_i Q_j \\ &+ \frac{1}{3!}\sum_{i=1}^{N}\sum_{j=1}^{N}\sum_{k=1}^{N}\left(\frac{\partial^3 V}{\partial Q_i \partial Q_j \partial Q_k}\right) Q_i Q_j Q_k \\ &+ \frac{1}{4!}\sum_{i=1}^{N}\sum_{j=1}^{N}\sum_{k=1}^{N}\sum_{l=1}^{N}\left(\frac{\partial^4 V}{\partial Q_i \partial Q_j \partial Q_k \partial Q_l}\right) Q_i Q_j Q_k Q_l + \cdots \end{aligned} \tag{2.15}$$

Here, N=3n-5 for linear molecules and N=3n-6 for molecules of arbitrary shape. For normal modes, the third term consists of nonzero components with $i = j$.

The theory of quantum mechanical anharmonic oscillators can be solved by a second order perturbative treatment and the potential expansion of Eq. 2.15 up to the quartic force constant.[50] The total vibrational energy is then given by

$$E = E_0 + \hbar\sum_{i=1}^{N}\omega_i\left(n_i + \frac{1}{2}\right) + \hbar\sum_{i\le j}^{N} x_{ij}\left(n_i + \frac{1}{2}\right)\left(n_j + \frac{1}{2}\right) + \cdots \tag{2.16}$$

Here, ω_i is the i^{th} harmonic frequency. The anharmonic constants x_{ii} and x_{ij} are given by

$$-2x_{ii} = \frac{1}{8}\left[-\Phi_{iiii} + \frac{5\Phi_{iiii}^2}{3\omega_i} + \sum k \neq i \frac{\Phi_{ijk}^2\left(8\omega_i^2 - 3\omega_k^2\right)}{\omega_k\left(4\omega_i^2 - \omega_k^2\right)}\right] \tag{2.17}$$

$$\begin{aligned} -x_{ij} = \frac{1}{4}\Bigg(&-\Phi_{iijj} + \frac{\Phi_{iii}\Phi_{ijj}}{\omega_i} + \frac{\Phi_{jjj}\Phi_{iij}}{\omega_j} + \frac{2\Phi_{iij}^2\omega_i}{4\omega_i^2 - \omega_j^2} - \frac{2\Phi_{jji}^2\omega_j}{4\omega_j^2 - \omega_i^2}\Bigg) \\ &+ \frac{1}{4}\sum_{k\neq j\neq i}\left[\frac{\Phi_{iik}\Phi_{jjk}}{\omega_k} - \frac{2\Phi_{ijk}^2\left(\omega_i^2 + \omega_j^2 + \omega_k^2\right)\omega_k}{\omega_i^4 + \omega_j^4 + \omega_k^4 - 2\left(\omega_i^2\omega_j^2 + \omega_i^2\omega_k^2 + \omega_j^2\omega_k^2\right)}\right] \end{aligned} \tag{2.18}$$

Here the cubic Φ_{iii} and quatic Φ_{iiii} force field constants in Eq. 2.17 and 2.18 are the 3rd and 4th derivatives of the PES with respect to the normal modes.

2.2 Density matrix description of 2D IR spectroscopy

The dipole approximation represents the most basic approach to describe the interaction of matter with a classical optical field:

$$\hat{V}(t) = -\hat{\mu} \cdot E(t) \tag{2.19}$$

Here, the quantity $\hat{\mu}$ represents the (induced) transition dipole between two quantum states and $E(t)$ the optical field. The time-dependent electric field results in a time-dependent total Hamiltonian

$$\hat{H} = \hat{H}_0 + V(t) \tag{2.20}$$

Here $\hat{H}_0$ is the Hamiltonian of the isolated molecule. The eigenstates $|n\rangle$ of $\hat{H}_0$ are obtained by solving the time-independent Schrödinger equation.

For external optical fields much weaker than the intramolecular fields, i.e., in the regime of non-perturbative light-matter interaction, the dipole interaction term is small compared to the energies of the optically coupled quantum states and, thus, can be treated in time-dependent perturbation theory.

So far, we have considered a single molecule interacting with light and used a description based on pure quantum states. In our experiments, however, large molecular ensembles are studied for which case pure quantum states cannot be calculated. Instead, density matrix theory is applied to determine ensemble-averaged quantities.

2.2.1 Density matrix and interaction picture

The density matrix is defined as following:

$$\rho = \overline{|\psi\rangle\langle\psi|} \tag{2.21}$$

The bar stands for taking the ensemble average. The time evolution of the density matrix is described by the Liouville-von-Neumann equation

$$\frac{d}{dt}\rho = -\frac{i}{\hbar}\hat{H}|\psi\rangle\langle\psi| + \frac{i}{\hbar}|\psi\rangle\langle\psi|\hat{H} = -\frac{i}{\hbar}\hat{H}\rho + \frac{i}{\hbar}\rho\hat{H} = -\frac{i}{\hbar}\left[\hat{H},\rho\right] \tag{2.22}$$

where $\hat{H}$ is the total Hamiltonian of the system.

The Hamiltonian of the molecular ensemble interacting with light can be divided into two parts. The first time-independent part describes the molecule itself and the second time-dependent part the interaction between the time-dependent light field and the molecule system.

$$\hat{H}(t) = \hat{H}_0 + \hat{H}'(t) \tag{2.23}$$

The time evolution operator of the molecular Hamiltonian $\hat{H}_0$ has the form

$$\hat{U}_0(t,t_0) = e^{-\frac{i}{\hbar}\hat{H}_0\cdot(t-t_0)} \tag{2.24}$$

This allows for defining the wavefunction $\psi_I(t)$ in the interaction picture according to

$$|\psi(t)\rangle \equiv \hat{U}_0(t,t_0)|\psi_I(t)\rangle \tag{2.25}$$

Here, $e^{-\frac{i}{\hbar}\hat{H}_0\cdot(t-t_0)}$ describes the time evolution caused by the system Hamiltonian $\hat{H}_0$ only. The time evolution of $|\psi_I(t)\rangle$ is determined by the weak perturbation $\hat{H}'(t)$. When putting this equation into Schrödinger equation, one obtains

$$\frac{d}{dt}|\psi_I(t)\rangle = -\frac{i}{\hbar}H'_I(t)|\psi_I(t)\rangle \tag{2.26}$$

where the perturbation $H'_I(t)$ is defined as:

$$\hat{H}'_I(t) = e^{\frac{i}{\hbar}\hat{H}_0\cdot(t-t_0)}\hat{H}'(t)\,e^{-\frac{i}{\hbar}\hat{H}_0\cdot(t-t_0)} \tag{2.27}$$

or

$$\hat{H}'_I(t) = \hat{U}_0^{\dagger}(t,t_0)\,\hat{H}'(t)\,\hat{U}_0(t-t_0) \tag{2.28}$$

Integrating Equation 2.26 provides

$$|\psi_I(t)\rangle = |\psi_I(t_0)\rangle - \frac{i}{\hbar}\int_{t_0}^{t} d\tau \hat{H}_I(\tau)|\psi_I(\tau)\rangle \tag{2.29}$$

We can solve this equation iteratively by plugging it into itself:

$$|\psi_I(t)\rangle = |\psi_I(t_0)\rangle + \sum_{n=1}^{\infty}\left(-\frac{i}{\hbar}\right)^n \int_{t_0}^{t} d\tau_n \int_{t_0}^{\tau_n} d\tau_{n-1} \cdots \int_{t_0}^{\tau_2} d\tau_1 \hat{H}'_I(\tau_n) H'_I(\tau_{n-1}) \cdots \hat{H}'_I(\tau_1)|\psi_I(t_0)\rangle \tag{2.30}$$

Substituting $\hat{H}'_I$ with $\hat{H}'$ by using Equation 2.28 gives

$$|\psi(t)\rangle = \left|\psi^{(0)}(t_0)\right\rangle + \sum_{n=1}^{\infty}\left(-\frac{i}{\hbar}\right)^n \int_{t_0}^{t} d\tau_n \int t_0 \tau_{n-1} \cdots \int_{t_0}^{\tau_2} d\tau_1 \hat{U}_0(t,\tau_n) d\hat{H}'(\tau_n) \hat{U}(\tau_n,\tau_{n-1}) \hat{H}'(\tau_{n-1}) \cdots \hat{U}_0(\tau_2,\tau_1) \hat{H}'(\tau_1) \hat{U}_0(\tau_1,t_0)|\psi(t_0)\rangle \tag{2.31}$$

The first term $\left|\psi^{(0)}(t)\right\rangle \equiv \hat{U}_0(t,t_0)|\psi(t_0)\rangle$ is the zero-order wavefunction. Its time evolution is governed by the molecular Hamiltonian $\hat{H}_0$ only. The other terms are perturbative terms that describe the effect of the time-dependent Hamiltonian $\hat{H}'(t)$. They have an intuitive physical interpretation: the system propagates under $\hat{H}_0$ freely until time τ_1. At τ_1, it interacts with the perturbation $\hat{H}'(t)$. Then subsequently, it again propagates freely until the next interaction time τ_2, and so on.

2.2.2 Perturbative expansion of the density matrix

In the last section, we made a perturbative expansion of the eigenfunction of the system in the interaction picture. It can be used for the treatment of pure states but not for a statistical ensemble. The latter requires the density matrix approach for determining the time evolution, i.e., a perturbative expansion of the density matrix in the interaction picture.

We first define the density matrix in the interaction picture:

$$|\psi(t)\rangle\langle\psi(t)| = U_0(t,t_0) \cdot |\psi_I(t)\rangle\langle\psi_I(t)| \cdot U_0^{\dagger}(t,t_0) \tag{2.32}$$

The density matrix obeys the Liouville-von-Neumann equation in the interaction picture:

$$\frac{d}{dt}\rho_I(t) = -\frac{i}{\hbar}\left[H'_I(t), \rho_I(t)\right] \tag{2.33}$$

Its power expansion is as follows:

$$\rho_I(t) = \rho_I(t_0) + \sum_{n=1}^{\infty}\left(-\frac{i}{\hbar}\right)^n \int_{t_0}^{t} d\tau_n \int_{t_0}^{\tau_n} \tau_{n-1} \cdots \int_{t_0}^{\tau_2} d\tau_1 \left[\hat{H}'_I(\tau_n), \left[\hat{H}'_I(\tau_{n-1}), \cdots \left[\hat{H}'_I(\tau_1), \rho_I(t_0)\right] \cdots\right]\right] \tag{2.34}$$

Switching back to the Schrödinger picture gives

$$\begin{aligned}\rho(t) =&\rho^{(0)}(t)+\sum_{n=1}^{\infty}\left(-\frac{i}{\hbar}\right)^{n}\int_{t_0}^{t}d\tau_n\int_{t_0}^{\tau_n}d\tau_{n-1}\cdots\int_{t_0}^{\tau_2}d\tau_1\\ &U(t,t_0)\cdot\left[H'_I(\tau_n),\left[H'_I(\tau_{n-1}),\cdots\left[H'_I(\tau_1),\rho_I(t_0)\right]\cdots\right]\right]U_0^{\dagger}(t,t_0)\end{aligned} \tag{2.35}$$

Here, $\rho(t_0)$ is an equilibrium density matrix. It does not change in time. The perturbation due to light-matter interaction is given by

$$H'(t) = -E(t)\cdot\mu \tag{2.36}$$

and the time evolution of the density matrix by

$$\rho(t) = \rho_{eq}+\sum_{n=1}^{\infty}\rho^{(n)}(t) \tag{2.37}$$

with

$$\begin{aligned}\rho^{(n)}(t) =&-\left(\frac{i}{\hbar}\right)^{n}\int_{-\infty}^{t}d\tau_n\int_{-\infty}^{\tau_n}\cdots\int_{-\infty}^{\tau_2}d\tau_1E(\tau_n)E(\tau_{n-1})\cdot\ldots\cdot E(\tau_1)\cdot\\ &U_0(t.t_0)\left[\mu_I(\tau_n),\left[\mu_I(\tau_{n-1}),\cdots\left[\mu_I(\tau_1),\rho(-\infty)\right]\cdots\right]\right]\cdot U_0^{\dagger}(t.t_0)\end{aligned} \tag{2.38}$$

Here, the dipole operator in the interaction picture is defined as

$$\hat{\mu}_I(t) = U_0^{\dagger}(t,t_0)\hat{\mu}U_0(t,t_0) \tag{2.39}$$

2.2.3 Nonlinear polarization

The macroscopic polarization is given by

$$P(t) = Tr(\hat{\mu}\rho(t)) \equiv \langle\hat{\mu}\rho(t)\rangle \tag{2.40}$$

Using the perturbative expansion of the density matrix and collecting the terms in powers of the electric field $E(t)$, one gets the nth-order polarization

$$\hat{P}^{(n)}(t) = \left\langle\hat{\mu}\rho^{(n)}(t)\right\rangle \tag{2.41}$$

Inserting Eq. 2.38 into Eq. 2.41 results in

$$\begin{aligned}P^{(n)}(t) =&-\left(\frac{i}{\hbar}\right)^{n}\int_{-\infty}^{t}d\tau_n\int_{-\infty}^{\tau_n}\ldots\int_{-\infty}^{\tau_2}d\tau_1E(\tau_n)E(\tau_{n-1})\cdot\ldots\cdot E(\tau_1)\\ &\cdot\langle\mu(t)\left[\mu(\tau_n),\left[\mu(\tau_{n-1}),\ldots\left[\mu_I(\tau_1),\rho(-\infty)\right]\ldots\right]\right]\rangle\end{aligned} \tag{2.42}$$

In a nonlinear experiment, sequences of ultrashort pulses interact with the system. In this scenario, the relative time delays between pulses t_n are relevant rather than the absolute instants in time τ_n. This allows for rewriting Equation 2.42 in the following way:

$$\begin{aligned} P^{(n)}(t) = -\left(\frac{i}{\hbar}\right)^n \int_0^\infty dt_n \int_0^\infty dt_{n-1} \ldots \int_0^\infty dt_1 \\ \cdot E(t-t_n)\, E(t-t_n-t_{n-1}) \cdot \ldots \cdot E(t-t_n-t_{n-1}-\ldots-t_1) \\ \cdot \langle \mu(t_n+t_{n-1}+\ldots+t_1)\,[\mu(t_n+t_{n-1}+\ldots+t_1), \ldots [\mu(0), \rho(-\infty)]\ldots]\rangle \end{aligned} \tag{2.43}$$

For the 3rd order nonlinear response, i.e., an interaction scheme with three subsequent pulses, we have

$$\begin{aligned} &\langle \mu(t_3+t_2+t_1)\,[\mu(t_2+t_1), [\mu(t_1), [\mu(0), \rho(-\infty)]]]\rangle \\ &= \langle \mu(t_3+t_2+t_1)\mu(t_2+t_1)\mu(t_1)\mu(t_0)\rho(-\infty)\rangle && \Rightarrow R_4 \\ &- \langle \mu(t_3+t_2+t_1)\mu(t_2+t_1)\mu(t_1)\rho(-\infty)\mu(t_0)\rangle && \Rightarrow R_1^* \\ &- \langle \mu(t_3+t_2+t_1)\mu(t_2+t_1)\mu(0)\rho(-\infty)\mu(t_1)\rangle && \Rightarrow R_2^* \\ &+ \langle \mu(t_3+t_2+t_1)\mu(t_2+t_1)\rho(-\infty)\mu(0)\mu(t_1)\rangle && \Rightarrow R_3 \\ &- \langle \mu(t_3+t_2+t_1)\mu(t_1)\mu(0)\rho(-\infty)\mu(t_2+t_1)\rangle && \Rightarrow R_3^* \\ &+ \langle \mu(t_3+t_2+t_1)\mu(t_1)\rho(-\infty)\mu(0)\mu(t_2+t_1)\rangle && \Rightarrow R_2 \\ &+ \langle \mu(t_3+t_2+t_1)\mu(0)\rho(-\infty)\mu(t_1)\mu(t_2+t_1)\rangle && \Rightarrow R_1 \\ &- \langle \mu(t_3+t_2+t_1)\rho(-\infty)\mu(0)\mu(t_1)\mu(t_2+t_1)\rangle && \Rightarrow R_4^* \end{aligned} \tag{2.44}$$

These eight terms represent eight possible interaction pathways of the pulses with the molecular system. For an ensemble of 3-level systems with a vibrational ground state v=0, a first excited (v=1) and second excited (v=2) state, the interaction pathways are visualized with the help of the Feynman diagrams in Figure 2.2.

2.3 Kubo′s stochastic theory of line shapes

In the rotation wave approximation (RWA), the response function R_1 can be written as

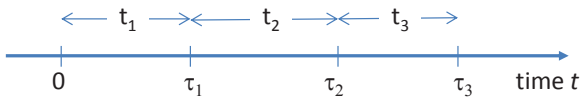

Fig. 2.1: Time variables: the τ is referred to absolute times, and t to time intervals.

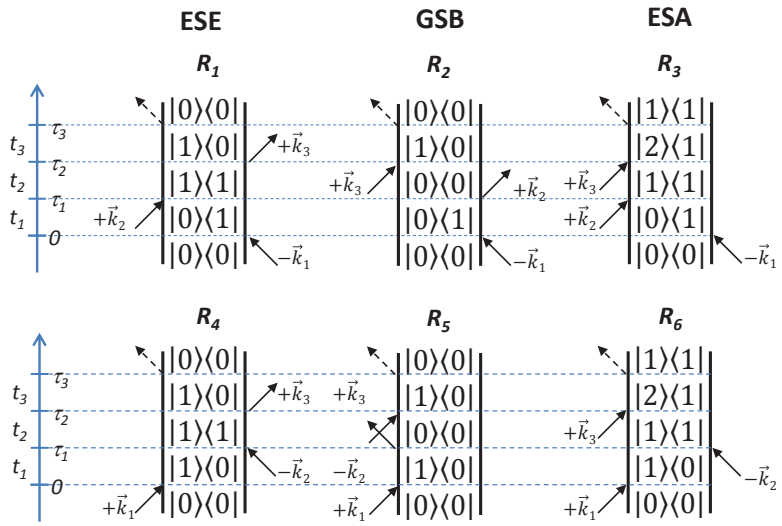

Fig. 2.2: Six Feynman diagrams of the third nonlinear response for 3-level system in rotate wave approximation. R_1, R_1 and R_3 is responsible for the rephasing process, while R_4, R_5 and R_6 for nonrephasing process. R_1 and R_4 are stimulated excited states emission (ESE), R_2 and R_5, ground states bleach (GSB); R_3 and R_6, excited states absorption (ESA).

$$R_1(\tau_3,\tau_2,\tau_1) = -\left(\frac{i}{\hbar}\right)^3 \langle \mu_{01}(\tau_3)\mu_{10}(0)\rho_{00}\mu_{01}(\tau_1)\mu_{10}(\tau_2)\rangle \tag{2.45}$$

Here, $\mu(t)$ is the dipole operator in the interaction picture:

$$\mu(t) = e^{+\frac{i}{\hbar}\hat{H}\cdot t}\mu e^{-\frac{i}{\hbar}\hat{H}\cdot t} \tag{2.46}$$

After expanding $\mu(t)$ in the eigenstate basis of $\hat{H}_0$, we derive for the case of $\mu_{01}(t)$:

$$\mu_{01}(t) = e^{+\frac{i}{\hbar}\varepsilon_0 t}\cdot\mu_{01}\cdot e^{-\frac{i}{\hbar}\varepsilon_1 t} = e^{-\frac{i}{\hbar}(\varepsilon_1-\varepsilon_0)\cdot t}\cdot\mu_{01} \tag{2.47}$$

and for the case of $\mu_{10}(t)$:

$$\mu_{10}(t) = e^{+\frac{i}{\hbar}(\varepsilon_1-\varepsilon_0)\cdot t}\cdot\mu_{10} \tag{2.48}$$

Such expressions allow for rewriting the response functions, e.g., R_1:

$$R_1(\tau_3,\tau_2,\tau_1) = -\left(\frac{i}{\hbar}\right)^3 \mu^4 e^{-i\omega(\tau_3-\tau_2-\tau_1)} \tag{2.49}$$

So far, we have considered an ensemble of noninteracting 3-level systems. In condensed phases, however, the 3-level systems interact with each other and with their surrounding, e.g., a liquid solvent. Kubo theory describes the influence of such interactions by introducing a stochastic modulation of

(optical) transition frequencies by a fluctuating force the 'bath' exerts on a 3-level system. Accordingly, the transition frequency is separated in its time-averaged value and a momentary and fluctuating deviation from the average:

$$\omega(t) = \omega_0 + \delta\omega(t) \tag{2.50}$$

and rewrite Eq. 2.49 into

$$\begin{aligned} R_1(\tau_3,\tau_2,\tau_1) = -\left(\frac{i}{\hbar}\right)^3 \mu^4 e^{-i\omega_0(\tau_3-\tau_2-\tau_1)} \\ \left\langle exp\left[-i\int_0^{\tau_3}\delta\omega(\tau)d\tau + i\int_0^{\tau_2}\delta\omega(\tau)d\tau + i\int_0^{\tau_1}\delta\omega(\tau)d\tau\right]\right\rangle \end{aligned} \tag{2.51}$$

The response function is calculated up to the second order in $\delta\omega$ by applying the cumulant expansion

$$\begin{aligned} \langle\cdots\rangle = 1 &- \frac{1}{2}\int_0^{\tau_3}\int_0^{\tau_3}\langle\delta\omega(\tau'')\delta\omega(\tau')d\tau''d\tau'\rangle - \frac{1}{2}\int_0^{\tau_2}\int_0^{\tau_2}\langle\delta\omega(\tau'')\delta\omega(\tau')d\tau''d\tau'\rangle \\ &- \frac{1}{2}\int_0^{\tau_1}\int_0^{\tau_1}\langle\delta\omega(\tau'')\delta\omega(\tau')d\tau''d\tau'\rangle + \int_0^{\tau_3}\int_0^{\tau_1}\langle\delta\omega(\tau'')\delta\omega(\tau')d\tau''d\tau'\rangle \\ &+ \int_0^{\tau_3}\int_0^{\tau_2}\langle\delta\omega(\tau'')\delta\omega(\tau')d\tau''d\tau'\rangle - \int_0^{\tau_2}\int_0^{\tau_1}\langle\delta\omega(\tau'')\delta\omega(\tau')d\tau''d\tau'\rangle \\ &+ O\left(\delta\omega^3\right) \end{aligned} \tag{2.52}$$

The terms linear in $\delta\omega$ vanish by definition. Introducing so-called lineshape functions,

$$g(t) = \frac{1}{2}\int_0^t\int_0^t d\tau'\tau''\langle\delta\omega(\tau)\delta\omega(\tau'')\rangle + O\left(\delta\omega^3\right) \tag{2.53}$$

We can rewrite this equation in the following form:

$$\langle\cdots\rangle = 1 - g(\tau_3) - g(\tau_2) - g(\tau_1) + h(\tau_3,\tau_1) + h(\tau_3,\tau_2) - h(\tau_2,\tau_1) + O\left(\delta\omega^3\right) \tag{2.54}$$

The functions $h(\tau',\tau)$ contain the same integrand as $g(\tau)$ and are only different by the integration limits, i.e.,

$$h(\tau_2,\tau_1) = g(\tau_2) + g(\tau_1) - g(\tau_2-\tau_1) \tag{2.55}$$

and

$$\langle\cdots\rangle = 1 + g(\tau_3) - g(\tau_2) - g(\tau_1) - g(\tau_3-\tau_1) - g(\tau_3-\tau_2) + g(\tau_2-\tau_1) + O\left(\delta\omega^3\right) \tag{2.56}$$

When we switch back to the time intervals, t_1, t_2 and t_3, we have

$$\langle\cdots\rangle = 1 - g(t_1) - g(t_2) - g(t_3) + g(t_1+t_2) + g(t_2+t_3) - g(t_1+t_2+t_3) + O\left(\delta\omega^3\right) \tag{2.57}$$

We now postulate

$$\langle\cdots\rangle = e^{-f} \tag{2.58}$$

An expansion f in powers of $\delta\omega$ gives the response function in different powers of $\delta\omega$.

$$R_1(t_3,t_2,t_1) = -\left(\frac{i}{\hbar}\right)^3 \mu^4 e^{-i\omega(t_3-t_1)} e^{-g(t_1)+g(t_2)-g(t_3)-g(t_1+t_2)-g(t_2+t_3)+g(t_1+t_2+t_3)} \tag{2.59}$$

Applying this procedure for all response functions of the 3-Level system defined above, the following expressions are derived:

$$\begin{aligned} R^{(3)}_{1,2,3} &= \sum_{n=1}^{3} R^{(3)}_n(t_1,t_2,t_3) \\ &= 2i\mu^4_{01}\left(e^{-i\omega_{01}(t_3-t_1)} - e^{-i((\omega_{01}-\Delta)t_3-\omega_{01}t_1)}\right)\cdot e^{-g(t_1)+g(t_2)-g(t_3)-g(t_1+t_2)-g(t_2+t_3)+g(t_1+t_2+t_3)} \end{aligned} \tag{2.60}$$

$$\begin{aligned} R^{(3)}_{4,5,6} &= \sum_{n=4}^{6} R^{(3)}_n(t_1,t_2,t_3) \\ &= 2i\mu^4_{01}\left(e^{-\omega 01(t_3+t_1)} - e^{-i((\omega_{01}-\Delta)t_3+\omega_{01}t_1)}\right)\cdot e^{-g(t_1)-g(t_2)-g(t_3)+g(t_1+t_2)+g(t_2+t_3)-g(t_1+t_2+t_3)} \end{aligned} \tag{2.61}$$

Here we assume that the transition dipole of $|1\rangle \rightarrow |2\rangle$ transition is $\sqrt{2}$ times of the $|0\rangle \rightarrow |1\rangle$ transition.

In addition to the interaction with the bath, there may be population transfer between different 3-level systems. In the 2D IR spectra, this mechanism leads to off-diagonal or cross peaks. In the simplest approach, population transfer is considered incoherent, i.e., one assumes that any frequency correlation is destroyed by 'jumping' from state A to B. The corresponding response functions are:

$$R^{(3)}_{AB} = i\mu^2_A\mu^2_B\left(e^{-i(\omega_B t_3-\omega_A t_1)} - e^{-i((\omega_B-\Delta)t_3-\omega_A t_1)}\right)\Gamma_{AB}(t_2)\cdot e^{-g(t_1)}e^{-g(t_3)} \tag{2.62}$$

$$R^{(3)}_{BA} = i\mu^2_A\mu^2_B\left(e^{-i(\omega_A t_3-\omega_B t_1)} - e^{-i((\omega_A-\Delta)t_3-\omega_B t_1)}\right)\Gamma_{BA}(t_2)\cdot e^{-g(t_1)}e^{-g(t_3)} \tag{2.63}$$

The equations above describe the time domain response of the ensemble of 3-level systems. By applying a Fourier transformation along t_1 and t_3, one derives the spectral response at a waiting time of t_2 as a function of frequencies ω_1 and ω_3:

$$R^{(3)}_n(\omega_1,t_2,\omega_3) = \int_0^\infty\int_0^\infty R^{(3)}_n(t_1,t_2,t_3)\, e^{-\omega_1 t_1} e^{-\omega_3 t_2} dt_1 dt_3 \tag{2.64}$$

Adding these four terms in the spectral domain, one gets the 2D spectrum at a waiting time of t_2 including population transfer between their first excited states,

$$\begin{aligned} S(\omega_1,t_2,\omega_3) = Re[&\Gamma_{AA}\sum_{n=1}^{6} R^{(3)}_n(\omega_1,t_2,\omega_3) + \Gamma_{BB}\sum_{n=1}^{6} R^{(3)}_n(\omega_1,t_2,\omega_3) \\ &+ \Gamma_{AB}R_{AB}(\omega_1,t_2,\omega_3) + \Gamma_{BA}R_{BA}(\omega_1,t_2,\omega_3)]. \end{aligned} \tag{2.65}$$

The transition rates Γ_{AB}, Γ_{AB}, Γ_{AB} and Γ_{BA} are obtained from a kinetic model of population transfer.

3. EXPERIMENTAL METHODS

The experimental methods applied for studying ultrafast processes in hydrated DNA are summarized in this chapter. After a brief discussion of the generation scheme for tunable femtosecond pulses in the mid-infrared (Mid-IR) spectral range, different approaches of 2D IR spectroscopy are introduced, followed by a description of the setup used in the present experiments. This part is followed by a section on the two-color pump-probe setup and a final part in which optics issues of 2D IR spectroscopy are discussed, in particular in view of future two-color 2D experiments.

3.1 Generation of femtosecond mid-infrared pulses

Mid-IR femtosecond pulses tunable in the 3 to 20 μm region are generated by optical parametric amplification and difference frequency mixing in nonlinear crystals. The generation scheme shown in Figure 3.1 is driven by 800 nm pulses of 60 fs duration from an amplified Ti:sapphire laser system working at a 1 kHz repetition rate. Optical parametric amplification provides near-infrared signal and idler pulses which generate the final long-wavelength output by difference frequency mixing in a second stage.[51] The optical parametric amplifier is based on β-BaB_2O_4 (BBO) in a type-II phase-matching geometry with

$$\omega_{pump} n_{eo}\left(\omega_{pump}, \Theta\right) = \omega_{signal} n_o\left(\omega_{signal}\right) + \omega_{idler} n_{eo}\left(\omega_{idler}, \Theta\right) \tag{3.1}$$

and

$$\omega_{pump} = \omega_{signal} + \omega_{idler}. \tag{3.2}$$

The seeding pulse for optical parametric amplification is derived from a white-light continuum generated by focusing a small portion of the 800 nm pulse into a sapphire plate of a 1 mm thickness. The seed and 10% (about 40 μJ) of the 800 nm pump beam are spatially and temporally overlapped and focused into a 4 mm thick β-BBO crystal. After this first amplification of the seed, a dichroic mirror removes the idler and 800 nm residuals and the signal is amplified for a second time by an

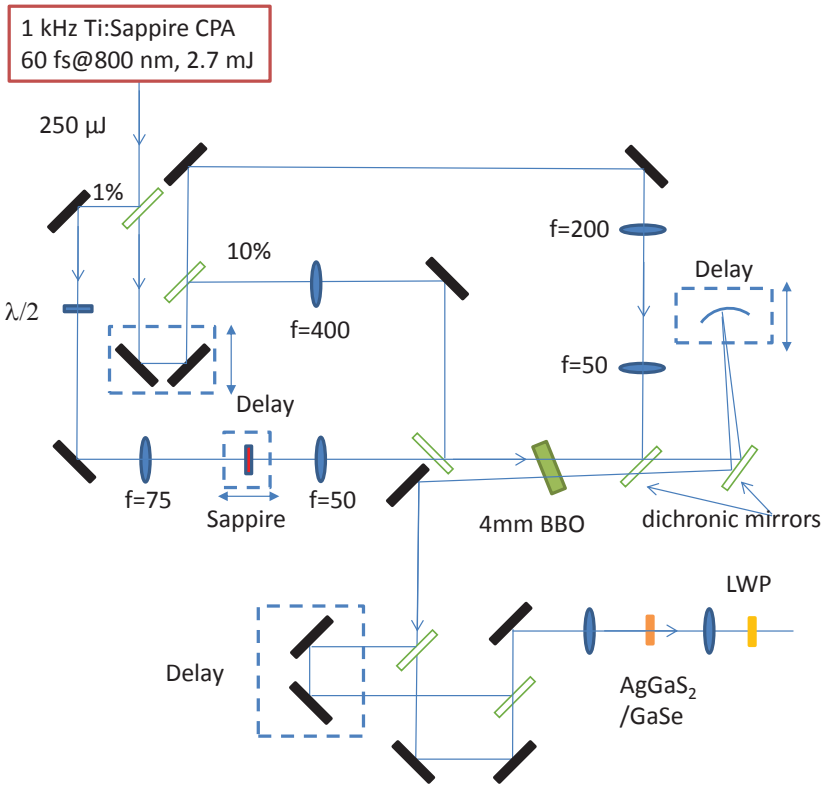

Fig. 3.1: Two-stage OPA and DFG to generate femtosecond MIR pulses

intense pump pulse (200 to 300 μJ) to generate 100 μJ of near-infrared signal and idler output. In the source applied in the 2D IR experiments, an additional β-BBO crystal serves for a third amplification up to a total energy of more than 200 μJ. The near-infrared signal and idler pulses then generate their difference frequency in the final stage, using a 0.75 mm thick GaSe crystal for the 8 to 11 μm wavelength range or a 0.75 mm thick Ag_2GaS_2 crystal for 3 μm pulses. The main parameters of the generated pulses are summarized in Table 3.1.

Tab. 3.1: Parameters of femtosecond pulses used in this work

OPA	DFG Crystal	Center Freq./cm^{-1}	FWHM/cm^{-1}	Pulse Energy/μJ	Duration/fs
Two Stage	0.75 mm Ag_2GaS_2	3450	300	1.6	
	0.75 mm GaSe	1090	140	1.0	150
	0.75 mm GaSe	1000	130	0.6	150
Three Stage	0.75 mm GaSe	1020-1250	200	6-8	120

3.2 Methods of 2D IR spectroscopy

The concept of 2D IR spectroscopy has been inspired by 2D NMR methods. The main difference with the spectrally resolved pump-probe technique consists in introducing a second frequency axis for the excitation frequency information. Key features of 2D IR spectra are the lineshapes of the different diagonal peaks and the occurrence of off-diagonal peaks. The time-dependent lineshapes of the diagonal peaks give insight into spectral diffusion and other line broadening mechanisms while couplings and population transfer between different modes as well as chemical exchange can be retrieved from off-diagonal peaks.

There are mainly two types of 2D IR experiments as illustrated in Figure 3.2.[52] The first approach is based on a pump and probe scheme with tunable narrowband pump pulses and spectrally resolved probing by broadband probe pulses.[35] The spectral narrowing of the pump has been implemented with the help of, e.g., a Fabry-Pérot interferometer which is tuned over the spectrum of the pump pulse. While this method is readily implemented in an experiment, its main disadvantage consists in the temporal broadening of the pump pulse which goes along with the spectral narrowing and, thus, the time resolution is on the order of 1 ps or longer.

In analogy to linear Fourier transform spectroscopy, excitation with a tunable frequency has been implemented with a pair of phase-locked pulses separated by a variable time interval $t_1 = \tau$. This concept which does not compromise the time resolution of the experiment, has been applied in 2D pump-probe schemes with the two phase locked pulses propagating collinearly and a third probe pulse traveling under a small angle.[53, 54] The probe pulse induces the emission of the signal field after a delay T, the waiting or population time, and serves as local oscillator, i.e, the signal and probe field interfere on the time-integrating and spectrally resolving detector.

In 2D photon echo spectroscopy, a sequence of three pulses is applied with a coherence time $t_1 = \tau$ between the first two pulses and the waiting time T between the second and the third pulse. The noncollinear beams $\mathbf{k}_1$, $\mathbf{k}_2$, and $\mathbf{k}_3$ are arranged in a so-called boxcar geometry with the photon-echo signal traveling in the phase-matched direction $\mathbf{-k_1+k_2+k_3}$. For measuring the photon echo signal in amplitude and (relative) phase, it is heterodyned with a fourth pulse traveling in the same direction as the signal. This fourth pulse has a fixed optical phase relative to the third pulse. Spectral interferometry and spectrally resolved detection with a monochromator in conjunction with an array detector is a convenient method for a frequency-resolved detection of the photon echo signal.

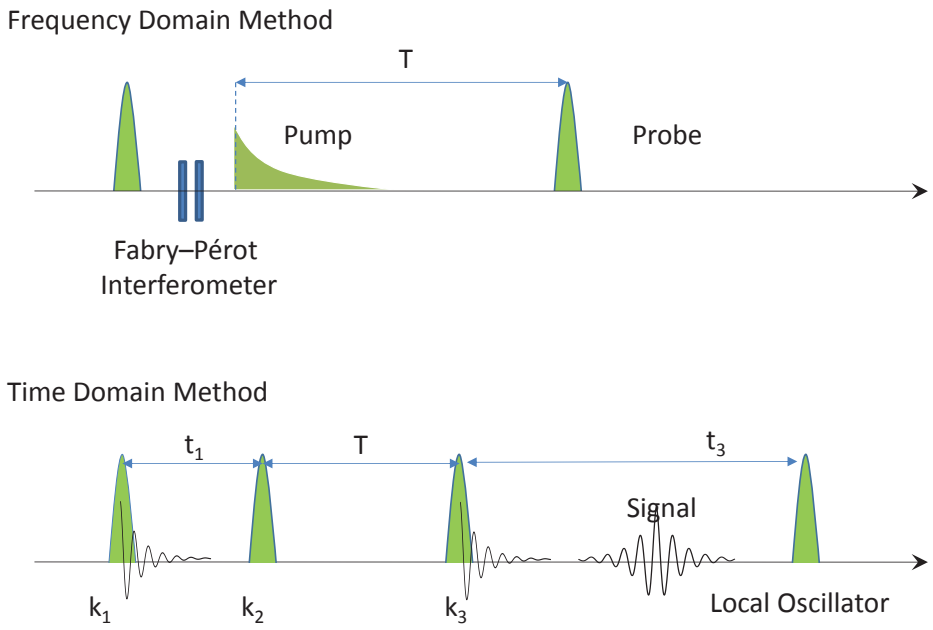

Fig. 3.2: 2D IR experiment: Frequency domain technique vs. Time domain technique

The interference signal is given by

$$S(\omega) = 2Re(f(\omega)exp(i\omega\tau)) \tag{3.3}$$

Here,

$$f(\omega) = E_0^*(\omega)E(\omega) \tag{3.4}$$

with the signal field $E(\omega)$ and the field $E_0(\omega)$ of the local oscillator. A Fourier transform to the time domain gives

$$F^{-1}S(\omega) = f(t-\tau) + f(-t-\tau) \tag{3.5}$$

This allows for deriving the frequency-dependent signal field as

$$E(\omega) = \frac{F\left[H(t)F^{-1}S(\omega)\right]exp(-i\omega t)}{E_0^*(\omega)} \tag{3.6}$$

where $H(t)$ is a window function in time which serves for suppressing noise from the detection process.[52]

The generation of phase-locked pulse pairs is a prerequisite for the Fourier-transform excitation and for heterodyne detection in the photon-echo scheme, requiring a phase-stabilized optical setup.

In active phase stabilization, fluctuations of the first order phase are measured and corrected instantaneously by moving a piezo-driven delay stage.[54, 55, 56] Passive phase stabilization is based on optical components which split an incoming pulse into two phase-locked replica. This can be achieved with diffractive optics or - less convenient - with conventional beam splitters.[57] A third method is the application of mid-infrared pulse shapers, based, e.g., on a germanium acousto-optic modulator (Ge AOM).[58, 59]

3.3 Setup for 2D IR spectroscopy

The present experiments are based on a 3-pulse photon echo scheme with heterodyne detection of the third-order signal. Passive phase stabilization is implemented with the help of diffractive optics, which generate two phase-locked pulse pairs in reflection. A schematic of the setup is presented in Figure 3.3. The diffractive optics scheme has been introduced in a time-resolved transient grating experiment[60] and 2D visible spectroscopy.[61] It was extended to the mid-infrared region in 2005.[36]

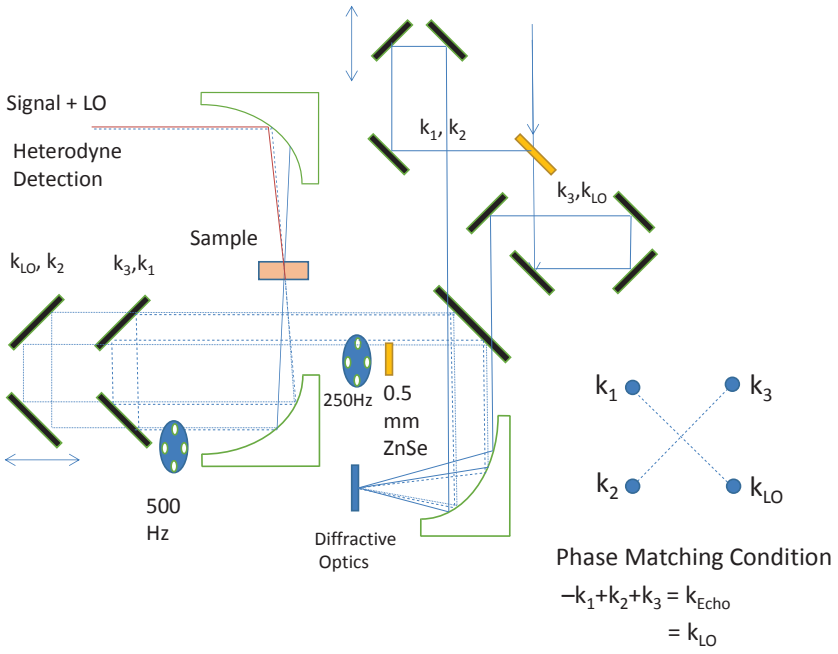

Fig. 3.3: Passive phase stable 2D IR setup using diffractive optics as a beam splitter. The diffractive grating is optimized to diffract 70% of the energy of each beam into the ±1 orders. The fourth beam is used as a reference, which is attenuated by copper mesh.

The infrared output pulse from the OPA is split by a ZnSe plate into two replica and aligned by

two irises. One of the pulses passes a delay line. Then, both pulses are focused by a parabolic mirror on an diffractive optics to generate two pulse pairs by $\pm 1^{st}$ order diffraction, the first pair for k_1 and k_2, and the second pair for k_3 and the local oscillator (LO). The four reflected beams are converted to parallel beams by the same parabolic mirror. The k_3 pulse then passes a 0.5 mm thick ZnSe plate to generate a 2.6 ps delay relative to the LO pulse. The time delay is chosen in a way that the signal is not undersampled by the array detector. At the same time, this time delay makes the local oscillator always arrive at the sample before k_3 in order to get rid of the pump-probe signal induced by it. The time delay between the (k_1, k_3) pair and the (k_2, k_{LO}) pair is controlled by a second delay line, which will modify the time delay of the upper beams and the lower beams. The intensity of the LO is attenuated by a factor of 100 using a copper mesh. The other three beams are focused on the sample by a second parabolic mirror. The nonlinear interaction of the k_1, k_2 and k_3 pulses generates a photon echo signal in the k_3+(k_2-k_1) direction. The photon echo signal and the LO pulse propagate in the same direction and fed into a monochromator (spectral resolution 2 cm^{-1}). The spectrally dispersed interferogram is detected with a 64-pixel HgCdTe (MCT) single array detector. The pulse to pulse stability of the energy of the mid-infrared pulses is better than 0.5%. The spatial and time overlap of the three pumping pulses is optimized by maximizing the frequency integrated non-resonance transient grating signal from a 1 mm thick ZnSe plate.

The pulse pairs (k_1, k_2) and (k_3, k_{LO}) experience the same fluctuations of the mirrors in the setup and, thus, the first order spectral phase is stabilized by the coupled fluctuation of k_1, k_2 and k_3, k_{LO}:

$$\Delta\varphi_{LO} - \Delta\varphi_3 = \Delta\varphi_2 - \Delta\varphi_1 \tag{3.7}$$

As a result of the coupled motion of the delay of the two pulse pairs, the 2D setup works effectively in the rotating wave frame.

When interacting with the DNA film samples, light from the different beams is elastically scattered, resulting in a background signal on the detector. To separate scattered light from the nonlinear signal, two mechanical choppers are introduced in the setup and difference signals are recorded. The chopper sequences for the four beams are summarized in Figure 3.4.

3.4 The pump-probe setup

Independently tunable pump and probe pulses were generated in two separate OPA systems driven by the output of an amplified femtosecond Ti:sapphire laser system. The setup for two-color pump-

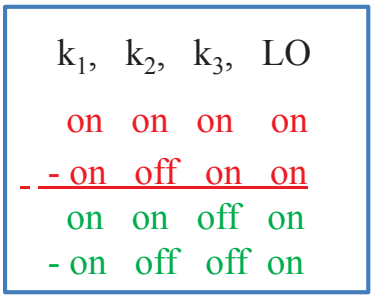

Fig. 3.4: How to subtract the interference from the scattered light from the sample

probe experiments is depicted schematically in Figure 3.5. The pulse to pulse stability of the probe

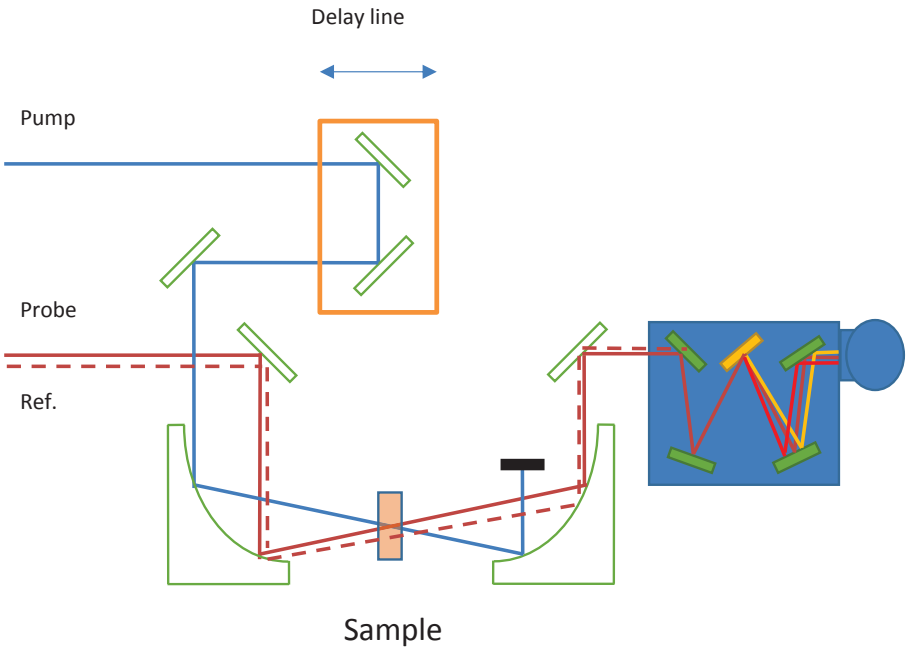

Fig. 3.5: Pump-probe setup with a reference beam

beam is optimized to better than 0.5%. In order to further suppress pulse-to-pulse fluctuations of the pump-probe signal, a reference beam is introduced and the change of absorbance $\Delta A(\omega,t)$ of the sample is measured as

$$\Delta A(\omega,t) = -log\left(\frac{I(\omega,t)_{pump\,on}}{I(\omega,t)_{ref}} \cdot \frac{I(\omega,t)_{ref}}{I(\omega,t)_{pump\,off}}\right) \tag{3.8}$$

In the setup, the pump pulse passes a delay line and is then focused on the sample. The same off-axis parabolic mirror is used to focus the probe and the reference beams. The probe beam overlaps with the pump beam in the sample (spot size approximately 200 μm), while the reference beam travels

through an unexcited part of the sample. The transmitted probe and reference pulses are spectrally dispersed with a monochromator and detected by a 2*64 element MCT(HgCdTe) detector. A 100 μm thick InSb plate is used for optimizing the spatial overlap and determining the delay zero of the pump and probe pulses in the 8 to 11 μm range. For pulses around 3 μm, a thin Ge plate is used.

3.5 Analysis of the optical interaction geometry in 2D IR setup with diffractive optics

Diffractive optical elements allow for the generation of phase-locked pulse pairs in a most reliable way. There are, however, the following issues that need to be addressed for a proper design of such elements: (i) Diffractive optics introduces a spatial chirp on the reflected pulses, i.e., the different frequency components of the pulse spectrum are reflected under different angles. (ii) The angular dispersion of the pulses affects the phase-matching process in a four-wave-mixing geometry. (iii) The overall spectral bandwidth a diffractive element can handle is typically less than an octave in frequency, making two-color 2D experiments with a single element difficult.[62] In the following, the influence of angular dispersion on phase-matching is analyzed in detail.

Reflection from a diffractive element for normal incidence of the incoming beam is governed by the grating equation

$$d \sin(\theta_m) = m\lambda \tag{3.9}$$

The elements are optimized for the first-order diffraction, i.e., the two phase-locked pulses are generated under the angles $\theta_\pm$ given by

$$d \sin(\theta_{\pm 1}) = \pm\lambda \tag{3.10}$$

The difference in wavevector of a particular spectral component is

$$k = \mid \vec{k} \mid = \frac{2\pi}{\lambda} \tag{3.11}$$

$$\Delta k = \mid k_2 - k_1 \mid = 2k \sin\theta = \frac{4\pi}{\lambda} \sin\theta \tag{3.12}$$

Using Eq. 3.10 for a replacement of the sine function results in

$$\Delta k = \frac{4\pi}{\lambda} \cdot \frac{\lambda}{d} \equiv \frac{4\pi}{d} \tag{3.13}$$

This equation shows that the difference in wavevector depends on the period of the diffractive element but not on the wavelength, as shown in Figure 3.6A. In other words, the different frequency components of the pulses generate gratings with the same period in the sample. Applying this result to the

phase-matching condition in the photon-echo experiment yields

$$k_{signal} - k_3 = k_2 - k_1 = \frac{4\pi}{d} = k_{LO} - k_3 \tag{3.14}$$

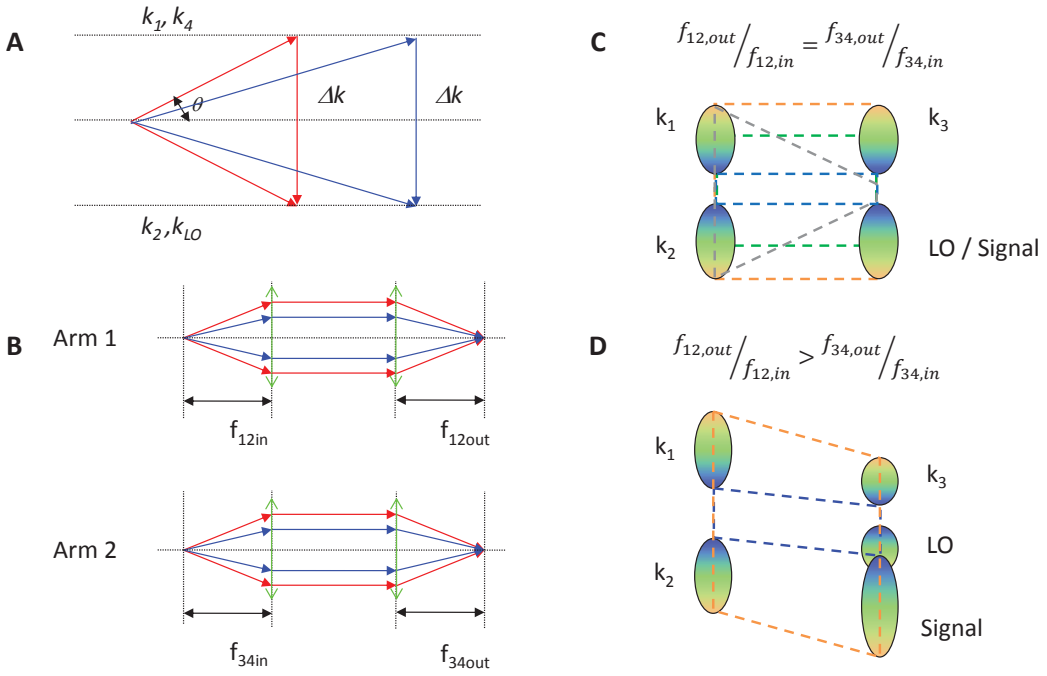

Fig. 3.6: Coupling between the diffraction and the phase matching process

So far, we have considered the case of normal incidence on the diffractive element. For an arbitrary angle of incidence θ_i, the grating equation reads

$$d(\sin\theta_i + \sin\theta_m) = m\lambda \tag{3.15}$$

In our case:

$$d(\sin\theta_i + \sin\theta_{\pm1}) = \pm\lambda = \pm\frac{2\pi}{|k|} \tag{3.16}$$

$$d(\sin\theta_{+1} - \sin\theta_{-1}) = 2\lambda = \frac{4\pi}{|k|} \tag{3.17}$$

$$|k|\sin\theta_{+1} - |k|\sin\theta_{-1} = \frac{4\pi}{d} \tag{3.18}$$

The last expression shows that the difference of the projections of $\vec{k}$ on the plane of the diffractive element is independent of wavelength. In the special case of normal incidence, $|k|\cos\theta_{+1} = |k|\cos\theta_{-1}$ and this equation can be written in the form of Eq. 3.13.

This analysis shows that the diffraction geometry for generating the phase-locked pulse pairs and the phase-matching in the four-wave-mixing geometry are coupled. The transient grating generated

in the sample by the pulse pair (k_1,k_2) is achromatic if the plane of the diffractive element and the plane of the sample are parallel, defining an alignment condition for the experiment. Diffraction of the spatially chirped pulse k_3 from the achromatic grating in the sample results in a spatially chirped photon-echo signal. The spatial chirp of the signal is identical to that of the local oscillator (LO) pulse, i.e., for a proper alignment of signal and LO beam the heterodyning process works for each spectral component. It should be noted that the cross peak signals in a 2D spectrum involve different frequency components of the (k_1,k_2) and the (k_3,k_{LO}) pulse pairs.

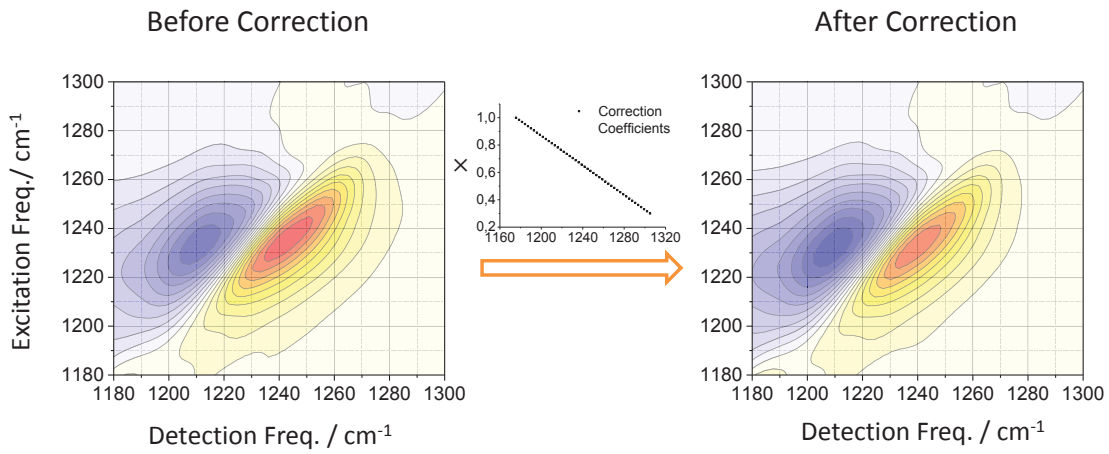

Fig. 3.7: Correction of 2D IR peaks. A linear correction coefficient is applied to a distorted 2D IR spectrum to change the weight of different spectral components. The analysis shows that there is an underestimation of 20% for the component at a detection frequency ν_3=1210 cm^{-1} compared to that at ν_3=1240 cm^{-1}.

If the two parabolic mirrors are aligned without taking a possible spatial chirp into account, i.e., for $\frac{f_{12,out}}{f_{12,in}} \neq \frac{f_{34,out}}{f_{34,in}}$, the alignment not only makes the generated signal beam not collinear with the reference beam, but also makes it have a different spatial chirp compared with the reference beam, as shown in Figure 3.6D. This results in different vertical distances between different spectral components of these two beams. In our case, the blue part has a shorter vertical distance compared to the red part. The aberration of the imaging system in vertical direction plays a role in the interferometry detection. For instance, the blue part of the two beams can have a better overlap than the red part. In other words, there is an inhomogeneous detection of the echo, affecting the relative strength of signals detected in different spectral regions. This may contribute to a blue shift of the high-frequency peaks in 2D IR spectra, especially when the vibrational band has a large homogeneous width as shown in Figure 3.7. A carefully alignment of the parabolic mirror in 2D IR setup is needed to avoid the influence of imaging aberration.

3.6 How to eliminate the effect of imaging aberration?

In our 2D IR experiment, we reconstructed the field of the signal by using the interference between photon echo signal and local oscillator with a known phase. One requirement is that the different spectral component of local oscillator and photon echo fully overlap or at least overlap homogeneously. For any pixel on the detector, we get the intensity of the signal beam by

$$I(\omega) \propto \int dx I(x,\omega) = \int dx E(x,\omega)\bar{E}(x,\omega) = E_{avg}(\omega)\bar{E}_{avg}(\omega) \tag{3.19}$$

Here, the width of the pixel is ignored and only the height direction 'x' is considered. The function of $E(x,\omega)$ can be viewed as a vector in Hilbert space. Then when it comes to the interference part of two different beams, one gets

$$\int dx E_1(x,\omega)\bar{E}_2(x,\omega) \leqslant E_{1,avg}(\omega)\bar{E}_{2,avg}(\omega) \tag{3.20}$$

Only when $\frac{E_1(x,\omega)}{E_2(x,\omega)} = constant$, the left equals the right side. In other words, the two vectors in Hilbert space are parallel to each other and the product reaches its maximum. Only when the same frequency component of the two beams in spectral interferometry have exactly the same spatial distribution of their electric field as a function of pixel height, this technique can be used to reconstruct the electric signal field correctly. In case that identical spectral components of the local oscillator and the signal do not propagate parallel to each other but with different spatial chirp, the spherical aberration of the imagine system of 2D IR setup starts to play a role and affects the field reconstruction of the signal.

The four-wave-mixing process can be viewed as a transient diffraction process of a third beam on the transient grating formed by the first two beams. Four-wave mixing in a boxcar geometry always generates an echo pulse with a spatial dispersion different from the excitation beams, as shown in Figure 3.6. A proper heterodyne detection and reconstruction of the field of the echo requires that the influence from the imagining aberration in the height direction of the pixels is minimized. A solution is to optimize the alignment of 2D IR setup to avoid imagining aberration as much as possible.

In order to avoid this problem, I. V. Rubstov and coworkers suggested a setup that can change the geometry of the all the four beams in the experiment.[63] Here, the error in the cross peak amplitude from imaging aberration is at the level of 20%. A 2D IR setup in pump-probe geometry avoids a different spatial chirp of the collinear signal and the reference beam. The signal will always have a similar spatial chirp of the third beam, where the third beam is used in the self-heterodyned detection of the signal. Moreover, the cross peaks have the same spacial chirp as the third pulse k_3 since

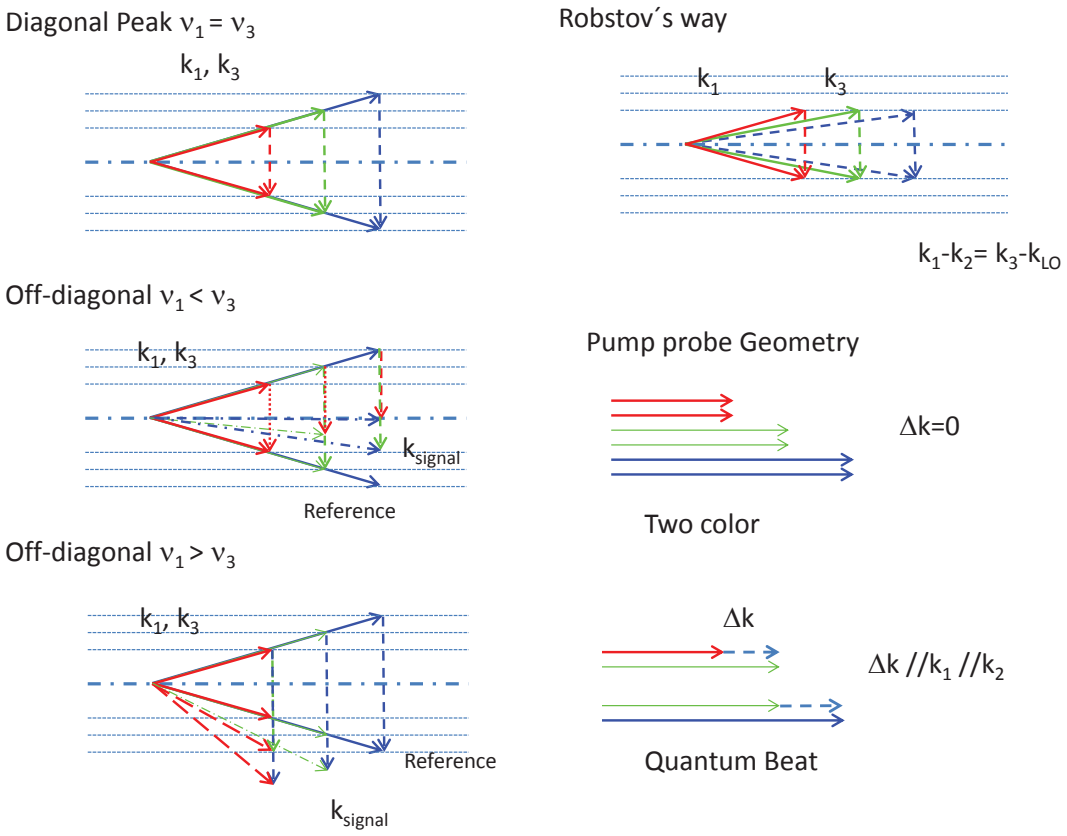

Fig. 3.8: Phase matching induced spatial chirp of 2D setup in different geometries. In boxcar geometry, the signal related to the cross peaks of 2D spectra will have a different spacial chirp as the diagonal ones. In pump-probe geometry, there is no such a difference between the diagoanl peak and cross peaks except the quantum beating.

$k_2(\omega_2) - k_1(\omega_1) = 0$ when $\omega_1 = \omega_2$ as shown in Figure 3.6. The only exception are quantum beating signals propagating in a direction different from the probe.

In summary, the pump-probe geometry is a more simple and convenient choice for 2D experiments in the far-IR region and for two-color broadband schemes. The collinear pump-probe geometry will introduce almost no variation of the spatial chirp of the signal field. This advantage has been exploited in a number of broadband and two-color 2D IR experiments.[53, 64]

4. DNA SAMPLES AND LINEAR INFRARED SPECTRA

Two types of DNA samples are studied in this thesis, the prototypical salmon testes DNA in an aqueous environment and artificial double-stranded DNA oligomers which are processed into DNA-lipid complexes and cast into thin films on substrate materials transparent in the relevant mid-infrared spectral range. The thin films are mounted in a humidity cell which allows for changing the water content of the samples in a wide range.

4.1 Preparation of DNA samples

The artificial DNA oligomers contain 23 alternating adenine-thymine base pairs with a sequence of 5′-T$(TA)_{10}$TT-3′. The DNA-lipid complexes were prepared by replacing the counterion Na^+ from NaDNA with cetyltrimethylammonium (CTMA) $[CH_3(CH_2)_{15}N(CH_3)_3]^+$, following a procedure first described in Ref.[65] A water solution of CTMA chloride (about 0.5 g/L) is put into a water solution of NaDNA (about 0.5 g/L). As a result of its low solubility in water, the DNA-CTMA complex precipitates at the bottom of the container. The complexes are washed out several times by pure water to remove the adsorbed extra NaCl. The cleaned complexes are dissolved in ethanol and cast on a BaF_2 window to make a film with good optical quality.

A homemade humidity cell is used to keep the DNA film at a controlled level of hydration.[66] The optical part of the cell consists of a closed volume between the entrance window with the DNA film on the inner side and an exit window. This cell is connected to a reservoir containing P_2O_5 powder or a saturated solution of $NaBrO_3$ in water to maintain the relative humidity (r.h.) at values of 0% or 92%. After an equilibration period, the water content of the DNA film assumes a value determined by the humidity of the inner-cell atmosphere. According to a gravimetric calibration of the water content, first discussed by M. Falk et al.[11], the DNA sample contains less than 2 water molecules per base pair (b.p.) at 0% r.h. and 20-30 water molecules per b.p. at 92% r.h.

Salmon testes DNA contains approximately 2000 base pairs, 41% of which are guanine-cytosine

and 59% adenine-thymine pairs in Watson-Crick geometry. The molecular weight is approximately 1.3 MDa. DNA samples in the solution phase are made by dissolving DNA in a 3 M NaCl or a (0.1 M NaCl, 1 M $MgCl_2$) solution in water. The weight ratio is controlled to make a hydration level of about 150 water molecules per b.p. The thickness of the DNA solution sample is estimated to be 7.5 μm.

4.2 Linear infrared spectra and normal mode assignments

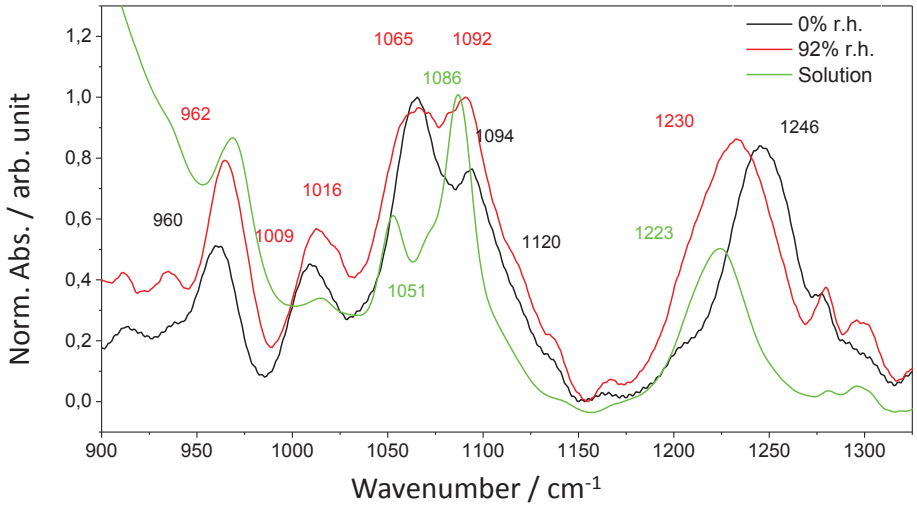

Fig. 4.1: FT-IR spectra of backbone modes measured with DNA at different environments. The black curve from dehydrated AT23 CTMA film, red from hydrated AT23 CTMA film, green from salmon test DNA in 0.1 M NaCl.

Figure 4.1 summarizes the linear infrared absorption spectra of different DNA samples in the frequency range from 900 to 1350 cm^{-1}. The distinct bands are due to different backbone modes of DNA, while the broad background at low frequencies originates from the librational absorption of the embedding water. The spectrum of the dehydrated AT23 film is plotted in black, of the hydrated AT23 film in red and the salmon testes DNA in solution in green. The peak at 1250 cm^{-1} region represents the antisymmetric stretching band P1 of the phosphate groups. This band displays a pronounced red-shift with increasing hydration level a behavior also found in phospholipids and first discussed in Ref.[11]

There is detailed literature on the assignment of the infrared bands to normal modes of the backbone, based on the infrared and Raman spectra of isotope labeled DNA and on normal mode calculations.[68, 69, 70, 67, 71, 72] The resulting assignments are listed in Table 4.1. There are two

Tab. 4.1: Vibrational modes of the sugar-phosphate backbone of DNA under different hydration conditions

Mode	Freq. / cm^{-1}			Character and contribution (in % PED)
	0% r.h.	92% r.h.	Solution	
ν_{P1}	1246	1230	1226	Phosphate: $\nu_{as}(PO_2^-)$ 91%
ν_{R0}	1120	1120	1120	Furanose ring
ν_{P2}	1094	1092	1086	$\nu_{ss}(PO_2^-)$ 52%;ν_s (OPO) 26%; ν_s(CO) 16%
ν_{L1}	1069	1071	1071	Diester linkage: ν_s(CO) 41% ; ν_s(CC) 17% ; ν_{ss} (PO_2^-) 31%
ν_{L2}	1049	1052	1051	Diester linkage: ν_s(CO) 48% ; ν_s(CC) 20% ; ν_{ss} (PO_2^-) 21%
ν_{R1}	1009	1013	1014	Furanose ring: C2′ C1′ OC4′
ν_{R2}	976	976	976	Ribose main chain: undefined coordinate
ν_{L3}	960	962	967	Diester linkage: ν_s(CC) 42% ; ν_s(OPO) 27% ; ν_s(CO) 12%

The character of the backbone vibration modes is derived from ab initio normal mode analysis of dimethyl-phosphodiester with a PED analysis.[67]

major structural elements in DNA backbone: one is the phosphodiester unit and the other is the sugar ring. One needs to be very careful when it comes to the assignment of the infrared bands. At first glance, an assignment based on quantum calculations using the phosphodiester only is too simple a model for the assignment of all peaks in the 8 to 11 μm region. The ^{13}C isotope-labeled Raman spectra, however, show that the P2 mode has no contribution from the motion of C2 and C1 as there is no isotopic frequency shift. While, when it comes to the case of R1 mode, there is a shift of 5 cm^{-1} when C1 is isotope labeled by ^{13}C, and 1 cm^{-1} when C2 is isotope labeled by ^{13}C. For R2 modes, the corresponding shift is 13 cm^{-1} and 3 cm^{-1}. While when it comes to the L1 and L2 modes, there is no isotopic frequency shift when one labels C1, and there is a 4 cm^{-1} red shift of L1 modes when C2 is isotope labeled. All these mean that the assignment of all these five peaks is reliable and it is pretty good to use diethyl phosphate as a simplified model to do a normal mode analysis to DNA backbone.

The assignments listed in Table 4.1 show that the normal modes are delocalized over several functional groups, i.e., comprised of several local modes. The P2 mode has a contribution from the CO stretching mode, while the linkage modes L1 and L2 have some contribution from the symmetric stretching mode of the phosphate groups. From the isotope shift spectra, it can be seen that the L2 and R1, R2 modes all have a contribution from the movement of C2 atom, while R1 and R2 have both C1 and C2 atoms involved. This indicates some excitonic coupling between the linkage mode and the sugar ring modes. All these will contribute to the intrinsic off-diagonal peaks in the 2D IR spectra discussed in the later chapters.

The spectra in Figure 4.1 exhibit a decrease in infrared linewidth upon increasing the hydra-

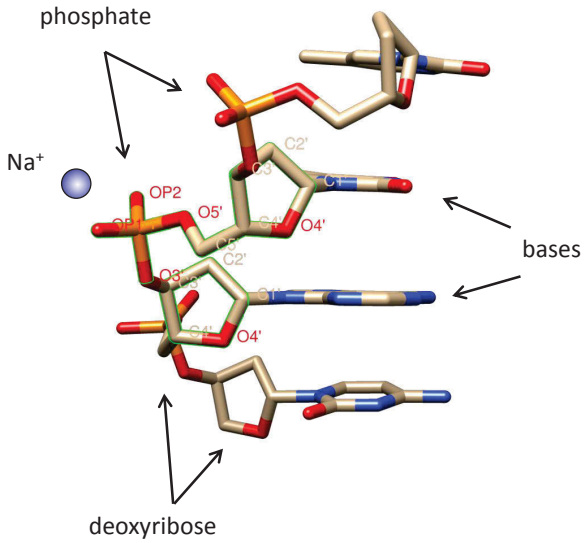

Fig. 4.2: DNA backone structure and the atom numbering

tion level from 2 water molecules per b.p. to 20 water molecules per b.p., and further to 140 water molecules per b.p.. This finding suggests a reduction of inhomogeneous broadening, i.e., a decrease of structural heterogeneity of the hydrated DNA as the hydration level increases.

4.3 Temperature-dependent infrared absorption spectra of salmon testes DNA

In order to investigate the influence of temperature on the infrared absorption spectra of the DNA backbone, a temperature variation experiment on salmon testes DNA in 0.1 M NaCl solution was performed. Measurements were done at five fixed temperatures separated by 5 K in the temperature interval from 298 K to 318 K. The spectra at these five temperatures are shown in Figure 4.3. In order to make the variation of the spectra clearer and easier to compare with transient pump-probe spectra presented in Chapters 7 and 8, the difference spectra were derived and shown in the lower panel of Figure 4.3. They represent the changes expected for a respective temperature jump of 5 to 20 K in the sample.

The different DNA absorption bands are superimposed on a broad background originating from the librational absorption of the surrounding water. This background changes with increasing temperature. Above 1000 cm^{-1}, the librational background decreases with increasing temperature, resulting in a spectrally broad negative component in the absorption changes. In addition, a very clear blue shift

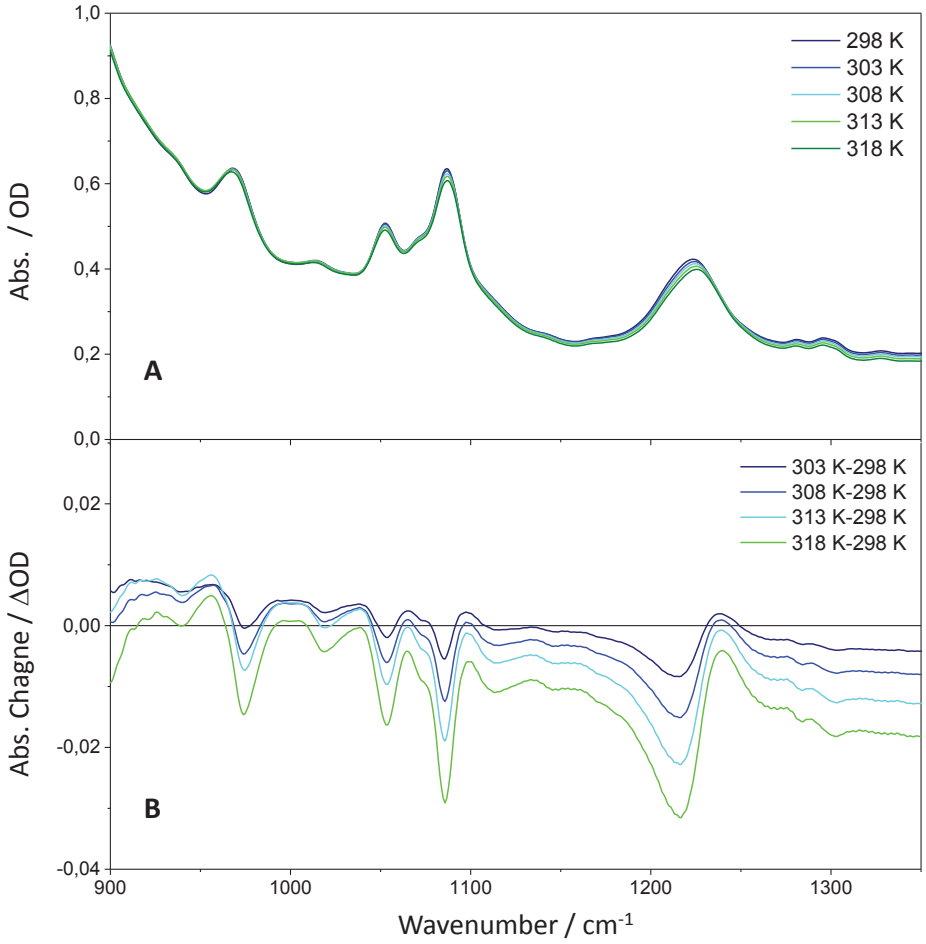

Fig. 4.3: Temperature dependent FT-IR spectra of backbone modes measured with salmon test DNA in 0.1 M NaCl solution.

of the stretching modes of the phosphate groups, P1, P2 and a red shift of the other backbone modes, i.e., L1, L2 and the ring modes are found. The former points to a weakening of the hydrogen bonds between water and the phosphate groups and changes in the electronic polarizability of the phosphate, while the red-shift of the other modes originates from the thermal excitation of low-frequency fingerprint modes that are anharmonically coupled to the backbone stretching modes in the 9 μm to 11 μm region.

Part I

2D IR EXPERIMENT ON DNA

5. 2D IR SPECTRA OF SALMON TESTES DNA BACKBONE STRETCHING MODES

Methods of 2D IR spectroscopy have been applied frequently to study vibrational dynamics and couplings in water, ionic solutions, nucleic bases and base pairs in solution, as well as biomolecules at different levels of hydration. Work on biomolecular systems has focused on NH and OH stretching excitations, the amide-I and II region of the spectrum and other fingerprint vibrations.[37, 73, 74, 75, 76, 77, 78] In the present study, fluctuations and structural dynamics of the hydration shell around DNA are probed via DNA backbone vibrations in the spectral range from 900 to 1300 cm^{-1}. Such modes involve functional groups located at the DNA-water interface, thus being sensitive to both electric fields and local interactions at the DNA surface. Moreover, backbone modes are non-invasive probes, leaving the genuine hydration geometries of DNA unaffected. Two sets of independent experiments are performed, one on the antisymmetric and symmetric stretching modes of phosphate groups in the backbone, and the other on the symmetric phosphate stretching mode and the carbon linkage and sugar ring modes. The first one is mainly focused on the coupling of two P=O stretching modes and their response to the environment's fluctuations. The second mainly concentrates on spectral diffusion and solvation dynamics induced by the water molecules around DNA. Dynamics of DNA backbone modes are compared at different hydration levels to isolate the influence of the fluctuating hydration shell.

All 2D IR experiments are performed with parallel linear polarization of the three pulses in the photon-echo sequence and the fourth local oscillator pulse. Reorientation processes of vibrational transitions dipoles by, e.g., rotational degrees of freedom and/or resonant energy transfer between vibrations have not been studied in detail. In this chapter, we focus on salmon testes DNA with CTMA and Na^+ as counterions. The linear FT-IR absorption spectra of the samples are shown in Figure 5.1.

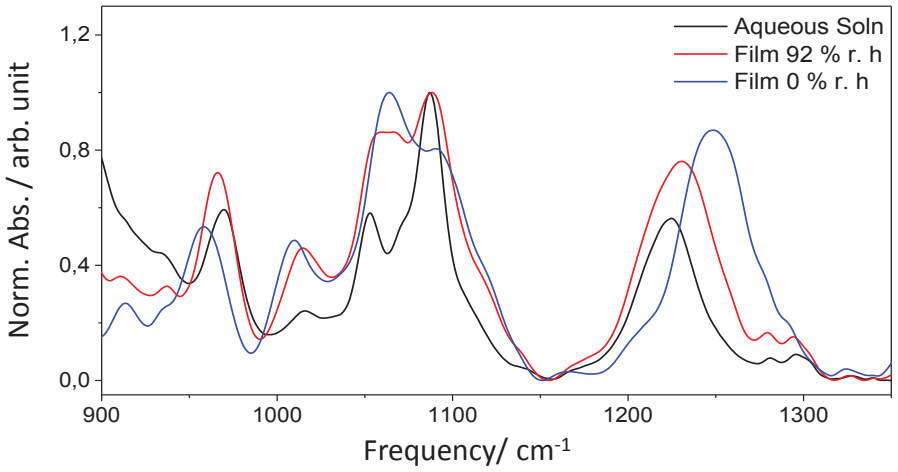

Fig. 5.1: Linear FT-IR absorption spectra of backbone modes of salmon testes DNA at different hydration levels.

5.1 2D IR spectra of DNA backbone modes at early waiting time

5.1.1 2D IR spectra of phosphate stretching modes at different hydration levels

Figures 5.2 and 5.3 show the 2D IR spectra at a waiting time of 250 fs of the symmetric (P2) and antisymmetric (P1) stretching modes of the phosphate groups at three different hydration levels. All spectra display two pairs of peaks along the diagonal direction ($\nu_1 = \nu_3$). The positive ones shown in red and yellow originate from the bleaching of the v=0 ground states and stimulated emission from the v=1 states, while the negative ones shown in blue represent the v=1 to 2 excited state absorption. As a result of the diagonal vibrational anharmonicity, the transition frequency of excited states absorption ($|1\rangle \rightarrow |2\rangle$ transition) is smaller than that of the fundamental transition ($|1\rangle \rightarrow |0\rangle$ transition). This fact results in a red shift of the negative relative to the positive peaks along the detection frequency axis ν_3. In the harmonic limit, the transition dipole of $|1\rangle \rightarrow |2\rangle$ transition is $\sqrt{2}$ times that of the $|0\rangle \rightarrow |1\rangle$ transition, resulting in a similar amplitude of the positive and negative peaks. The elliptic shape and substantial spectral width along the diagonal are due to the inhomogeneous broadening of the vibrational transitions, while the antidiagonal width is a measure of homogeneous line broadening. The spectra in Figures 5.2 and 5.3 show that the antisymmetric mode P1 has a larger diagonal width compared to the symmetric stretching mode P2.

In addition to the diagonal peaks, the 2D spectra in Figures 5.2 and 5.3 exhibit two pairs of cross peaks. These two pairs originate from the excitonic coupling between the two phosphate stretching modes. The positive components are from the bleaching of the original $|0\rangle \rightarrow |1\rangle$ transitions, while

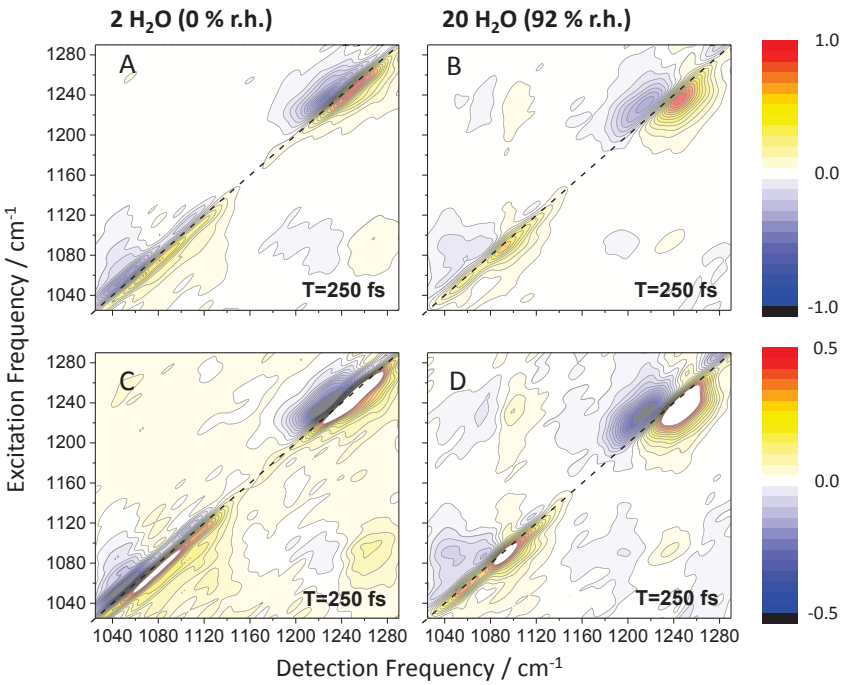

Fig. 5.2: 2D IR spectra of symmetric (P2) and antisymmetric (P1) phosphate stretching modes measured with a salmon testes DNA film at a waiting time of 250 fs. (A,C): hydration level 0% r.h. corresponding to less than 2 water molecules per base pair (b.p.).(B,D): hydration level 92% r.h. corresponding to 20-30 water molecules per b.p. The amplitude of the 2D IR spectra in panels (A) and (B) are normalized to the maximum nonlinear signal in the frequency range shown, while the spectra in (C,D) are normalized to half of the maximum.

the negative represent the contributions of the transitions shifted by the excitation of the other mode.

The anharmonicity of the diagonal peak pairs is estimated by fitting the 0° cuts of the 2D IR spectra in Figures 5.2 and 5.3. The fitting curves and the peak center are shown in Figure 5.4. The diagonal anharmonicity of the P1 mode in DNA CTMA films is about 15 cm^{-1}; in 0.1 M NaCl solution the value changes to 30 cm^{-1}. This means that the antisymmetric phosphate stretching mode is sensitive to the variation of its chemical environment.

The pairs of cross peaks are oriented in a direction more or less parallel to the diagonal direction axis $\nu_1 = \nu_3$. This finding suggests that the frequency fluctuation cross correlation between the two phosphate modes is positive, meaning that the anti-symmetric mode P1 and the symmetric mode P2 experience frequency fluctuation with the same sign but different amplitude. This conclusion is supported by the vibrational Stark shifts of the two modes measured with static electric fields,[47] and by theoretical work on $H_2PO_4^-$ ions in aqueous solution.[79]

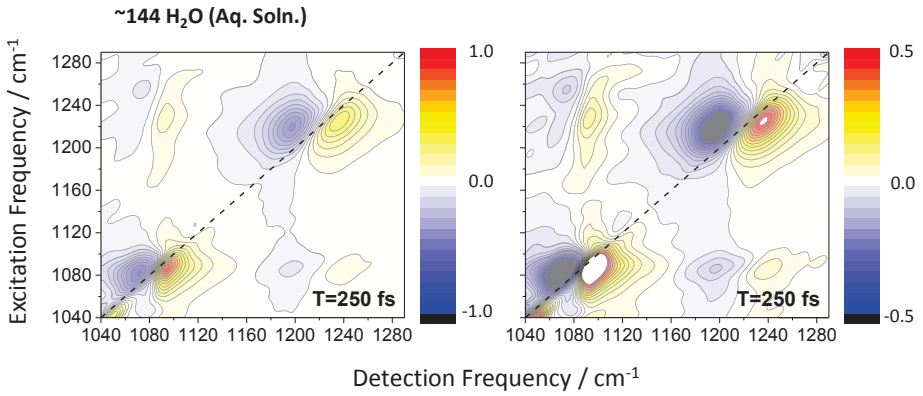

Fig. 5.3: 2D IR spectrum of symmetric and antisymmetric phosphate stretching modes of salmon testes DNA in a 0.1 M NaCl solution at a waiting time of 250 fs. There are approximately 144 water molecules per b.p. The amplitude of 2D IR spectrum in each plot is normalized to the maximum signal in the frequency window shown.

The phosphate stretching vibrations of 1,2-dioleoyl-sn-glycero-3-phosphocholine (DOPC) phospholipids in reverse micelles containing small water pools display a similar red-shift of the P1 absorption with increasing hydration level, besides the 2D IR spectra close to the present ones for salmon testes DNA.[80] Such 2D IR spectra again show a positive correlation of the frequency fluctuation function of the symmetric and antisymmetric stretching modes. In contrast, a negative or anti-correlation of the spectral shifts upon hydration changes has been reported for the phospholipid 1-palmitoyl-2-oleoyl-sn-glycero-3-phosphocholine (POPC).[47] This opposite behavior can be rationalized as follows. The quantum chemistry calculations reported in Ref. [47] for a selected hydration geometry predict a positive correlation of the frequency shifts when the electric field is along the C2 axis of the PO_2^- group. A negative correlation is calculated for an electric field along the free O-O axis of PO_2^-. For the case of the phosphate group in DNA and DOPC reverse micelles, the hydration geometry and position of counterions and/or choline group favor a predominant electric field along the C2 axis. The different behavior of POPC points to a different hydration pattern of this phospholipid.

5.1.2 2D IR spectra of backbone modes at frequencies below 1100 cm^{-1}

Figure 5.5 summarizes the 2D IR spectra in the frequency range of the phosphate (P2), phosphodiester linkage (L1-L3), and sugar ring structure (R1, R2) vibrations at an early waiting time (T = 250 fs). Each mode gives rise to a pair of diagonal peaks originating from its $|0\rangle \rightarrow |1\rangle$ and $|1\rangle \rightarrow |2\rangle$ transitions. Moreover, the 2D spectra display a very rich pattern of off-diagonal peaks, revealing

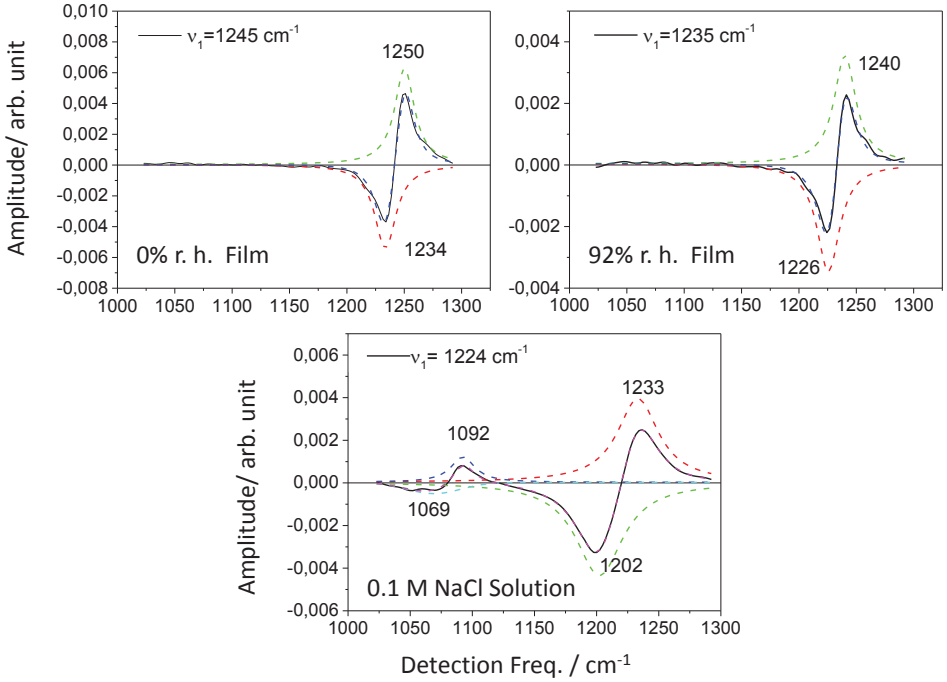

Fig. 5.4: Diagonal anharmonicity of the antisymmetric phosphate stretching mode P1 at different hydration levels

pronounced intermode couplings. As shown in Figure 5.5, the symmetric phosphate mode P2 is well separated from the L1 and L2 modes in the DNA/CTMA film at 92% r.h. case and for DNA in 0.1 M NaCl solution. In contrast, for the dehydrated case, it is hard to separate these three diagonal peak pairs at 0% r.h. This experimental fact points to a stronger inhomogeneous broadening of the vibrational bands in the dehydrated film, in line with the width of the absorption bands in the FT-IR spectra of Figure 4.1. We conclude that the hydration process reduces the structural heterogeneity of the system. On the other hand, the antidiagonal spectral width of the peaks along the diagonal increases with increasing hydration, suggesting a larger homogeneous linewidth of the corresponding modes. The different cross peaks demonstrate a strong coupling of the L1 and L3/R2 modes at all hydration levels. The symmetric phosphate mode P2 is coupled to the L2 mode as well.

5.2 Dynamical behavior of 2D IR spectra of DNA/CTMA film samples

In order to get insight in the time evolution of 2D IR spectra, we performed measurements for different waiting times. Figures 5.6 and 5.7 show 2D IR spectra of salmon testes DNA/CTMA thin films at 0% r.h. and 92% r.h. for several selected waiting times. From the time evolution of the diagonal peaks, one can track structural fluctuations of the system which are manifested in spectral

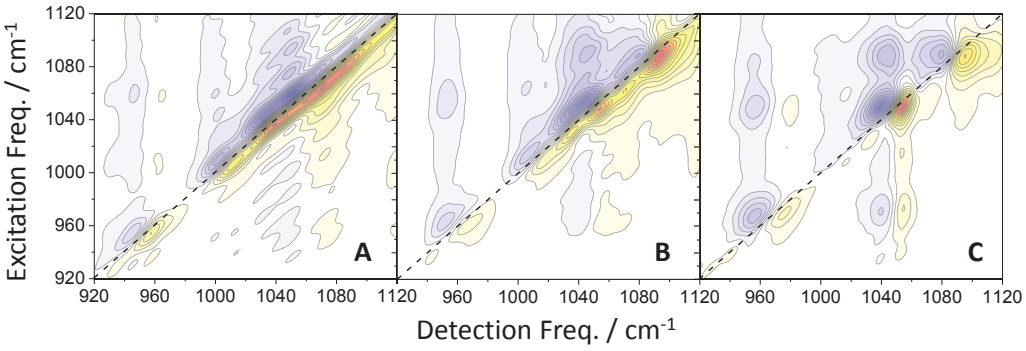

Fig. 5.5: 2D IR spectrum of salmon test DNA backbone modes at a waiting time of 250 fs. (A) 2 water molecules per b.p.; (B) more than 20 water molecules per b.p.; (C) about 144 water molecules per b.p. in 0.1 M NaCl water solution. The 2D spectra are measured with parallel linear polarization of the femtosecond pulses. The amplitude of 2D IR spectrum in each plot is normalized by the maximum of absolute value of the peaks in the frequency window.

diffusion. Both the shape and the orientation of diagonal peaks display minor changes up to waiting time of several picoseconds. In contrast, the cross peaks in the upper trigonal part of the 2D spectra undergo substantial intensity changes with increasing waiting time. More specifically, cross peaks at low detection frequencies gain in intensity relative to the cross peaks at high detection frequencies, indicating population transfer processes from the high-frequency donor to the low-frequency acceptor vibrations. This agrees with the difference of the apparent decay time in the two-color and direct pump-probe transients to be discussed in Chapter 7.

At waiting times T>6 ps, the 2D spectra display a stripe-like feature of negative sign at a detection frequency of ν_3=1100 cm^{-1}. A similar contribution has been observed in the 2D IR spectra of phosphate vibrations of DOPC reverse micelles and been assigned to spectral changes induced by vibrational heating.[79] The fast relaxation of the phosphate stretch vibrations transfers excess energy into the vibrational manifold and - when present - into the water shell. This mechanism results in an increase of vibrational temperature and a rearrangement of water molecules in the hydration shell. Both the change of local electric fields and a weakening of hydrogen bonds between hydrating water molecules and the phosphate group lead to a blue shift of the vibrational frequency of the symmetric phosphate stretching mode P2. The frequency positions of the other backbone modes undergo small spectral shifts as well. Such shifts are also present in the linear infrared absorption spectra measured at different ambient temperatures shown in Figure 4.3. A more detailed analysis of thermal effects will be presented in Chapter 8, including experiments in which the hydration shell is heated via OH

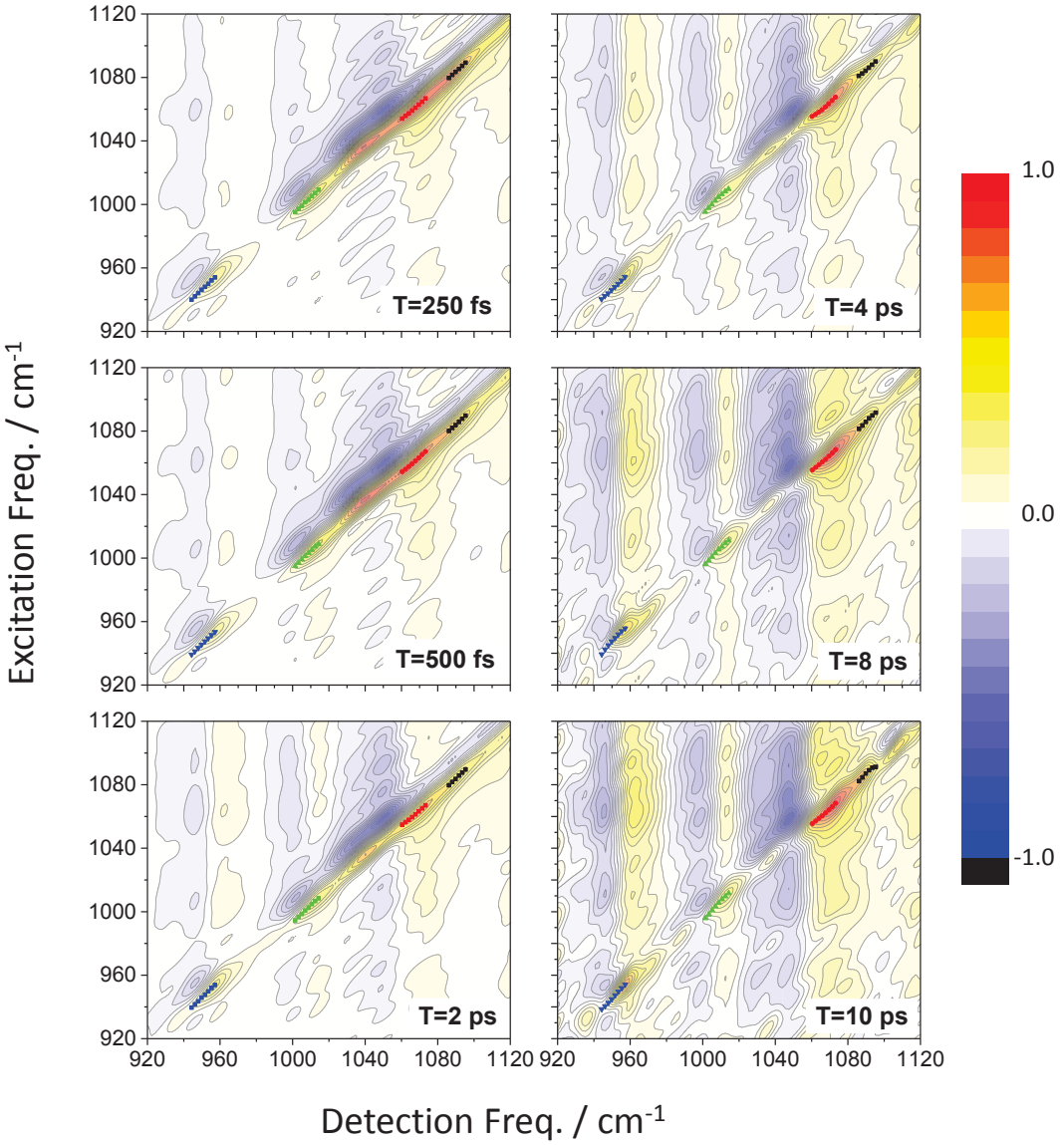

Fig. 5.6: 2D IR spectra of backbone modes at several waiting times for dehydrated salmon test DNA CTMA film with center line of the ground state bleach. The hydration level of 0% r.h. is estimated to be 2 water molecules per b.p. The amplitude of each plot is scaled to the maximum of 2D IR plots at every waiting time.

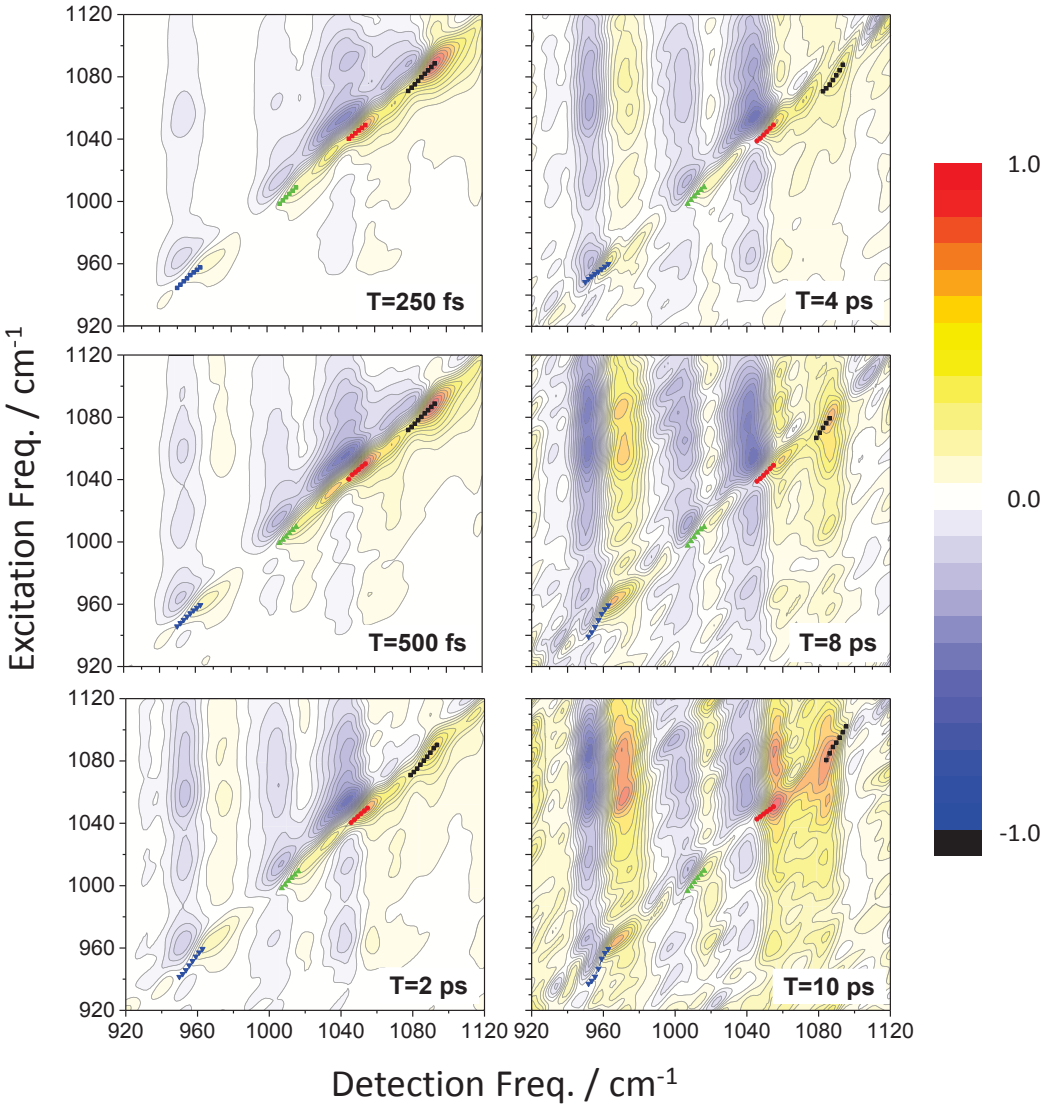

Fig. 5.7: 2D IR spectra of backbone modes at several waiting times for hydrated salmon test DNA CTMA film with center line of the ground state bleach. The hydration level of 92% r.h. is estimated to be more than 20 water molecules per b.p. The amplitude of each plot is scaled to the specific maximum of 2D IR plots at every waiting time.

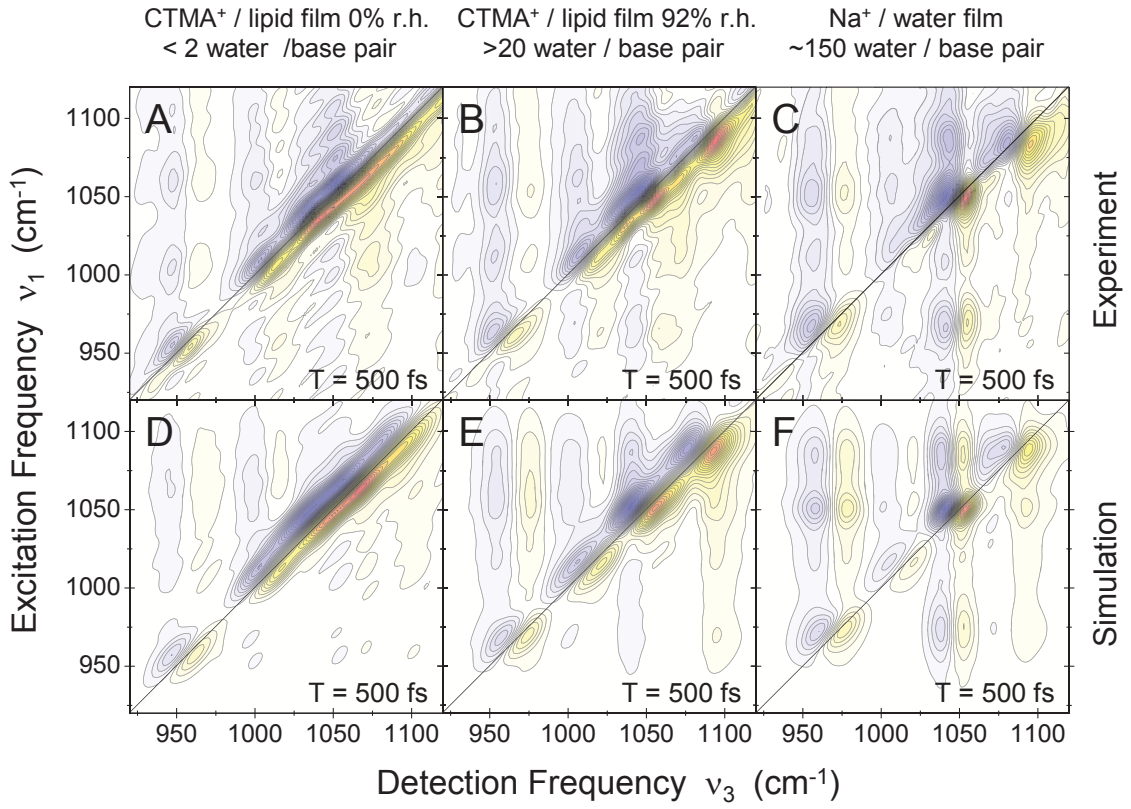

Fig. 5.8: 2D IR spectra of salmon test DNA backbone modes at different hydration levels. The signal change by 5% between adjacent lines. Panels A to C in the first row are experiment spectra with a waiting time of 500 fs, while those D to F in the second row are calculated spectra

stretch excitations of water molecules.

5.3 Analysis of fast fluctuation processes in 2D IR spectra using Kubo's theory

In order to analyze the mechanism determining the 2D lineshapes, a simulation has been done based on Kubo′s lineshape theory, as shown in Figure 5.8. The details of the theory have been described in Chapter 2. The lifetime used in the simulation of the vibration states is obtained from pump-probe experiment in Chapter 7. The frequency fluctuation correlation function (FFCF) used is

$$<\delta\nu(t)\delta\nu(0)>=\Delta\nu_{1i}^2 e^{-t/\tau_1}+\Delta\nu_{2i}^2 e^{-t/\tau_2} \tag{5.1}$$

A 300 fs fast fluctuation is used for the FFCF in the simulation as it is done in the work of DOPC.[80] A 50 ps slow fluctuation is used to get the heterogeneous broadening of the vibrational modes. All the parameters used in the simulation are listed in Table 5.1.

Tab. 5.1: Parameters obtained from the simulation of 2D IR spectra of DNA vibrational modes under different hydration conditions. The diagonal anharmonicity Δ and the FFCF are derived from the analysis of the linear and 2D IR spectra. The FFCF consists of two Kubo terms with amplitudes of $\Delta\nu_1$ and $\Delta\nu_2$ and decay times τ_1=300 fs and τ_2=50 ps.

Mode	Character	Frequency	Anharmonicity	FFCF	
		ν_0/cm^{-1}	Δ/cm^{-1}	$\Delta\nu_1/cm^{-1}$	$\Delta\nu_2$/ cm^{-1}
Water film of 0.1 M NaCl					
ν_{P2}	Sym. PO_2^-Str.	1090	7	11	3
ν_{L1}	Diester Linkage	1078	9	9	8
ν_{L2}	Diester Linkage	1051	9	7	4
ν_{R1}	Furanose ring	1018	10	8	10
ν_{R2}	Ribose main chain	979	12	7	6
ν_{L3}	diester linkage	970	12	7	6
CTMA film at 92% r.h.					
ν_{P2}	Sym. PO_2^-Str.	1092	11	9	7
ν_{L1}	Diester Linkage	1071	11	7	6
ν_{L2}	Diester Linkage	1052	11	7	7
ν_{R1}	Furanose ring	1016	8	7	12
ν_{R2}	Ribose main chain	976	9	6	6
ν_{L3}	diester linkage	962	8	7	6
CTMA film at 0% r.h.					
ν_{P2}	Sym. PO_2^-Str.	1096	12	5	13
ν_{L1}	Diester Linkage	1068	8	3	8
ν_{L2}	Diester Linkage	1038	15	4	15
ν_{R1}	Furanose ring	1009	8	4	9
ν_{R2}	Ribose main chain	972	9	5	8
ν_{L3}	diester linkage	957	9	6	8

The lineshape of all the diagonal peaks is reproduced well by assuming the τ_1 = 300 fs and $\tau_2 > 10$ ps.[81] The fluctuation amplitudes of the different backbone modes at these three hydration levels are summarized in Table 5.1. Combining with the simulation work of the local electric field on the phosphate vibration frequency, the fluctuation amplitude of the electric field along the C2 axis of PO_2 group is estimated to be 2.5 V/nm.[3]

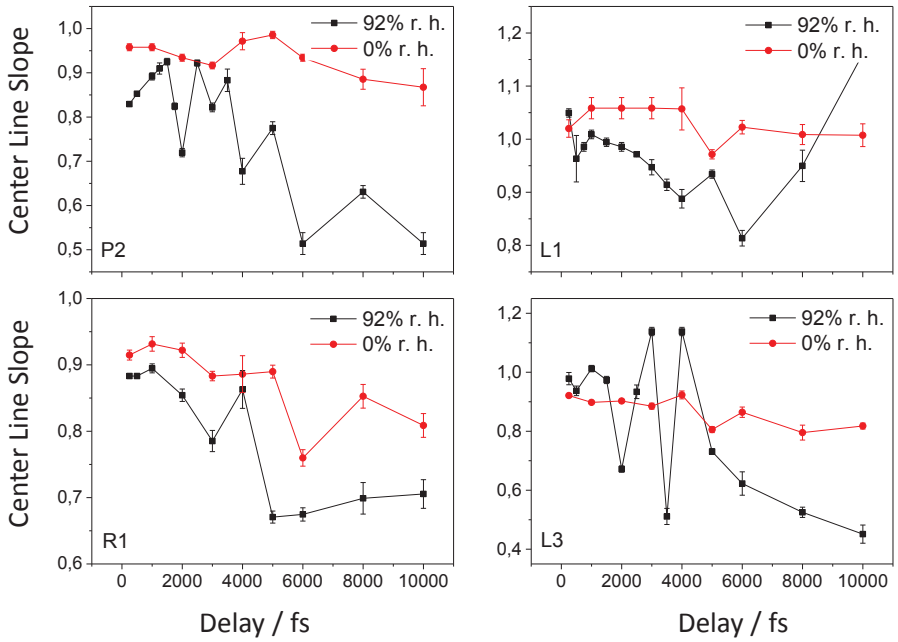

Fig. 5.9: Comparison of the center line slopes of 2D diagonal peaks of different backbone modes of DNA in CTMA film at two different hydration levels. The black points are data from dehydrated DNA, while the red ones are from the hydrated DNA film. There is a stronger change of center line slope in hydrated DNA than in dehydrated DNA.

5.4 Slow spectral diffusion processes reported by diagonal peaks

In order to check for slow spectral diffusion processes that affect the 2D lineshapes, we derive the center line slopes (CLS) of the positive diagonal peaks at every waiting time T and plot them as a function of T in Figure 5.9.[83] The CLS decays averaged over the 4 modes are shown in Figure 5.10 for the two hydration levels. They are roughly reproduced by exponential decays with time constants of 11.3 ps at 92% r.h. and 22.0 ps at 0% r.h.

There are mainly two processes contributing to spectral diffusion, structural fluctuations and resonant energy transfer between vibrations. The second mechanism consists in a population transfer between oscillators at different sites in DNA. The rate of resonance energy transfer is estimated by

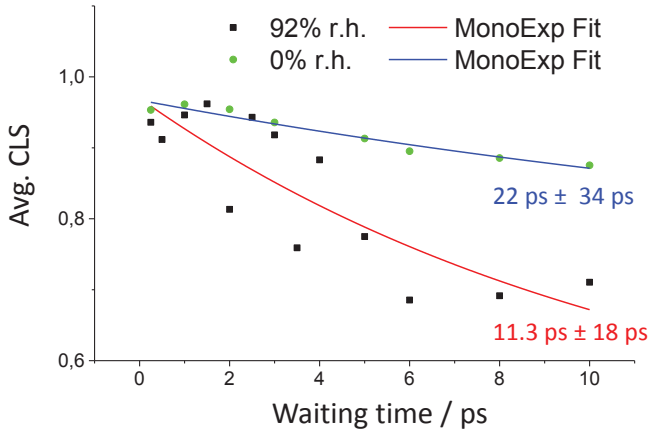

Fig. 5.10: Averaged center line slopes for DNA/CTMA film at two different hydration levels and single exponential decay curves from fitting.

the standard Förster method for point-like dipoles,[84]

$$k = \frac{3}{2T_{VR}}\kappa^2(\Omega)\left(\frac{R_0}{r}\right)^6 \tag{5.2}$$

Here, T_{VR} is the lifetime of the donor, R_0 is the Förster radius and r is the distance between the donor and the acceptor. The Förster radius R_0 (in cm) is given by

$$R_0^6 = \frac{9000(ln10)\kappa^2 Q_D}{128\pi^5 N_A n^4}\frac{\int_0^{+\infty}\frac{1}{\tilde{\nu}^4}\varepsilon_A(\tilde{\nu})\varepsilon_D(\tilde{\nu})d\tilde{\nu}}{\int_0^{+\infty}\varepsilon_D(\tilde{\nu})d\tilde{\nu}} \tag{5.3}$$

In this equation, ε_A is the excitation coefficient of the acceptor in (M^{-1} cm^{-1}), with a value of 400 M^{-1} cm^{-1} for the P2 mode; N_A is Avogadro's constant; n is the reflective index of the medium. Q_D is the quantum yield. It can be obtained by

$$Q_D = \frac{k_{rad}}{k_{rad}+k_{nr}} = \frac{k_{rad}}{k_D} \tag{5.4}$$

k_{rad} and k_{nr} are the radiative and nonradiative decay rate of the donor. The former can be estimated by [85]

$$k_{rad} = \frac{1}{\tau_{rad}} = 2.880\times10^{-9}n^2\tilde{\nu}_D^3\int d\tilde{\nu}\frac{\varepsilon(\nu)}{\tilde{\nu}} \tag{5.5}$$

Here, n is the refractive index, which is 1.256 for water at 1090 cm^{-1}; $\tilde{\nu}_D$ is 1090 cm^{-1} with a FWHM of 18 cm^{-1} for the symmetric stretching mode of phosphate groups in DNA solution. Using the above parameters, the Q_D is estimated to be 4.56 E-11.

κ^2 is the dipole-dipole coupling orientation factor between the donor (D) and acceptor (A). It is defined as following:

$$\kappa = \hat{u}_i\cdot\hat{u}_j - 3(\hat{u}_i\cdot\hat{n})(\hat{u}_i\cdot\hat{n}) \tag{5.6}$$

For the case of neighboring phosphate groups in B DNA, we have κ = 1.0, r = 7.0 Å, which are calculated from the crystal structure of B-DNA dodecamer.[86]

The resonant energy transfer rate is proportional to the overlapping of the homologous broadening of vibrators in different chemical environment. The excitation transfer induced spectral diffusion (ETISD) can be calculated from the time-dependent probability distribution of the vibrational frequencies. For a two-particle system, the excitation transfer induced FFCF is given by the following formula:[84]

$$\langle \delta\omega(t)\,\delta\omega(0)\rangle = E\{\delta\omega_1, \delta\omega_2\}\left[\frac{1}{2}\left(1+e^{-2k(\omega_1,\omega_2)t}\right)\delta\omega_1^2 + \frac{1}{2}\left(1-e^{-2k(\omega_1,\omega_2)t}\right)\delta\omega_1\delta\omega_2\right] \tag{5.7}$$

In the case of B DNA, the excitation transfer between the chromophores in the compensation strand can be ignored, for the nearest distance between the nearest pair is 12 Å, which is 1.7 times of the distance between the neighboring phosphate groups in the same strand.

This makes it possible to use a one-dimensional-lattice model to simulate of the ETISD.

$$\langle \delta\omega(t)\,\delta\omega(0)\rangle = \int\int d\omega_1 d\omega_2 P(\delta\omega_1)\,P(\delta\omega_2)\left(\delta\omega_1\delta\omega_2\left[1-G_s^{\delta\omega_1,\delta\omega_2}(t)\right]+\delta\omega_1\delta\omega_1 G_s^{\delta\omega_1,\delta\omega_2}(t)\right) \tag{5.8}$$

The self part of Green's function $G_s(t)$ can be obtained using following relationship derived from Equation 10 in the work of Rosenfeld in 2012.[84].

$$lnG_s(t) = exp\left(-\frac{3tR_0^6}{T_{VR}r^6}\kappa^2(\Omega)\right) - 1 \tag{5.9}$$

In the simulation, we use a homogeneous width of 10.7 cm^{-1} and an inhomogeneous width of 21.2 cm^{-1} for the dehydrated DNA film, while for hydrated case we use 16 cm^{-1} and 13.6 cm^{-1} correspondingly. The homogeneous width used here is from the fitting of the antidiagonal cuts of the P2 mode in 2D IR spectra at waiting time of 250 fs, while the inhomogeneous width from the peak fitting procedure of the static spectra in 930 to 1140 cm^{-1} regions. Using the two particle model, the ETISD is estimated with a time constant of 90 ps for DNA at 0% r.h. and 35 ps for DNA at 92% r.h. Using the one-dimensional lattice model, it is estimated to occur with respective time constants of 70 ps and 27 ps. All such values are longer than the experimental decay times. We conclude that the experimental decays include contributions from both resonant energy transfer and structural fluctuations. For the latter, time constants of 19 ps and 32 ps in the hydrated and dehydrated DNA CTMA film are derived by a decomposition of the experimental decay rates into two partial rates. The 32 ps dynamics can be attributed to the structure fluctuation of DNA because water motions are heavily restricted in dehydrated DNA CTMA film.

In former time-resolved Stokes shift experiments on DNA to which organic chromophores were attached, an 11.6 ps process was discovered in the hydration correlation function.[33] So the pure structural spectral diffusion process of hydrated film has a great chance to be a reflection of the hydrogen bond dynamics on DNA surface. The simulation work of M. A. Berg and coworkers in 2009 revealed that most of the dynamics in the first 10 ps comes from the structural fluctuation of water.[87] A 19 ps process reported by transient Stokes shift of dye molecule Hoechst 33258 [88] has been assigned to DNA dynamics by Furse and Corcelli, according to their nonequilibrium molecular dynamics simulation of the same system.[89, 90] In their simulation work, two slow processes were discovered: 2.6 ps water dynamics and 30 ps DNA dynamics. In the simulation of M. A. Berg and coworkers in 2009,[87] they also found a similar contribution from DNA fluctuation. Meanwhile, they discovered that the fluctuation of the counter ions is small and with a time constant of 220 ps. The theoretical study of Furse and Corcelli showed a very similar result that the contribution from counter ions is minor and essentially flat as the time varies. These suggest that the major part of the structural spectral diffusion of the dehydrated DNA CTMA film comes from the movement of DNA for their are only two water molecules per b.p. and their movement is locked by adjacent phosphate groups. As a result of poor signal-to-noise ratio in our CLS from 2D IR spectra, we can not separate the contribution of water dynamics and DNA dynamics in hydrated DNA CTMA film. Here, we can only say that both these two processes have chance to contribute to the structural fluctuation of hydrated DNA reported by the 2D IR spectra.

5.5 Conclusions

An extensive set of 2D IR spectra of DNA backbone modes has been recorded for salmon testes DNA in aqueous solution and in thin films with CTMA as counter ions. The data cover a broad range of hydration levels. Structural fluctuations of the hydration shell have a strong impact on the 2D line-shapes and display a correlation decay time of 300 fs, somewhat slower than in bulk water. The water shell exerts very strong electric fields on the DNA backbone with fluctuation amplitudes on the order of 2.5 V/nm. Particularly sensitive to hydration shell fluctuations are the two PO_2 stretching modes of the highly polarizable and directly hydrated phosphate groups in the backbone. The antisymmetric phosphate stretching mode is most sensitive to the fluctuation of the chemical environment. The orientation of the cross peaks in 2D IR indicates that the cross frequency fluctuation correlation between these two phosphate stretching modes is positive. This indicates that the fast electric field fluctuation of water molecules around the phosphate group is mainly along its C2 axis or the radial direction of

DNA.

For hydrated DNA, the population decay of backbone modes below 1100 cm^{-1} is accelerated and contributes to the homogeneous broadening of their vibrational lineshapes. This effect is, however, smaller than the increment of homogeneous broadening with growing hydration level, again showing that the fast structural fluctuations of water are the predominant broadening mechanism, as dicussed in more detail in Ref. [91]. This conclusion is in agreement with simulation work for short time scales.[31, 87]

6. 2D IR SPECTRA OF ARTIFICIAL DNA OLIGOMERS IN DIFFERENT IONIC WATER SOLUTIONS

In Chapter 5, the backbone modes of salmon testes DNA, a native long DNA helix, have been studied at different hydration levels. Here, artificial double-stranded DNA oligomers containing 23 adenine-thymine (AT) base pairs are embedded in an aqueous environment containing different positively charged ions at different concentrations. This approach gives information on a potential influence of the ions on the structural dynamics of the hydration shell.

The samples are prepared by dissolving AT23 DNA (concentration c$\approx 1.3 * 10^{-2}$ M) in aqueous solutions of NaCl or $MgCl_2$. The weight ratio of DNA and water is controlled to maintain a hydration level of 145 water molecules per b.p. The concentration of $MgCl_2$ was 1 M, while the NaCl concentration was 0.1 M or 3 M. These ionic concentrations are used to implement the same ionic strength in the different samples. NaCl and $MgCl_2$ fully dissociate in the aqueous environment, i.e., the cations and anions are separately solvated in the liquid.

The experimental setup and conditions in measuring 2D IR spectra are the same as in the former Chapter 5. In particular, all pulses are of parallel linear polarization and reorientation processes of transition dipoles are not studied.

6.1 Results and discussion

The linear infrared absorption spectra of the different DNA solutions in 8 to 11 μm wavelength range are presented in Figure 6.1. There are small differences in individual lineshapes while the transition frequencies of the different backbone modes remain unchanged. The presence of Mg^{2+} ions seems to introduce a slight broadening in the absorption spectrum.

The 2D IR spectra of DNA in the 0.1 M NaCl solution are shown in Figure 6.2 for waiting times between 250 to 1500 fs. The corresponding set of spectra of DNA in a 1.0 M $MgCl_2$ and a 3.0 M

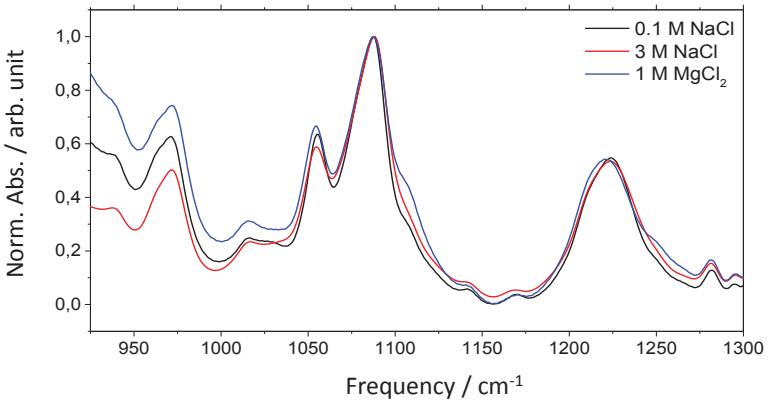

Fig. 6.1: FT-IR spectra of AT23 DNA in different salt aqueous solutions

NaCl solution are presented in Figure 6.3 and Figure 6.4, respectively. The overall pattern of diagonal and cross peaks is similar to the 2D IR spectra of salmon testes DNA in Chapter 5. Differences in lineshape of diagonal and cross peaks are minor for the different counterions. There is no apparent sign of spectral diffusion in the time window up to waiting times of 2 ps, again similar to the data for salmon testes DNA. Compared to the case of the DNA/CTMA film samples, the diagonal peaks in the solution-phase spectra display a smaller spectral width along the diagonal, pointing to less inhomogeneous broadening, and a somewhat enhanced width along the antidiagonal.

The 2D IR spectra show that counterions of different charges have a minor influence on lineshapes and, thus, on the frequency spectrum of structural fluctuations of hydrated DNA. This observation is surprising given the pronounced Coulomb interaction of counterions with their environment and the phenomenon of counterion condensation close to the DNA surface, i.e., an enhanced local ionic concentration at small radial distances from the DNA surface. It is important to note, however, that the concentration of water molecules close to the DNA surface is always higher than that of counterions, i.e., there are strong local electric fields originating from the dipolar water molecules.

Quantum chemistry simulations suggest that there are two ways in which the Na^+ and Mg^{2+} cations interact with the PO_2^- group in the model system $H_2PO_4^-$.[92] One is called direct contact binding of the partially hydrated cations with the anion; the other is through water association. These two types of interaction are competitive with each other, with water binding being the preferred mechanism. X-ray scattering data suggest enhanced counterion concentrations in a cylindrical volume of 1 nm radius around DNA, embedded in an environment of water molecules at higher concentrations.[23, 24] A minor fraction of counterions is placed in the minor groove of the DNA surface. The molecular dynamics simulation work on B-DNA in solution also shows a very similar

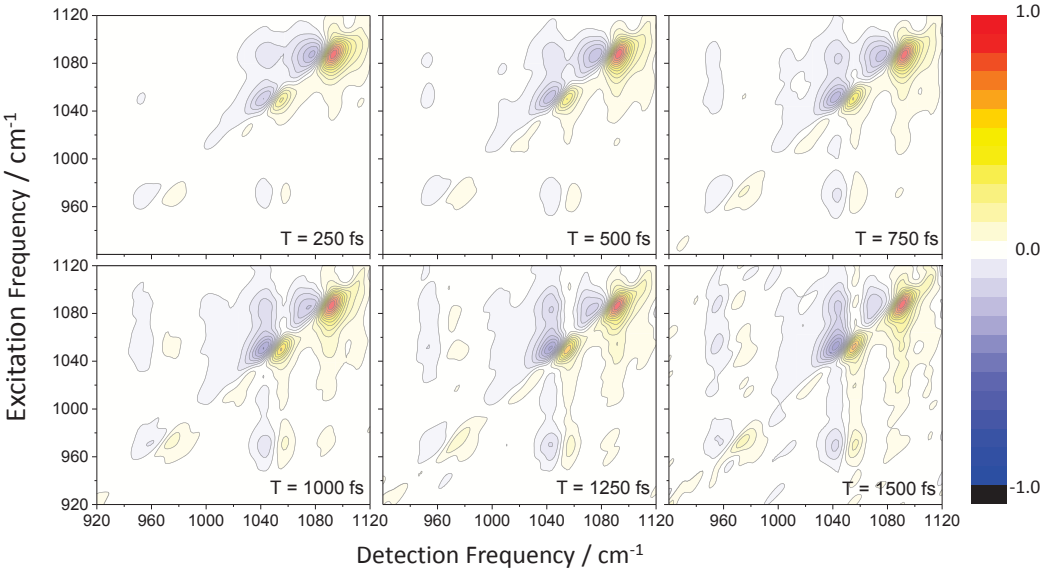

Fig. 6.2: 2D IR spectra of AT23 DNA in 0.1 M NaCl solution. The amplitude of each plot is scaled to the specific maximum of the 2D IR plots at every waiting time.

water and counterions distribution.[93] For the more distant counterions, the water molecules screen their Coulomb forces on the DNA very effectively, even at the terahertz fluctuation frequencies of the system.[39, 87] Moreover, the partial delocalization of the net charge on the phosphate group makes its interaction with the counterions less strong than localized charges. As a result, the partially charged oxygen atoms of water molecules compete with the phosphate groups when it comes to the charge-charge interaction with the positively charged counterions. Three-site water models used in molecule dynamics simulation also support this picture, with a partial charge of +0.4e on the water hydrogen atoms and -0.8e on the oxygen atom.[94]

The phosphate groups of the backbone are hydrated by up to 6 water molecules forming strong hydrogen bonds with the PO_2^- oxygens.[19] Such water molecules are the main source of electric fields exerted on the phosphate groups and the structural fluctuations of this local hydration shell rather than the counterions determine spectral diffusion as manifested in the 2D lineshapes. This picture is in line with simulation work on the contribution of water and ions to the transient Stokes shift of electronic chromophores attached to DNA,[87] suggesting that two thirds of the emission Stokes shift within the first 10 ps originate from water reorientation. According to this work, the contribution of counterions is less than 10%. Further work from Furse and Corcelli also shows a very similar minor and flat contribution of the counterions in their nonequilibrium molecular dynamics simulation.[89, 90, 95]

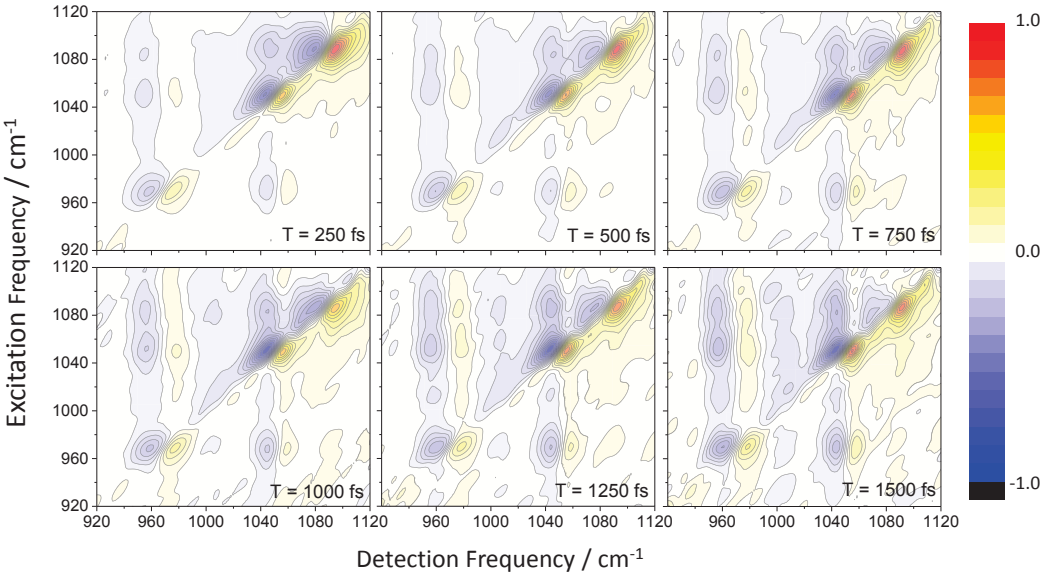

Fig. 6.3: 2D IR spectra of AT23 DNA in 1 M $MgCl_2$ solution. The amplitude of each plot is scaled to the specific maximum of the 2D IR plots at every waiting time.

In addition, molecular dynamics simulations have been carried out to the ion residence time around DNA.[96, 97] Kowalczyk and coworkers found that the Na^+ has a residence time more than 20 ps around DNA.[96] It should be noticed that they underestimated the residence time constant by using a static dielectric constant of water. Actually, the dielectric constant of water is a function of the frequency of the electric field. In 50 GHz or higher frequency region, its real part is less than 10 and its imaginary part less than 15.[27, 28, 98] The simulation in this work has not taken this into consideration and underestimates the Coulomb interaction between DNA and the counterions. Using a CHARMM force field, Jejoong Yoo and Aleksei Aksimentiev found that the most significant difference between Na^+ and Mg^{2+} happens on some 1 ns level.[97] In the case of Mg^{2+}, long-lived contact (>500 ps) contributes more than half of the cumulative residence time. However short-lived contact (10 to 500 ps) contributes to the cumulative residence time of Na^+as well. So a time window of 2 ps is not enough to distinguish the dynamics of different counterions in the hydration shell.

Although the electrostatic interaction is a long-range interaction, this does not mean that the electric field fluctuation felt by the probe are also long-range. The range over which fluctuationing fields act, decays more faster than the electrostatic interaction when more molecules are introduced into the solvation shell, defining a spatial range shorter than that of the mean electrostatic interaction.[87] The spectral broadening and its dynamical behavior are determined by fluctuations of the electric field. This is why we only get information about the fluctuation of inner hydration shell, but no long-range information.

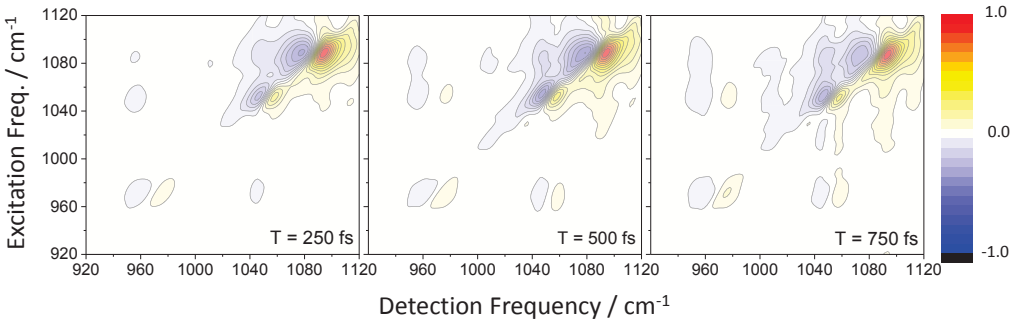

Fig. 6.4: 2D IR spectra of AT23 DNA in 3 M NaCl solution. The amplitude of each plot is scaled to the specific maximum of the 2D IR plots at every waiting time.

6.2 Conclusions

As a result of the competition between local hydration and the Coulomb interaction with the delocalized charge in the phosphate group of DNA, the counterions tend to interact with the phosphate groups via their primary hydration shell even in the crystal structure. This makes the interaction between water and DNA backbone determine the main feature of the fast fluctuation of the electric field around the probing backbone modes. This is why the influence of counterions is not mapped onto the 2D lineshapes.

Part II

PUMP PROBE EXPERIMENT ON DNA

7. FEMTOSECOND PUMP-PROBE EXPERIMENTS WITH RESONANT EXCITATION OF DNA BACKBONE STRETCHING MODES

The 2D IR experiments reported in the previous chapters are complemented by spectrally resolved two-color pump-probe experiments to map population kinetics and the underlying relaxation and/or energy transfer processes. In the first set of measurements discussed in this chapter, backbone stretching modes are resonantly excited by a femtosecond infrared pulse, and the resulting change of vibrational absorption is measured on the same vibration (quasi-one-color experiment) or other backbone vibrations. In the latter two-color experiments, vibrational modes in the range from 1040 to 1120 cm^{-1} are excited and absorption changes at lower frequencies between 900 and 1020 cm^{-1} are recorded.

7.1 DNA samples and experiment

Two types of DNA samples are studied, a DNA film containing double-stranded AT23 oligomers at hydration levels of 0% r.h. and 92% r.h., as well as salmon testes DNA in a 0.1 M NaCl water solution. Figure 7.1 shows the linear infrared absorption spectra of the samples together with the spectra of the pump and probe pulses employed in the different experiments. The pink and orange dashed lines are the spectra of the pump pulses used in the quasi-one-color measurements, while the blue dashed line shows the spectrum of pump pulses used in the two-color studies. In the two-color measurements, a direct excitation of the R1 and R2/L3 modes is negligible.

Similar to the 2D IR experiment, the polarization of the probe beam is parallel to that of the pump beam. Pump-probe anisotropies and, thus, reorientation processes of vibrational transition dipoles have not been studied. Frequency-integrated cross-correlation functions of pump and probe and the delay zero in the experiments are determined via two-photon absorption of a 100 μm thick InSb crystal. The full width at half maximum of the cross-correlation function has a value of approximately 200 fs.

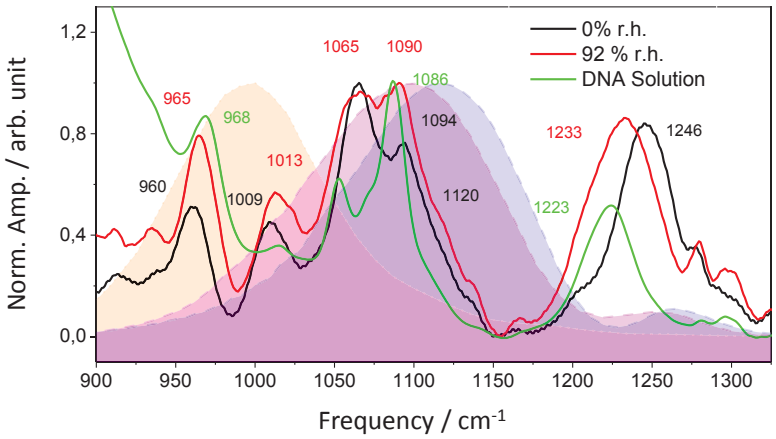

Fig. 7.1: Spectra of pump pulses used in the pump-probe experiment to gather with the spectra of AT23 film and salmon test DNA in 0.1 M NaCl solution. The pink and the orange dashed lines are the spectrum of pump pulse used in the direct pump probe experiment; while the blue dashed line shows the spectrum of pump pulse used in the two-color experiment.

7.2 Results and discussion

Transient pump-probe spectra of the DNA CTMA film at 0% r.h. and 92% r.h. are shown in Figures 7.2 and 7.3, together with time-resolved traces recorded at several fixed probe frequencies. The corresponding data set for salmon testes DNA in solution is presented in Figure 7.4. The transient spectra in the quasi-one-color scheme shown in Figures 7.2 7.3 7.4 A, B display a sequence of negative (absorbance change $\Delta A < 0$) and positive ($\Delta A > 0$) peaks. The negative signals originate from the ground state bleaching and stimulated emission on the v=$|0\rangle \rightarrow |1\rangle$ transitions of the vibrations, while the positive peaks represent the anharmonically red-shifted transient v=$|1\rangle \rightarrow |2\rangle$ absorption. Due to the comparably small spectral separation of the different fundamental transitions, the positive and negative signal components partly overlap and compensate each other.

All absorption changes recorded at fixed probe frequencies in the quasi-one-color scheme display a decay on a time scale of first 5 to 10 ps and a long-lived residual signal. The first component at 1098 cm^{-1} decays clearly faster than the others, as is evident from the time traces in Figures 7.2A and 7.3A. Consequently, the transient signal around 1120 cm^{-1} shoulder becomes significant after 1 ps. The slow signal component decays on a 5-20 ps time scale for the dehydrated case (0% r.h.) while there is no long-lived signal apparent at 92% r.h. hydration level.

The two-color data in Figures 7.2C and 7.3C exhibit absorption changes of modes at lower fre-

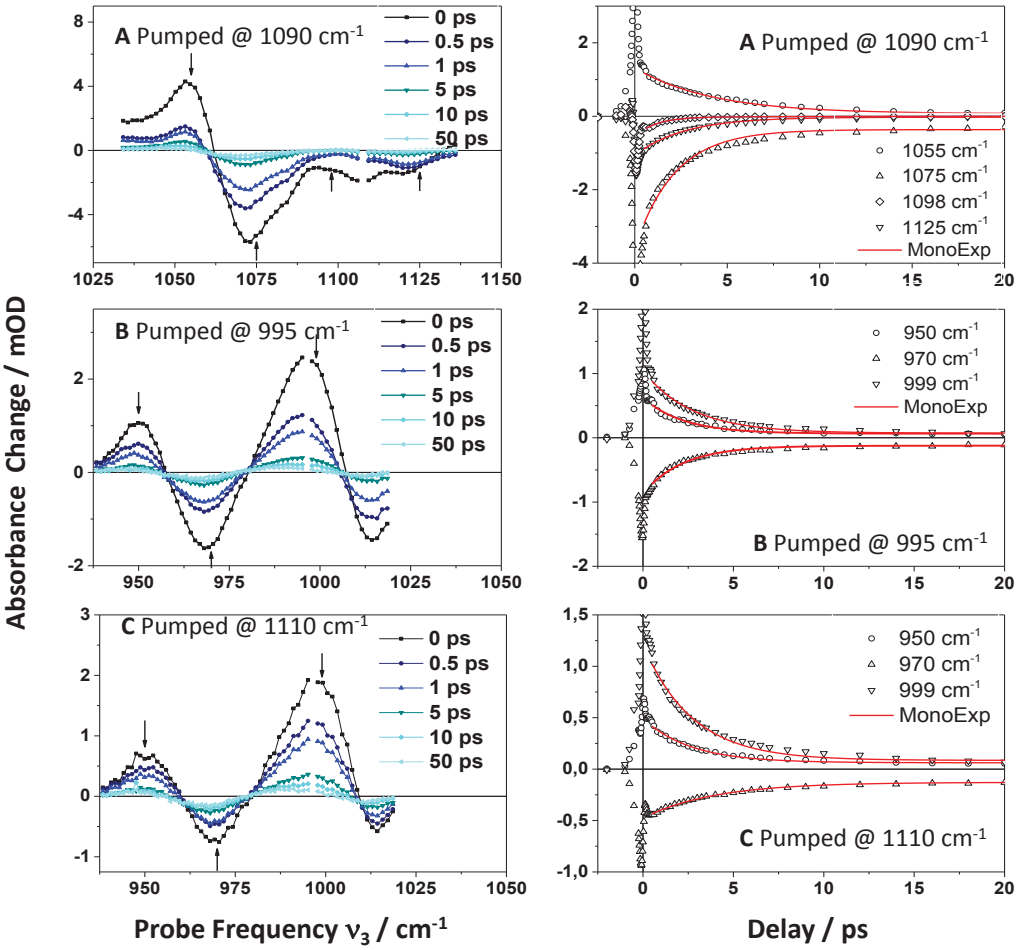

Fig. 7.2: Transient pump-probe spectra and traces at selected probe frequencies of 0% r.h. DNA after backbone modes excited. (A) Pumped at 1090 cm^{-1}; (B) pumped at 995 cm^{-1}; (C) pumped at 1110 cm^{-1}. The time constants obtained from the fitting process are listed in Table 7.1.

quencies rising around delay zero although such vibration modes are not directly excited by the pump. This behavior is caused by the anharmonic coupling of such modes to the directly excited modes with higher frequency, i.e., it gives evidence of intermode couplings mediated through higher-order terms in the vibrational potential. The transient spectra reveal a coupling-induced red-shift of the modes at lower frequencies, causing the positive absorption changes. This behavior is in line with the cross peak pattern in the 2D IR spectra. The spectral position of the maximum ground state bleaching around 970 cm^{-1} slightly red-shifts with increasing delay time. This finding together with the nonzero offset after 50 ps suggest some heat-induced signal at late delay time.

The pump-probe data for salmon testes DNA in solution are shown in Figure 7.4. While the general behavior is similar to the DNA oligomer data, there is a background signal from the thermal response of the surrounding water, affecting the amplitudes in the transient spectra. In the spec-

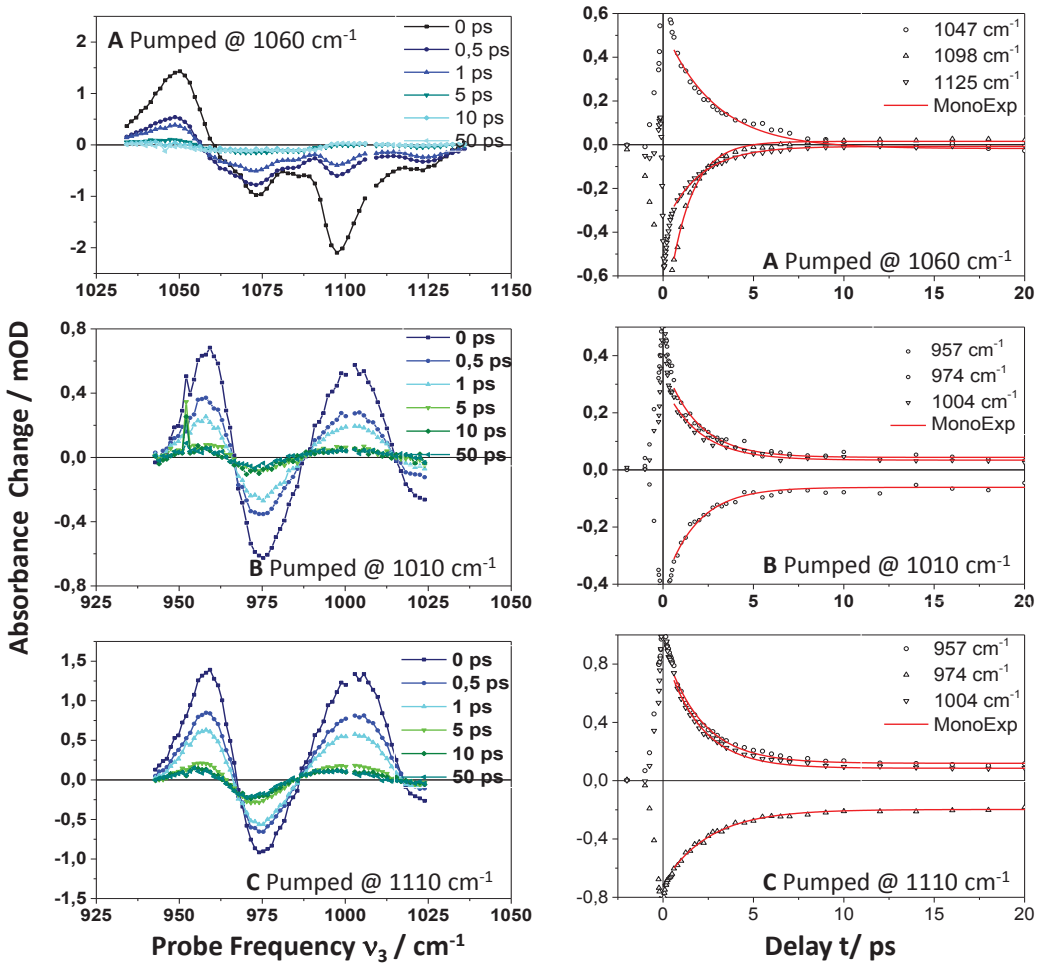

Fig. 7.3: Transient pump-probe spectra and traces at selected probe frequencies of 92% r.h. DNA after backbone modes excited. (A) pumped at 1060 cm^{-1}; (B) pumped at 1010 cm^{-1}; (C) pumped at 1095 cm^{-1}. The time constants obtained from the fitting process are listed in Table 7.1.

tral range shown, water displays a broadband librational absorption, i.e., a small part of the pump pulse is absorbed by water directly. The librational absorption undergoes a red-shift upon vibrational heating.[99, 100] The red-shift builds up within the time resolution of the experiment as the initial librational excitation decays on a sub-100 fs time scale. This thermal signal persists for delay times much longer than the range studied here.

The v=1 lifetimes of the backbone modes are obtained from single exponential fits of the initial decays in the time-resolved quasi-one-color pump-probe transients. The time constants are summarized in Table 7.1 and plotted in Figure 7.5. All the backbone stretching modes have a lifetime of between 1.0 to 4.4 ps. The symmetric phosphate stretching mode P2 has the shortest lifetime of approximately 1 ps, consistent with the temporal behavior of the transient spectra. An increase in hydration level influences the vibrational lifetimes differently: for the symmetric phosphate mode P2,

Tab. 7.1: Time constants from single exponential fitting of the traces of pump-probe transient spectra of DNA CTMA film

0% r.h.	Probe Freq./ cm^{-1}	950	970	999	1055	1075	1098	1125
Direct pump	lifetime/fs	2230	2190	2710	4190	2150	1190	2620
	Std. Error/fs	162	116	137	199	128	44	104
Two Color	lifetime/fs	2620	3930	2710				
	Std. Error/fs	114	120	129				
92% r.h.	Probe Freq./ cm^{-1}	957	974	1004	1047	1073	1098	1125
Direct pump	lifetime/fs	1850	1810	1960	2810	1590	1240	1930
	Std. Error/fs	113	118	112	175	69	38	44
Two Color	lifetime/fs	2040	2510	1950				
	Std. Error/fs	79	92	73				

the variation in lifetime is relatively small, while the change is much more significant for the 960, 1050 and 1125 cm^{-1} modes. The exact origin of this behavior is unknown.

Tab. 7.2: Time constants from single exponential fitting of the traces of pump-probe transient spectra of salmon testes DNA in 0.1 NaCl solution

Probe Freq./ cm^{-1}	960	977	1006	1046	1098	1124
lifetime/fs	1660	1190	1670	1890	1040	1470
Std. Error/fs	108	179	226	71	67	163

The decay times derived for the lower-frequency modes from the two-color data, i.e., for non-resonant excitation at high frequencies, are systematically longer than with resonant pumping. This behavior is a signature of population transfer from the directly excited high-frequency modes to the vibrations at lower frequency. The transfer typically occurs with picosecond time constants and, thus, results in a delayed feeding component in the pump-probe signals at lower frequency. This result is in agreement with the waiting time evolution of the cross peaks in our 2D IR data in Chapter 5. The theoretical analysis of the 2D IR spectra presented in Ref.[81, 91] and the present pump-probe data gives population transfer times on the order of 1-2 ps. The underlying intermode couplings are on the order of 10 cm^{-1}.

In order to figure out the origin of the nonzero long-lived offset of the transient spectra of the DNA/CTMA film at late delay time, we compare it with the temperature dependent stationary infrared

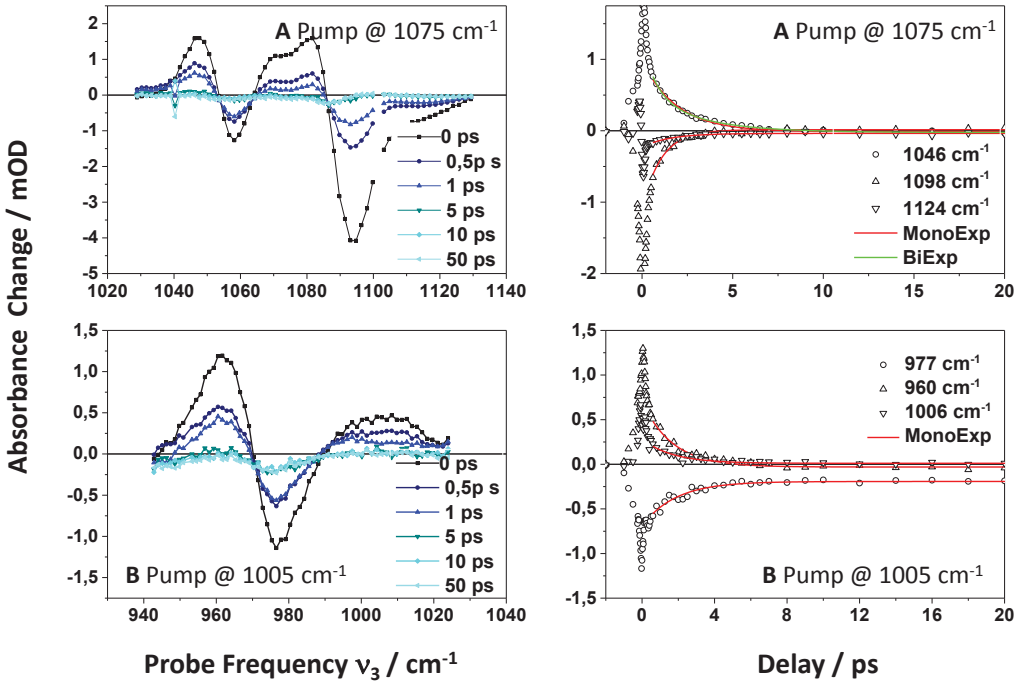

Fig. 7.4: Transient pump-probe spectra and traces at selected probe frequencies of Salmon Test DNA solution after backbone modes excited. (A) pumped at 1075 cm^{-1}; (B) pumped at 1005 cm^{-1}. The time constants obtained from the fitting process is listed in Table 7.2.

absorption spectra in Chapter 4. The latter display similar features, i.e., a blue shift of the phosphate band and a red shift of the other bands. We conclude that the long-lived pump-probe signals are of thermal origin. In a vibrationally heated ground state, low-frequency modes are populated which couple anharmonically to the backbone stretching modes studied here. This coupling gives rise to spectral shifts of the v=0 to 1 transitions of the backbone stretching modes. In the case of dehydrated DNA (0% r.h.), the relevant low-frequency modes belong to the vibrational manifold of the DNA itself. Energy dissipation along the double helix reduces excess populations localized around the initially excited backbone oscillators and leads to the observed decay on a 20 ps time scale. In contrast, a joint heated ground state of DNA and its water shell is formed at higher hydration level and/or in aqueous solution which only decays by heat diffusion on a microsecond time scale.

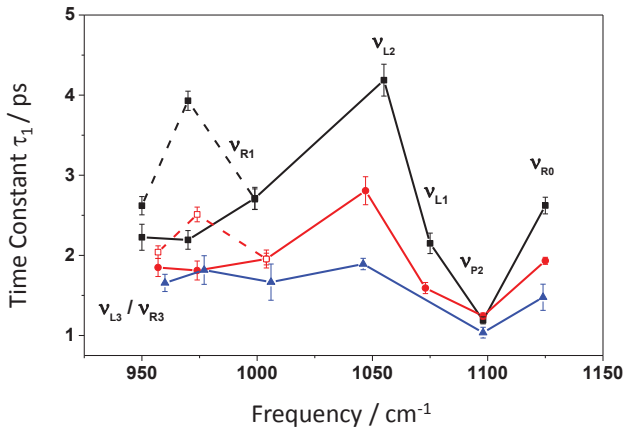

Fig. 7.5: Comparison of the lifetimes of DNA backbone modes from single exponential fitting under different experiment conditions. Those of the dehydrated DNA film are shown in black squares, and hydrated AT23 DNA film in red square. The directly pumped case, the lifetime constants are shown in solid symbols with solid line and indirect in empty symbols with dashed line, for the case of salmon test DNA solution, the lifetime constants are plotted in blue triangle.

7.3 Conclusions

A set of pump-probe experiments are carried out to investigate the population relaxation of DNA backbone stretching modes and the coupling between them on DNA sample with different hydration levels. The data provide evidence for intermode anharmonic couplings and population transfer from backbone modes at higher frequency to those at lower frequency. This behavior is favored by the delocalized character of the backbone normal modes. Vibrational lifetimes display moderate changes as a function of water content. The microscopic origin of this behavior is unknown and needs further investigation. There are long-lived pump-probe signals which are of thermal origin. Three mechanisms contribute to this effect: A temperature rise of the water shell weakens hydrogen bonds between water molecules and the PO_2^- oxygens, leading to a blue shift of the P2 mode. Heating of the water shell is connected with a limited spatial rearrangement of water molecules and a concomitant change of the electric field acting on the backbone oscillators. This effect results in spectral shifts as well. The second mechanism consists in the anharmonic coupling of low-frequency modes of DNA and the surrounding water shell to the backbone stretching modes in the spectral range studied here. Thermal excess populations of low-frequency modes result in spectral shifts and potentially changes of transition dipoles of the backbone modes. So far, the most relevant low-frequency modes and their excess populations are unknown. Methods such as time-resolved anti-Stokes Raman scattering can grasp such excess populations and characterize the low-frequency heat bath in more detail.

8. ENERGY EXCHANGE BETWEEN THE WATER SHELL AND DNA STUDIED IN WATER-PUMP/BACKBONE-PROBE EXPERIMENTS

Energy exchange between DNA and its water shell is understood only in part. While the formation of vibrationally hot ground states after relaxation of DNA and water vibrations and the general heat sink function of the water shell are known, the time scales and mechanisms of energy exchanging between the double helix and its aqueous environment represent important open questions. In particular, the pathways of energy transfer from the backbone into the water shell and vice versa are unknown, raising, e.g., the question which parts of the backbone couple how strongly to water degrees of freedom. In this chapter, we report experiments in which the water shell is excited via its OH stretching absorption and the response of the backbone modes is probed. The relaxation of the OH stretch vibrations establishes a hot ground state in the water shell which couples to the DNA and changes its energy content via energy transfer processes. As a benchmark, measurements at a low hydration level of less than two water molecules per base pair (b.p.) are performed. Here, the infrared absorption at 3450 cm^{-1} is dominated by the NH stretch vibrations of the base pairs rather than by water.

8.1 Experiment

Pump and probe pulses are generated in two home-made two-stage OPA systems pumped by femtosecond pulses from a commercial Ti:sapphire regenerative amplifier. The energy of the pump pulses is about 1.6 μJ. In order to pump water and at the same time avoid absorption by the CH stretching modes of DNA and its CTMA counterions, we center the spectrum of the pump pulse at 3450 cm^{-1} with a bandwidth of 300 cm^{-1}. Under this pump condition, 3 to 4 percent of the water molecules in the interaction region are excited. The final temperature jump is estimated to be some 20 K at maxima. The probe pulses have a tuning range from 950 to 1150 cm^{-1} with a duration of 150 fs. The spatial and temporal overlap of pump and probe pulses are optimized by measuring the 3-photon absorption signal of a 100 μm thick Ge plate.

Natural salmon testes DNA is studied in this experiment. To generate a thin film of high optical quality, the counterion Na^+ are exchanged by CTMA. The DNA/CTMA complexes are cast on a BaF_2 window and packaged in a home-made humidity cell to control the hydration level of the sample. Measurements were performed at 0% r.h. and 92% r.h., corresponding to a water concentration in the film of less than 2 and more than 20 water molecules per b.p. Salmon testes DNA with Na^+ counterions are dissolved in a 0.1 M NaCl solution in water with approximately 140 water molecules per b.p., i.e., under conditions of full hydration. The linear infrared absorption spectra of the different samples are presented in Figure 8.1.

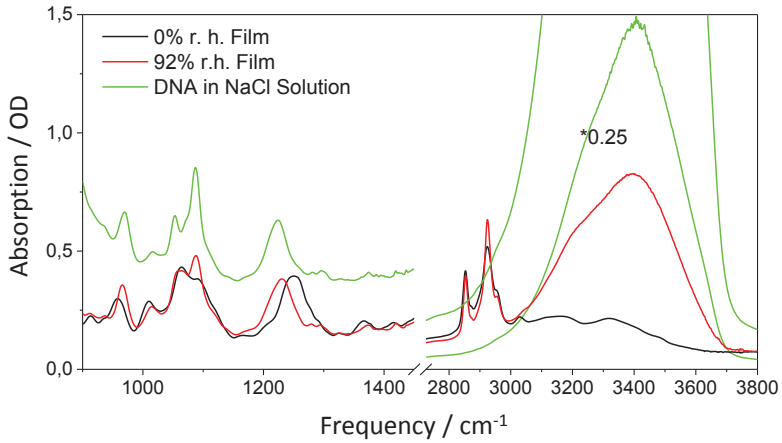

Fig. 8.1: Linear infrared absorption spectra of salmon testes DNA at different hydration levels.

8.2 Results

Transient spectra of backbone modes measured in the range from 940 to 1125 cm^{-1} after excitation centered at 3450 cm^{-1} are shown for several selected time delays in Figures 8.2A (0% r.h.), 8.3A (92% r.h.), and 8.4A (DNA in solution). The spectra recorded at the low hydration level of 0% r.h. reflect the response of the DNA backbone modes only, while both the backbone stretching modes and high-frequency water librations contribute to the absorption changes observed at the two higher hydration levels. Transient spectra of a thin film of neat water (about 6 μm thick) measured under the same experimental conditions (Figure 8.5) display a spectrally broad enhancement of absorption at early delay times which decays within the first 4 ps to a negative residual absorption change.

The backbone contributions to all transient spectra consist of a sequence of negative and positive peaks. In the 0% r.h. spectra, three negative peaks are distinguished around frequency positions

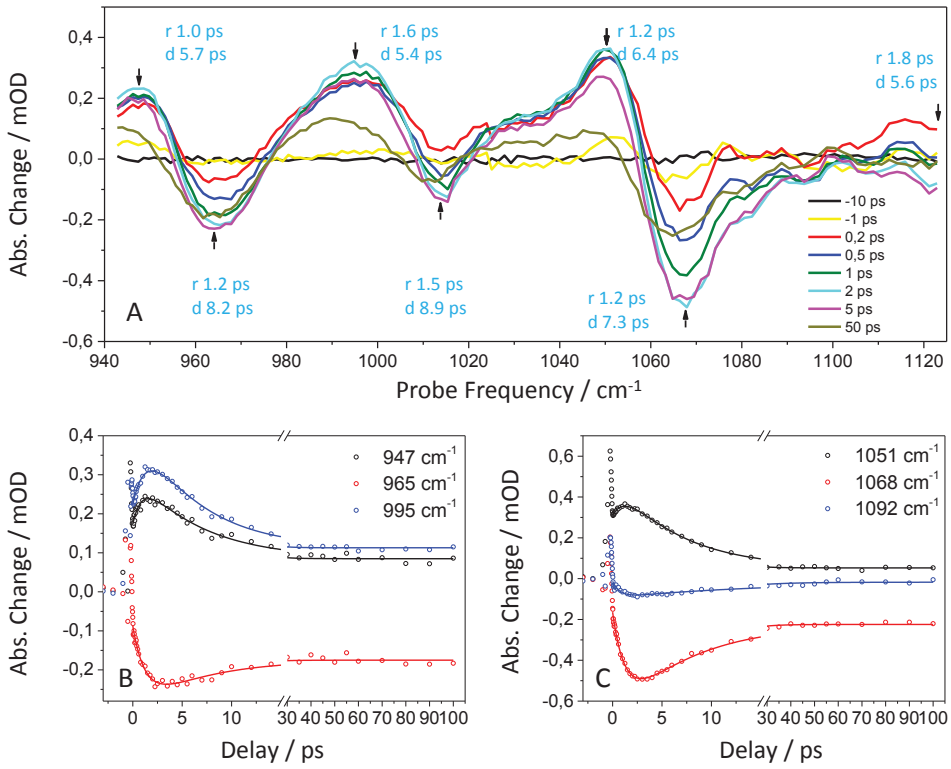

Fig. 8.2: (A) Transient spectra of DNA backbone modes at selected delay times in 0% r. h. salmon testes DNA CTMA film. (B,C) Time resolved pump-probe traces at selected probe frequencies. The frequencies where the traces are taken are marked with arrows in panel (A). The traces are fitted using double exponential decays with time constants labeled in panel (A) around the frequency component they belong to and listed in Table 8.1.

of 965, 1015, and 1070 cm^{-1}. Such frequencies correspond roughly to the absorption maxima in the linear infrared spectrum, except for the absorption band at 1090 cm^{-1}, the phosphate P2 band, which is not obviously distinguished in the transient spectra. In contrast, the spectra at the two higher hydration levels (92% r.h. and solution) display four negative peaks including a distinct peak at the position of the P2 band. The negative peaks give evidence of an absorption decrease at the initial frequency positions of the v=0 to 1 transitions of the underlying vibrations. The positive peaks can in principle originate from pump-induced spectral shifts of the v=0 to 1 transitions, a hallmark of anharmonic vibrational couplings, or from transient populations of the v=1 and higher states of individual vibrations. In the present pump-probe scheme, there is no direct excitation of backbone modes to their v=1 states and, thus, the latter contribution is minor. The absorption changes observed at time delays longer than 3-4 ps represent solely spectral shifts of vibrational v=0 to 1 transitions. The transient spectra at 92% r.h. and in solution exhibit a broad positive feature above 1100 cm^{-1} at early delay time, which is absent in the dry DNA film.

Tab. 8.1: Parameters obtained from double exponential fitting of the traces of 3 μm pump/backbone probe experiment of dehydrated DNA CTMA film.

Probe Freq./cm^{-1}	A_0/mOD	A_1/mOD	t_1/ ps	A_2/mOD	t_2/ ps
947	0.076	-0.181	1.0	0.240	5.7
965	-0.163	0.219	1.2	-0.097	8.2
996	0.098	-0.293	1.6	0.385	5.4
1114	-0.049	0.172	1.5	-0.122	8.9
1051	0.069	-0.235	1.2	0.435	6.4
1068	-0.210	0.541	1.2	-0.403	7.3
1121	-0.034	0.284	1.8	-0.183	5.6

Tab. 8.2: Parameters obtained from double exponential fitting of the traces of 3 μm pump backbone probe experiment of hydrated DNA CTMA film

Probe Freq./ cm-1	A_0/mOD	A_1/mOD	t_1/ps	A_2/mOD	t_2/ps
970	-1.12	0.73	0.9	0.12	17
1056	-0.58	0.56	1.04	0.12	17
1085	-0.80	0.31	0.9	0.12	17
1099	0.22	0.34	1.0	-0.07	21

Figures 8.2 B,C (0% r.h.), 8.3 B,C (92% r.h.), and 8.4 B,C (DNA in solution) summarize time-resolved traces of the absorption change measured at fixed spectral positions. The time-dependent absorption changes were numerically analyzed by fitting exponentially rising and decaying kinetics to the experimental data. The time constants and respective amplitudes of the exponential terms are summarized in the Tables 8.1, 8.2, and 8.3. The traces from the data set for 0% r.h. are well reproduced by a rise time of approximately 1.2 ps and a single decay component with time constants between 5.5 and 9 ps depending on the spectral position. The data for the two higher hydration levels display a larger kinetic variety. For DNA in water solution, the first kinetic component is within the time resolution of the experiment, i.e., the rise of the absorption changes appears 'quasi-instantaneous'. This behavior at early times is dominated by the ultrafast librational response of water after OH stretch excitation. In the two hydrated samples, there is a pronounced signal from the symmetric phosphate stretching mode P2.

In contrast to the case of DNA CTMA film, the transient spectra of DNA in solution have a large background from the response of bulk water. This is evident from the transient spectra in Figure 8.4 A

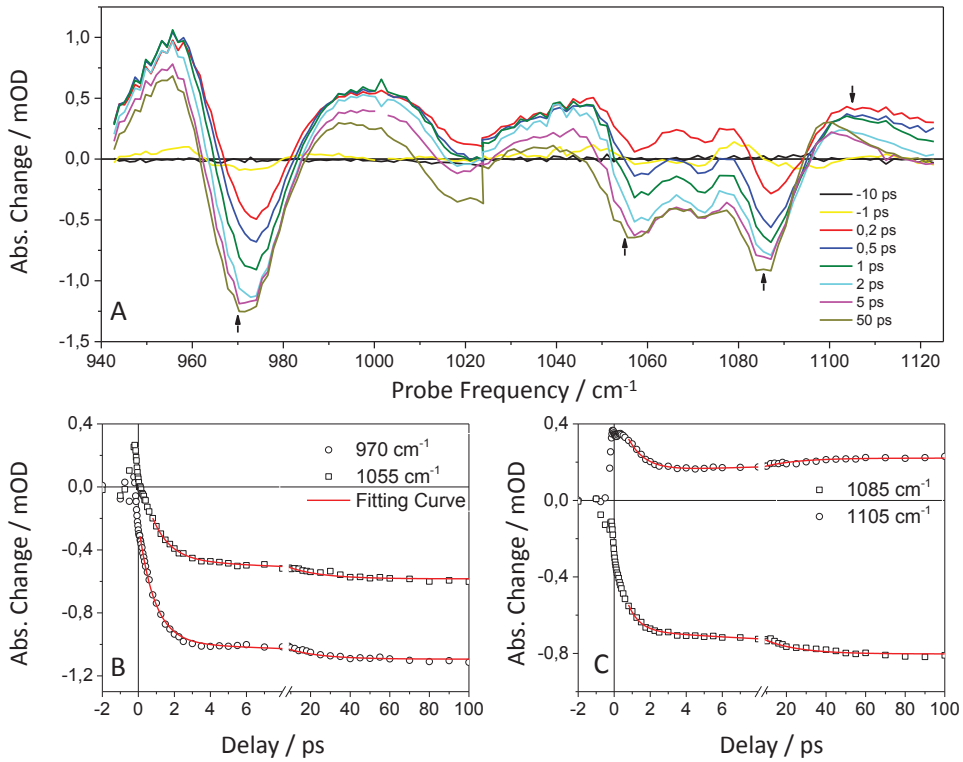

Fig. 8.3: Transient spectra of DNA backbone modes at selected delay times in 92% r.h. salmon testes CTMA film. (A) Transient spectra of salmon testes DNA backbone modes at selected delay time in 92% r. h. CTMA film. (B,C) Pump-probe traces at selected probe frequencies which are marked with arrows in panel (A). The traces are fitted using double exponential decay with time constant listed in Table 8.2.

and 8.5 A. The 1 ps process is due to the formation of a hot ground state in the aqueous environment.

8.3 Discussion

The pump pulses around 3450 cm^{-1} excite the water shell via its OH stretching band and/or the DNA base pairs via their NH stretching bands. At 92% r.h. and in water solution, the OH stretch absorption and, thus, water shell excitation strongly dominates (cf. Figure 8.1) whereas infrared absorption at low hydration originates mainly from the NH stretching vibrations, i.e., direct DNA excitation dominates. There are two basic mechanisms causing absorption changes of backbone stretching modes in the range from 940 to 1125 cm^{-1}:

(i) Relaxation of the initially excited modes occurs in the subpicosecond time domain and generates transient populations of other vibrations being part of the relaxation pathways. Eventually, the energy redistributed in this process is contained in low-frequency modes which display

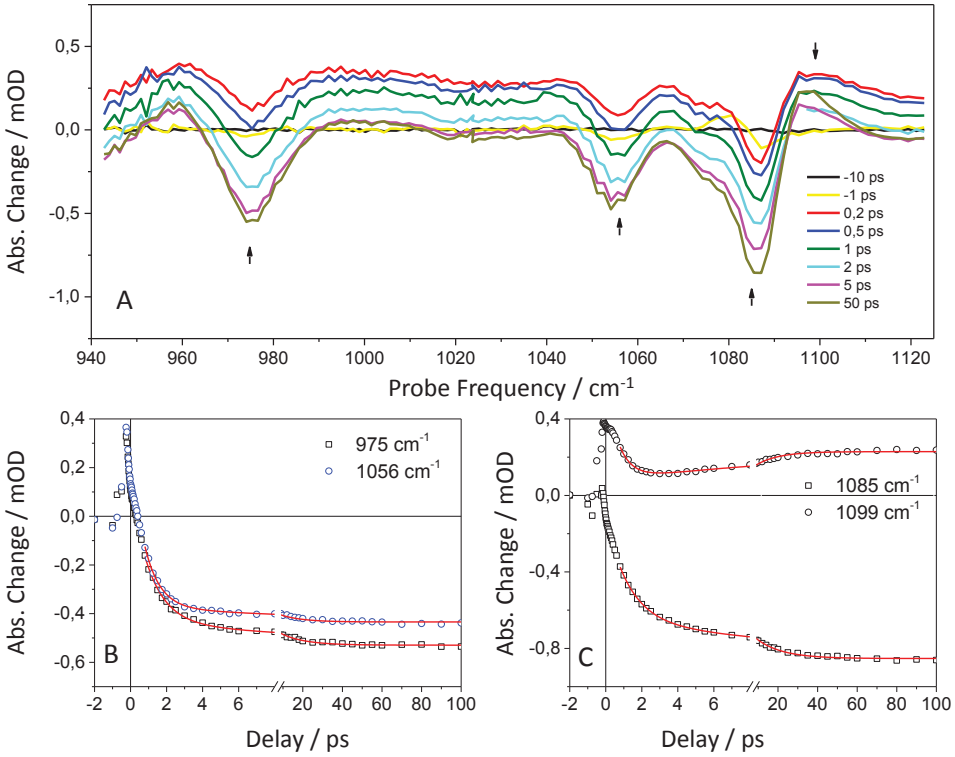

Fig. 8.4: Transient spectra of salmon testes DNA backbone modes at selected delay times in 0.1 M NaCl solution (A) and traces at selected probe frequencies (B) and (C). The frequencies where the traces are taken from are marked with arrows in the up panel (A). The traces are fitted using double exponential decay with time constants listed in Table 8.3. The 'r'and 'd'indicate a rise or a decay process of the transient signal amplitude.

excess populations relative to their initial thermal populations before excitation by the pump pulse. This vibrationally hot ground state has been characterized by an elevated vibrational temperature. Some of the transiently populated modes and/or low-frequency vibrations couple anharmonically to the backbone vibrations and induce frequency shifts of the latter. The sign of the frequency shifts depends on the sign of the anharmonic coupling term. In this scenario, the backbone stretching modes stay in their v=0 state and the transient spectra reveal frequency shifts of the v=0 to 1 transition. There are no experimental indications that the backbone stretching modes studied here are part of the relaxation pathway of the initially excited OH or NH stretching vibrations and, consequently, populations of backbone levels with v≥ 1 are highly improbable.

(ii) The phosphate groups in the backbone and - to a lesser extent - the sugar units form intermolecular hydrogen bonds to water molecules in the first layer. In the heated vibrational ground state, the strength of hydrogen bonds is reduced, resulting in a frequency shift of both backbone and

Tab. 8.3: Parameters obtained from double exponential fitting of the traces of 3 μm pump backbone probe experiment of DNA in 0.1 M NaCl solution

Probe Freq./ cm-1	A_0/mOD	A_1/mOD	t_1/ps	A_2/mOD	t_2/ps
975	-0.53	0.57	1.1	0.10	12
1056	0.43	0.66	0.8	0.07	11
1085	0.85	0.53	1.3	0.20	14
1099	0.29	0.53	0.7	-0.16	11

Tab. 8.4: Parameters derived from double exponential fitting of the traces of 3 μm pump backbone region probe experiment of pure water

Probe Freq./cm^{-1}	A_0 /mOD	A_1 /mOD	t_1/ ps
958	-0.334	0.620	1.0
975	-0.191	0.623	1.1
1002	-0.082	0.588	1.2
1042	-0.077	0.587	1.0
1056	-0.090	0.601	1.0
1085	-0.163	0.616	1.1
1099	-0.199	0.611	1.1
1121	-0.226	0.591	1.2

water vibrations. The rearrangement of water molecules in the heated hydration shell results in a change of the effective electric field the water dipoles generate at the location of the different backbone groups. This change of electric interaction also results in vibrational frequency shifts.

In the following, the results for the different hydration levels are examined in more detail.

8.3.1 Salmon testes DNA/CTMA film at 0% r.h.

The water content of this sample is less than 2 water molecules per base pair, and the linear infrared absorption in the range of the pump pulse is dominated by the NH stretching bands of the base pairs. It should be noted that salmon testes DNA contains both adenine-thymine and guanine-cytosine base pairs with their NH stretching bands in the same spectral range between 3100 and 3500 cm^{-1}. The molar extinction coefficients of NH stretching bands are typically 2.5 times larger than

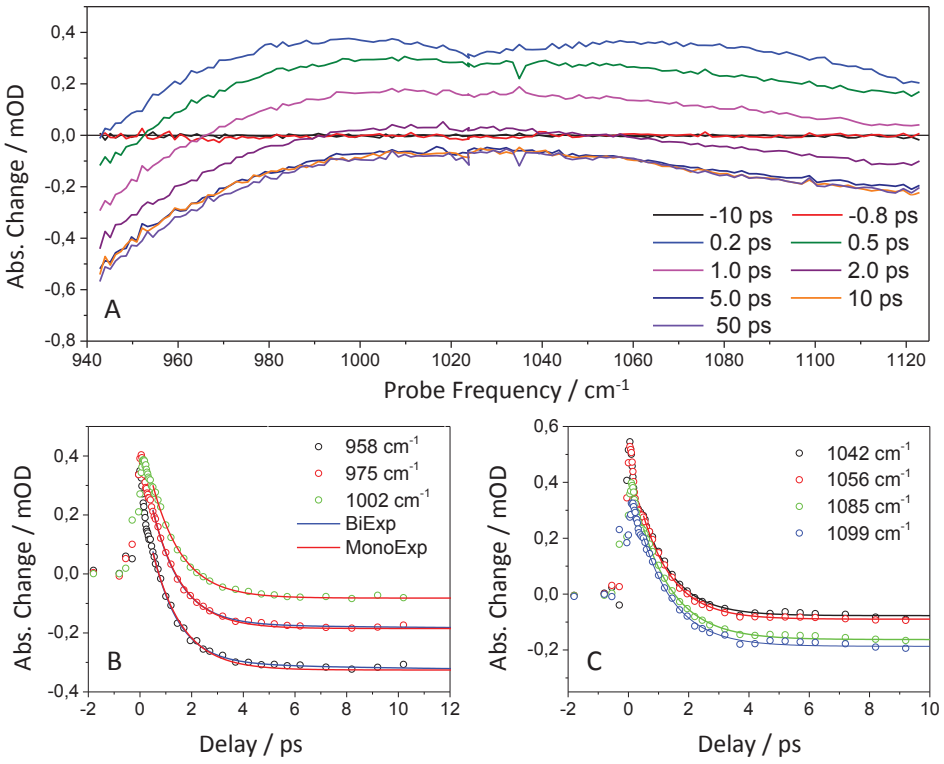

Fig. 8.5: Transient spectra of pure water in 9 μm to 11 μm region. (A) and traces at selected probe frequencies (B) and (C). The traces are fitted using single exponential decay with time constant listed in Table 8.4.

the OH stretch extinction coefficient of water.[101, 102] As a result, the pump pulse predominantly excites the different NH stretching modes to their v=1 states which have a lifetime on the order of 500 fs.[103] Time-resolved resonance Raman studies on adenine-thymine oligomers have shown that the NH stretch excitations decay via fingerprint modes in the range from 1490 to 1660 cm^{-1}, including a pronounced NH bending component.[104] The v=1 states of such fingerprint modes relax on a time scale of a few picoseconds, probably involving a multitude of decay channels into low-frequency modes of the double helix.

The different negative and positive peaks in the transient backbone spectra of Figure 8.2 show a delayed rise with time constants between 1.0 and 1.6 ps. After reaching the maximum amplitude, the positive peaks decay with a time constant of approximately 5 to 6 ps to their positive residual values, while the negative peaks display slower decays with 7-9 ps to negative residuals. All residual absorption changes are long-lived and remain essentially constant up to a delay of 100 ps. The delayed initial rise is due to the finite deposition time of excess energy into the vibrational manifold of DNA, governed by the NH stretch decay and the subsequent relaxation of fingerprint modes in the 1500 to 1700

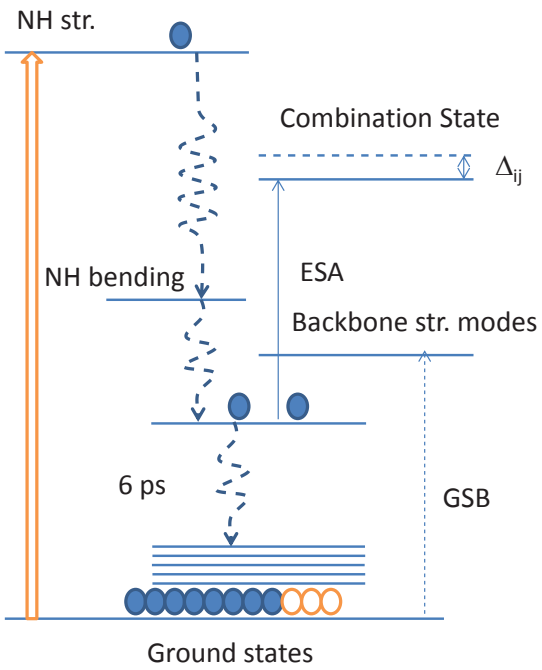

Fig. 8.6: Mechanisms for the population decay of NH and its coupling with the backbone modes in dehydrated film

cm^{-1} range. The fact that the transient backbone signals reach their respective maxima at a delay time of 2.5 ps, i.e., before the relaxation of fingerprint modes is completed, suggests an anharmonic coupling between backbone and fingerprint modes. The subsequent slower decays to the residual values reflect picosecond redistribution processes within the vibrational manifold during which the populations of modes coupling to the backbone vibrations decay. Eventually, low-frequency vibrations with a reduced but nonzero coupling to the backbone modes are populated in a heated vibrational ground state that maintains its character for delay times exceeding 100 ps.

The different intermediate decay times of positive and negative peaks as well as the long-lived positive signals show that transient v=1 populations of backbone modes can be ruled out. If the positive peaks were due to frequency shifts induced by v=1 populations, they should decay with time constants as measured in Chapter 7, in contrast to the experimental results. We conclude that the backbone modes are in their v=0 state at all delay times and the transient spectra reflect spectral shifts and/or a reshaping of the spectral envelopes of the different vibrational bands. The prominent absorption around 1070 cm^{-1} undergoes a red-shift, as suggested by the dispersive spectral feature with a zero crossing around 1055 cm^{-1} region, as shown in Figure 8.2.

8.3.2 Hydrated salmon testes DNA Film

At a hydration level of 92% r.h. corresponding to 20 to 30 water molecules per b.p., the salmon testes double helix is surrounded by roughly two closed water layers. The pump pulse now mainly excites OH stretch oscillators in the water environment whereas NH stretch excitation of the DNA plays a negligible role. The excitation process is spatially unselective, i.e., the excited water molecules are statistically distributed in the two water layers. This is quite similar to the case of DNA in aqueous solution.

In the case of bulk water, the lifetime of the OH stretch excitations is 200 fs and they relax via the v=2 and v=1 states OH bending mode which itself has a v=1 lifetime of 170 fs. In this process, the excess energy of approximately two OH bending quanta is transferred to a librational mode of the excited water molecule and then dissipated into the manifold to low-frequency water modes. The buildup of a hot water ground state occurs with a typical time constant of 1 ps. The neat water spectra and transients in Figure 8.5 represent the response of high-frequency librations in this relaxation scenario. In agreement with previous work,[99] there is a quasi-instantaneous broadband rise of librational absorption, which is a result of anharmonic couplings of librations and the intramolecular water modes, and decays within the first few hundreds of femtoseconds. This initial decline is followed by the build-up of the hot water ground state with a time constant of 1.0-1.2 ps.

After the excitation of the hydration shell, the DNA backbone modes first show a initial rise of 1 ps and a second slower 11 ps rise for DNA in solution or 17 ps rise for 92% r.h. DNA CTMA film. The rise time of the fast component is the same as the formation time of hot ground state of the hydration shell around DNA reported by the phosphate groups.

Similar to the case of dehydrated DNA CTMA film, the relaxation of the OH stretching mode does not get the v=1 states of the backbone stretching mode populated, for there is no decay process in 1 to 3 ps found from the temporal behavior of the transient spectra.

The coupling mechanism between water shell and the DNA backbone mode that makes the vibrational line shapes sensitive to heating of the water environment is of a predominantly electric nature. The DNA backbone is subjected to strong fluctuating electric fields, mainly generated by the dipolar water molecules in the first two hydration shells around DNA. Recent theoretical work suggests an electric field amplitude on the order of 90 MV/cm with a FWHM of 25 MV/cm.[3, 79] Excitation of the OH stretching mode of water molecules in the hydration shell of DNA and the subsequent

formation of the hot ground states change the spatial arrangement of water molecules, and, thus, the electric field acting on the backbone vibrations. Using DMP as a model system, our simulation reveals that there is a change of radical distribution of water molecules around DNA when the temperature varies. When the temperature is raised, the structure of the first hydration shell changes, resulting in a reduction of the electric field exerted on the backbone, in particular on the phosphate groups. This contributes to the blue shift of the vibration frequency of P2 modes and reshaping of the peaks from other backbone modes.

The slow 11 to 17 ps process is assigned to the further thermalization process of DNA hydration shell, in other words, to the further variation of the hydration shell and DNA structure. This comes from the fact that only 3 to 4 percent of the water molecules are excited while there are only ten water molecules in the first two hydration shell of DNA backbone for each phosphate group. In other words, only no more than half of the phosphate groups has their hydration shell heated at early delay time. This makes further spreading of the extra heat becomes possible. The assignment of this slow component is supported by the former study of transient Stokes shift spectra on DNA using dye Hoechst 33258 as a structure probe.[88] The simulation of Furse and Corcelli on TRSS experiment found two processes: one 2.6 ps from water and the other 30 ps from DNA.[89, 90] in this simulation they assigned the experimental 19 ps process to DNA movement. While, here, this 11 to 17 ps process has a chance to get both water dynamics and DNA dynamics involved, it is an average of these two processes.

8.3.3 Comparison between 2D IR spectral diffusion and response of DNA to temperature jumping by excited OH stretching mode of water

Subtracting the contribution of the ETISD, a some 19 ps pure structural diffusion has been obtained for hydrated DNA CTMA film in Chapter 5. This structural fluctuation time constant is very close to the 17 ps further thermalization process obtained here. The question is why we obtain similar time constants when it comes to two different processes here: spectral diffusion and thermal spreading?

Spectral diffusion in 2D IR spectroscopy gives information about the interchanging process between different configurations of phosphate group hydration shell at equilibrated states, i.e. hydration shell fluctuation. While, the 3 μm pump backbone probe used here gives the information about the configuration changing from one equilibrium to another after a perturbation, i.e., information about

perturbation dissipation. These two processes are correlated by fluctuation-dissipation theorem for that the perturbation can also be viewed as a fluctuation, or as the origin of the fluctuation. This theorem connects the linear response relaxation of a prepared non-equilibrium state to its statistical fluctuation in equilibrium. Besides this, the fast population relaxation of the backbone stretching modes forms a perturbation of the chemical environment of DNA backbone. The dissipation of this perturbation makes more DNA backbone modes with different chemical environment involved in the transient spectra, hence also contributes to spectral diffusion. Furse and Corcelli revealed that linear response approximation robust for DNA-Hoechst33258 system.[90] Besides, at room temperature of 300 K, the mean square fluctuation of the temperature is estimated to be 150 K^2, or root mean square fluctuation 12 K. These two facts suggest a very similar behavior for the temperature jumping process to DNA.

In 2D IR experiment, the time window can be used to track the structural fluctuation is limited by the lifetime of the probe mode's excited state. The advantage of the water pump experiment is avoiding the limitation of the short lifetime of the phosphate mode as a probe in 2D IR diffusion spectroscopy. A detailed comparison of these two experimental methods is needed. The fluctuation-dissipation theorem can be used to explain the similarity of the observation from different experiments, where dissipation function of small perturbation in the nonequilibrium process equals fluctuation correlation function in the equilibrium state under linear response approximation.

8.4 Conclusions

In this chapter, we have carried out an experiment study on hydration dynamics of DNA by pumping the NH and OH stretching modes of DNA bases and hydration water. By comparing results for DNA at different hydration levels, water-DNA couplings and time scales of energy transfer are determined. The subpicosecond relaxation of water vibrations establishes a hot water ground state on a time scale of a few picoseconds, in which water molecules slightly rearrange and hydrogen bonds between water molecules are weakened. This structure change is mapped onto the DNA backbone modes by changes in the local electric field the water shell exerts on the backbone. As a result, all backbone modes show a similar picosecond response to water heating, independent of their local hydrogen patterns. Energy transfer from the heated water shell into DNA occurs on a slower time scale of tens of picoseconds.

The temperature jump experiment provides information about structural dynamics manifested

as spectral diffusion in the 2D IR spectra. In contrast to the 2D IR method, the temperature jump approach is not restricted by the lifetime of v=1 state of the probe vibration modes. The influence of counterions with various charge, size and hardness can be resolved using 3 μm pump backbone probe method. A method combining the transient Stokes shift experiment and 2D IR studies of DNA backbone modes as a probe can be implemented, to study the influence of an extra dye molecule on the dynamics of DNA hydration shell.

Transient anti-Stokes Raman spectroscopy can be implemented in the future to figure out the low-frequency fingerprint modes that contribute to the red shift of the phosphate linkage and sugar ring stretching modes in 9 to 11 μm region.

9. CONCLUSIONS

9.1 Concluding remarks

In this thesis, structural dynamics of the DNA hydration shell and molecular couplings between DNA and water have been investigated by femtosecond 2D IR and pump-probe spectroscopy. DNA backbone modes serve as sensitive and noninvasive interfacial probes of DNA-water interactions in a broad range of hydration levels from less than 2 up to approximately 150 water molecules per base pair. The main new results are the following:

(i) An analysis of spatial chirp of the signal field introduced by the transient grating in a four-wave-mixing geometry has been performed. The existence of spatial chirp compromises the heterodyne detection and electric field reconstruction of the signal. Careful alignment of the mirrors in the 2D photon echo setup is needed to avoid the distortion of 2D spectra from imagining aberration.

(ii) An extensive set of 2D IR data allows for characterizing structural dynamics in a time range from 100 fs up to tens of picoseconds and for hydration levels between less than 2 water molecules per base pair and about 150 water molecules per base pair. The fastest decay in the frequency fluctuation correlation function of backbone modes occures with a time constant of 300 fs, reflecting structural fluctuations of the first few hydration layers around the DNA double helix. Compared with the results from the spectral diffusion in bulk water, the dynamics of water in the first few hydration layers of DNA are moderately slowed down, due to steric constraints at the interface and stronger hydrogen bonds between the first water layer and the DNA phosphate groups. The fast correlation decay is followed by slower kinetics in the tens of picoseconds range. The 2D IR lineshapes display a long-lived inhomogeneous broadening even under conditions of full hydration, pointing to a distribution of hydrogen geometries for different hydration sites.

(iii) A large set of femtosecond pump-probe data has been generated with both direct excitation of DNA and excitation of the water shell via its OH stretching absorption. Vibrational lifetimes of backbone modes are in a range between 1 and 4 ps, except for the antisymmetric phosphate stretching

mode with a 300 fs lifetime. Except for the latter mode, the lifetime are moderately shorter at higher hydration levels. The mechanisms behind this behavior are not known yet. After OH stretch excitation of water, a hot ground state of the water shell is formed with a time constant of approximately 1 ps. The resulting change of the hydration shell structure is mapped onto the backbone modes via a change of the electric field exerted by the water shell. This coupling mechanism affects all backbone modes, including those without local hydrogen bonds to water molecules. On a slower time scale of tens of picoseconds, there are energy transfer processes between water and DNA and within the DNA double helix.

(v) A significant advantage of the 3-μm pump experiment over 2D IR studies with resonant backbone excitation is that the time window of the experiment is not limited by the excited state lifetime of the probing modes. This makes it possible to use this method to track processes occurring at long delay times.

(iv) Spectral diffusion in 2D IR spectra gives information about rapid structure changes between different configurations of the DNA hydration shell, while the 3 μm pump experiment gives insight in changes from one configuration to another set of configurations at a higher temperature. In the latter case, the temperature jump can be viewed as a fluctuation or perturbation in the hydration shell. The fluctuation-dissipation theorem can be used to understand the similarity of their time constant. This theorem connects the dissipation of small perturbation in the nonequilibrium process with the fluctuation in the equilibrium system. A complete comparison of these two methods is needed.

9.2 Perspectives and outlook

While the present work has generated detailed unprecedented insight into ultrafast hydration processes of DNA and the underlying molecular interactions, there is room for a range of complementary studies in the future:

(i) Transient anisotropy measurements with hydration shells consisting of isotopically diluted water can give information about reorientation processes of hydration water at different hydration levels and for DNA with different counterions.

(ii) Along similar lines, transient anisotropy measurements on backbone modes in 9 to 11 μm region may resolve the relative transition dipole orientation of different backbone modes and the resonant population transfer between them, together with the influence of the hydration. Information

about inter- and intra- strand population and heat transfer can in principle be resolved by this kind of experiment. A two-color transient anisotropy measurement can be done with isotope diluted sample to investigate the reorientation dynamics of water hydrogen bonding to different hydrogen bond acceptor groups in DNA.

(iii) In all the experiments of this work, there is a thermally induced signal from low-frequency modes that are coupled to the backbone modes in 9 to 11 μm region. In future, IR pump anti-Stocks Raman probe experiments in combination with quantum chemistry calculations may allow for a better characterization of the low-frequency degrees of freedom relevant for this behavior.

(iv) So far, mainly dynamics of hydration water on the DNA surface has been addressed, with little insight into water dynamics in the minor and major groove of the double helix structure. In B DNA, the O4′ of the sugar ring is in the minor groove. Therefore, vibrations involving this functional unit can be used as a probe of structural dynamics in the minor groove of DNA.

(v) Benchmark experiments on dimethyl- and diethyl-phosphate anions in aqueous solution would clarify to what extent such systems mimic the true DNA behavior. Here, both 2D IR and 3 μm-pump/phosphate-stretching probe experiments are of interest.

(vi) Complementary dielectric relaxation spectroscopy on DNA CTMA films at different hydration levels can help to resolve the influence of different DNA sequences on hydration dynamics at a slower time scale and be compared with the results from ultrafast vibrational spectroscopy.

Appendices

Appendix A

CHEMICAL STRUCTURE OF CHEMICALS MENTIONED IN THIS THESIS

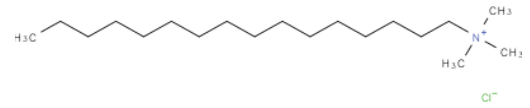

CTMA Cl

cetyltrimethylammonium chloride

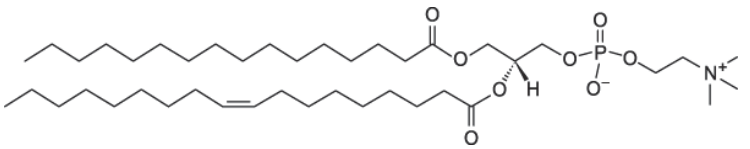

POPC

1-palmitoyl-2-oleoyl-*sn*-glycero-3-phosphocholine

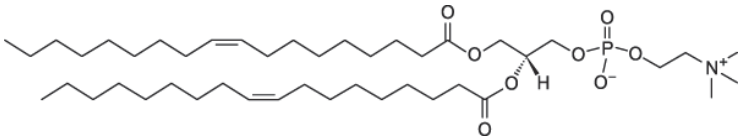

DOPC

1,2-dioleoyl-sn- glycero-3-phosphocholine

Fig. A.1: Chemical structure of chemicals mentioned in this thesis

BIBLIOGRAPHY

[1] J. D. Watson and F. H. C. Crick. Molecular Structure of Nucleic Acids: A Structure for Deoxyribose Nucleic Acid. *Nature*, 171:737, 1953.

[2] R. E. Franklin and R. G. Gosling. The structure of sodium thymonucleate fibres. I. The influence of water content. *Acta Crystallographica*, 6:673, 1953.

[3] F. DiMaio, X. Yu, E. Rensen, M. Krupovic, D. Prangishvili, and E. H. Egelman. A virus that infects a hyperthermophile encapsidates A-form DNA. *Science*, 348:914, 2015.

[4] D. R. Whelan, T. J. Hiscox, J. I. Rood, K. R. Bambery, D. McNaughton, and B. R. Wood. Detection of an en masse and reversible B- to A-DNA conformational transition in prokaryotes in response to desiccation. *Journal of The Royal Society Interface*, 11:20140454, 2014.

[5] S. C. Harvey. The scrunchworm hypothesis: Transitions between A-DNA and B-DNA provide the driving force for genome packaging in double-stranded DNA bacteriophages. *J. Struct. Biol.*, 189:1, 2015.

[6] S. C. Ha, K. Lowenhaupt, A. Rich, Y.-G. Kim, and K. K. Kim. Crystal structure of a junction between B-DNA and Z-DNA reveals two extruded bases. *Nature*, 437:1183, 2005.

[7] W. Saenger, W. N. Hunter, and O. Kennard. DNA conformation is determined by economics in the hydration of phosphate groups. *Nature*, 324:385, 1986.

[8] B. Jayaram, D. Sprous, M. A. Young, and D. L. Beveridge. Free energy analysis of the conformational preferences of A and B forms of DNA in solution. *J. Am. Chem. Soc.*, 120:10629, 1998.

[9] B. Gu, F. S. Zhang, Z. P. Wang, and H. Y. Zhou. Solvent-induced DNA conformational transition. *Phys. Rev. Lett.*, 100:088104, 2008.

[10] A. Yildirim, M. Sharma, B. M. Varner, L. Fang, and M. Feig. Conformational preferences of DNA in reduced dielectric environments. *J. Phys. Chem. B*, 118:10874, 2014.

[11] M. Falk, K. A. Hartman, and R. C. Lord. Hydration of Deoxyribonucleic Acid. II. An Infrared Study. *J. Am. Chem. Soc.*, 85:387, 1963.

[12] M. Egli, V. Tereshko, M. Teplova, G. Minasov, A. Joachimiak, R. Sanishvili, C. M. Weeks, R. Miller, M. A. Maier, H. An, Dan C. P., and M. Manoharan. X-ray crystallographic analysis of the hydration of A- and B-form DNA at atomic resolution. *Biopolymers (Nucleic Acid Sciences)*, 48:234, 1998.

[13] E Westhof. Water: An integral part of nucleic acid structure. *Annu. Rev. Biophys. Biophys. Chem.*, 17:125, 1988.

[14] I. M. Parrot, V. Laux, V. Urban, M. Haertlein, and V. T. Forsyth. X-rays and neutrons for the study of DNA structure, hydration, and transitions. *Physica B*, 385-386:848, 2006.

[15] D. Vlieghe, J. P. Turkenburg, and L. Van Meervelt. B-DNA at atomic resolution reveals extended hydration patterns. *Acta Crystallographica Section D*, 55:1495, 1999.

[16] S. Arai, T. Chatake, T. Ohhara, K. Kurihara, I. Tanaka, N. Suzuki, Z. Fujimoto, H. Mizuno, and N. Niimura. Complicated water orientations in the minor groove of the B-DNA decamer d(CCATTAATGG)$_2$ observed by neutron diffraction measurements. *Nucleic Acids Res.*, 33:3017, 2005.

[17] M. Meot-Ner (Mautner). Update 1 of: Strong Ionic Hydrogen Bonds. *Chem. Rev.*, 112:PR22, 2012.

[18] T. V. Chalikian, J. Völker, and T. P. Begley. *Nucleic Acids: Hydration*. John Wiley & Sons, Inc., 2007.

[19] B. Schneider, K. Patel, and H. M. Berman. Hydration of the phosphate group in double-helical DNA. *Biophys. J.*, 75:2422, 1998.

[20] E. Allahyarov, H. Löwen, and G. Gompper. Adsorption of monovalent and multivalent cations and anions on DNA molecules. *Phys. Rev. E*, 68:061903, 2003.

[21] S. Y. Ponomarev, K. M. Thayer, and D. L. Beveridge. Ion motions in molecular dynamics simulations on DNA. *Proc. Natl. Acad. Sci. U.S.A.*, 101:14771, 2004.

[22] T. J. Robbins, J. D. Ziebarth, and Y. Wang. Comparison of monovalent and divalent ion distributions around a DNA duplex with molecular dynamics simulation and a Poisson-Boltzmann approach. *Biopolymers*, 101:834, 2014.

[23] J. A. Subirana and M. Soler-López. Cations as hydrogen bond donors: A view of electrostatic interactions in DNA. *Annu. Rev. Biophys. Biomol. Struct.*, 32:27, 2003.

[24] T. K. Chiu and R. E. Dickerson. 1 Å crystal structures of B-DNA reveal sequence-specific binding and groove-specific bending of DNA by Magnesium and Calcium. *J. Mol. Biol.*, 301:915, 2000.

[25] R. Das, T. T. Mills, L. W. Kwok, G. S. Maskel, I. S. Millett, S. Doniach, K. D. Finkelstein, D. Herschlag, and L. Pollack. Counterion distribution around DNA probed by solution X-ray scattering. *Phys. Rev. Lett.*, 90:188103, 2003.

[26] E. Stellwagen, J. M. Muse, and N. C. Stellwagen. Monovalent cation size and DNA conformational stability. *Biochemistry*, 50:3084, 2011.

[27] R. Buchner, J. Barthel, and J. Stauber. The dielectric relaxation of water between 0° C and 35° C. *Chem. Phys. Lett.*, 306:57, 1999.

[28] D. Polley, A. Patra, and R. K. Mitra. Dielectric relaxation of the extended hydration sheathe of DNA in the THz frequency region. *Chem. Phys. Lett.*, 586:143, 2013.

[29] P. Glancy. Concentration-dependent effects on fully hydrated DNA at terahertz frequencies. *J. Biol. Phys.*, 41:247, 2015.

[30] N. Verma, S. D.and Pal, M. K. Singh, and S. Sen. Probe position-dependent counterion dynamics in DNA: Comparison of time-resolved stokes shift of groove-bound to base-stacked probes in the presence of different monovalent counterions. *J. Phys. Chem. Lett.*, 3:2621, 2012.

[31] N. Pal, H. Shweta, M. K. Singh, Sachin D. V., and S. Sen. Power-law solvation dynamics in G-quadruplex DNA: Role of hydration dynamics on ligand solvation inside DNA. *J. Phys. Chem. Lett.*, 6:1754, 2015.

[32] S. K. Pal, J. Peon, and A. H. Zewail. Biological water at the protein surface: Dynamical solvation probed directly with femtosecond resolution. *Proc. Natl. Acad. Sci. USA*, 99:1763, 2002.

[33] S. K. Pal, L. Zhao, T. Xia, and A. H. Zewail. Site- and sequence-selective ultrafast hydration of DNA. *Proc. Natl. Acad. Sci. USA*, 100:13746, 2003.

[34] Ł. Szyc, M. Yang, and T. Elsaesser. Ultrafast energy exchange via water-phosphate interactions in hydrated DNA. *J. Phys. Chem. B*, 114:7951, 2010.

[35] P. Hamm, M. Lim, and R. M. Hochstrasser. Structure of the amide I band of peptides measured by femtosecond nonlinear-infrared spectroscopy. *J. Phys. Chem. B*, 102:6123, 1998.

[36] M. L. Cowan, B. D. Bruner, N. Huse, J. R. Dwyer, B. Chugh, E. T. J. Nibbering, T. Elsaesser, and R. J. D. Miller. Ultrafast memory loss and energy redistribution in the hydrogen bond network of liquid H_2O. *Nature*, 434:199, 2005.

[37] M. Yang, Ł. Szyc, and T. Elsaesser. Decelerated water dynamics and vibrational couplings of hydrated DNA mapped by two-dimensional infrared spectroscopy. *J. Phys. Chem. B*, 115:13093, 2011.

[38] S. Pal, P. K. Maiti, and B. Bagchi. Exploring DNA groove water dynamics through hydrogen bond lifetime and orientational relaxation. *J. Chem. Phys.*, 125, 2006.

[39] S. Pal, P. K. Maiti, B. Bagchi, and J. T. Hynes. Multiple time scales in solvation dynamics of DNA in aqueous solution: The role of water, counterions, and cross-correlations. *J. Phys. Chem. B*, 110:26396, 2006.

[40] S. T. Roberts, K. Ramasesha, and A. Tokmakoff. Structural rearrangements in water viewed through two-dimensional infrared spectroscopy. *Acc. Chem. Res.*, 42:1239, 2009.

[41] D. Laage and J. T. Hynes. A molecular jump mechanism of water reorientation. *Science*, 311:832, 2006.

[42] D. Laage, G. Stirnemann, F. Sterpone, R. Rey, and J. T. Hynes. Reorientation and allied dynamics in water and aqueous solutions. *Annu. Rev. Phys. Chem.*, 62:395, 2011.

[43] D. Laage, G. Stirnemann, F. Sterpone, and J. T. Hynes. Water jump reorientation: From theoretical prediction to experimental observation. *Acc. Chem. Res.*, 45:53, 2012.

[44] A. C. Fogarty, E. Duboue-Dijon, F. Sterpone, J. T. Hynes, and D. Laage. Biomolecular hydration dynamics: a jump model perspective. *Chem. Soc. Rev.*, 42:5672, 2013.

[45] J. D. Eaves, J. J. Loparo, C. J. Fecko, S. T. Roberts, A. Tokmakoff, and P. L. Geissler. Hydrogen bonds in liquid water are broken only fleetingly. *Proc. Natl. Acad. Sci. USA*, 102:13019, 2005.

[46] E. Duboué-Dijon, A. C. Fogarty, J. T. Hynes, and D. Laage. Dynamical disorder in the DNA hydration shell. *J. Am. Chem. Soc.*, 138:7610, 2016.

[47] N. M. Levinson, E. E. Bolte, C. S. Miller, S. A. Corcelli, and S. G. Boxer. Phosphate vibrations probe local electric fields and hydration in biomolecules. *J. Am. Chem. Soc.*, 133:13236, 2011.

[48] S. Mukamel. *Principles of Nonlinear Optical Spectroscopy*. Oxford University Press, 1995.

[49] Peter Hamm. Principles of nonlinear optical spectroscopy: A practical approach or: Mukamel for dummies, 2005.

[50] V. Barone. Anharmonic vibrational properties by a fully automated second-order perturbative approach. *J. Chem. Phys.*, 122:014108, 2005.

[51] R. A. Kaindl, M. Wurm, K. Reimann, P. Hamm, A. M. Weiner, and M. Woerner. Generation, shaping, and characterization of intense femtosecond pulses tunable from 3 to 20 μm. *J. Opt. Soc. Am. B*, 17:2086, 2000.

[52] Peter Hamm; Martin Zanni. *Concepts and Methods of 2D Infrared Spectroscopy*. Cambridge University Press, 2011.

[53] L. P. DeFlores, R. A. Nicodemus, and A. Tokmakoff. Two-dimensional fourier transform spectroscopy in the pump-probe geometry. *Opt. Lett.*, 32:2966, 2007.

[54] J. Helbing and P. Hamm. Compact implementation of fourier transform two-dimensional ir spectroscopy without phase ambiguity. *J. Opt. Soc. Am. B*, 28:171, 2011.

[55] T. Zhang, C. N. Borca, X. Li, and S. T. Cundiff. Optical two-dimensional fourier transform spectroscopy with active interferometric stabilization. *Opt. Express*, 13:7432, 2005.

[56] V. Volkov, R. Schanz, and P. Hamm. Active phase stabilization in fourier-transform two-dimensional infrared spectroscopy. *Opt. Lett.*, 30:2010, 2005.

[57] U. Selig, F. Langhojer, F. Dimler, T. Löhrig, C. Schwarz, B. Gieseking, and T. Brixner. Inherently phase-stable coherent two-dimensional spectroscopy using only conventional optics. *Opt. Lett.*, 33:2851, 2008.

[58] S.-H. Shim, D. B. Strasfeld, and M. T. Zanni. Femtosecond pulse shaping directly in the mid-IR using acousto-optic modulation. *Opt. Lett.*, 31:838, 2006.

[59] S. H. Shim, D. B. Strasfeld, E. C. Fulmer, and M. T. Zanni. Generation and characterization of phase and amplitude shaped femtosecond mid-IR pulses. *Opt. Express*, 14:13120, 2006.

[60] G. D. Goodno, G. Dadusc, and R. J. D. Miller. Ultrafast heterodyne-detected transient-grating spectroscopy using diffractive optics. *J. Opt. Soc. Am. B*, 15:1791, 1998.

[61] M.L. Cowan, J.P. Ogilvie, and R.J.D. Miller. Two-dimensional spectroscopy using diffractive optics based phased-locked photon echoes. *Chem. Phys. Lett.*, 386:184, 2004.

[62] Franklin D. F. and J. P. Ogilvie. Experimental implementations of two-dimensional fourier transform electronic spectroscopy. *Annu. Rev. Phys. Chem.*, 66:667, 2015.

[63] J. D. Leger, C. M. Nyby, C. Varner, J. Tang, Na. I. Rubtsova, Y. Yue, V. V. Kireev, V. D. Burtsev, L. N. Qasim, G. I. Rubtsov, and I. V. Rubtsov. Fully automated dual-frequency three-pulse-echo 2DIR spectrometer accessing spectral range from 800 to 4000 wavenumbers. *Rev. Sci. Instrum.*, 85:083109, 2014.

[64] A. Mandal and A. Tokmakoff. Vibrational dynamics of aqueous hydroxide solutions probed using broadband 2dir spectroscopy. *J. Chem. Phys.*, 143:194501, 2015.

[65] K. Tanaka and Y. Okahata. A DNA-lipid complex in organic media and formation of an aligned cast film. *J. Am. Chem. Soc.*, 118:10679., 1996.

[66] J. R. Dwyer, Ł. Szyc, E. T. J. Nibbering, and T. Elsaesser. Note: An environmental cell for transient spectroscopy on solid samples in controlled atmospheres. *Rev. Sci. Instrum.*, 84, 2013.

[67] Y. Guan and G. J. Thomas. Vibrational analysis of nucleic acids. V. force field and conformation-dependent modes of the phosphodiester backbone modeled by diethyl phosphate. *Biophys. J.*, 71:2802, 1996.

[68] P. Carmona and M. Molina. Raman and infrared spectra of d-ribose and d-ribose 5-phosphate. *J. Raman Spectrosc.*, 21:395, 1990.

[69] Y. Guan, C.J. Wurrey, and G.J. Thomas. Vibrational analysis of nucleic acids. I. the phosphodiester group in dimethyl phosphate model compounds: $(CH_3O)_2PO_2^-$, $(CD_3O)_2PO_2^-$, and $(^{13}CH_3O)_2PO_2^-$. *Biophys. J.*, 66:225, 1994.

[70] Y. Guan and G. J. Thomas. Vibrational analysis of nucleic acids. III. conformation-dependent raman markers of the phosphodiester backbone modeled by dimethyl phosphate. *J. Mol. Struct.*, 379:31, 1996.

[71] V. Andrushchenko, H. Wieser, and P. Bouř. B-Z conformational transition of DNA monitored by vibrational circular dichroism. ab initio interpretation of the experiment. *J. Phys. Chem. B*, 106:12623, 2002.

[72] V. Andrushchenko, L. Benda, O. Páv, M. Dračínský, and P. Bouř. Vibrational properties of the phosphate group investigated by molecular dynamics and density functional theory. *J. Phys. Chem. B*, 119:10682, 2015.

[73] C. Greve, E. T. J. Nibbering, and H. Fidder. Hydrogen-bonding-induced enhancement of Fermi resonances: A linear IR and nonlinear 2D-IR study of aniline-d_5. *J. Phys. Chem. B*, 117:15843, 2013.

[74] M. Yang, Ł. Szyc, K. Röttger, H. Fidder, E. T. J. Nibbering, T. Elsaesser, and F. Temps. Dynamics and couplings of N-H stretching excitations of guanosine-cytidine base pairs in solution. *J. Phys. Chem. B*, 115:5484, 2011.

[75] Ł. Szyc, M. Yang, E. T. J. Nibbering, and T. Elsaesser. Ultrafast vibrational dynamics and local interactions of hydrated DNA. *Angew. Chem. Int. Ed.*, 49:3598, 2010.

[76] A. T. Krummel, P. Mukherjee, and M. T. Zanni. Inter and intrastrand vibrational coupling in DNA studied with heterodyned 2D-IR spectroscopy. *J. Phys. Chem. B*, 107:9165, 2003.

[77] A. T. Krummel and M. T. Zanni. Interpreting dna vibrational circular dichroism spectra using a coupling model from two-dimensional infrared spectroscopy. *J. Phys. Chem. B*, 110:24720, 2006.

[78] A. T. Krummel and M. T. Zanni. Evidence for coupling between nitrile groups using DNA templates: A promising new method for monitoring structures with infrared spectroscopy. *J. Phys. Chem. B*, 112:1336, 2008.

[79] R. Costard, T. Tyborski, B. P. Fingerhut, and T. Elsaesser. Ultrafast phosphate hydration dynamics in bulk H_2O. *J. Chem. Phys.*, 142:212406, 2015.

[80] R. Costard, I. A. Heisler, and T. Elsaesser. Structural dynamics of hydrated phospholipid surfaces probed by ultrafast 2D spectroscopy of phosphate vibrations. *J. Phys. Chem. Lett.*, 5:506, 2014.

[81] T. Siebert, B. Guchhait, Y. Liu, R. Costard, and T. Elsaesser. Anharmonic backbone vibrations in ultrafast processes at the DNA-water interface. *J. Phys. Chem. B*, 119:9670, 2015.

[82] T. Siebert, B. Guchhait, Y. Liu, B. P. Fingerhut, and T. Elsaesser. Range, magnitude, and ultrafast dynamics of electric fields at the hydrated DNA surface. 7:3131, 2016.

[83] S. Park, K. Kwak, and M.D. Fayer. Ultrafast 2d-ir vibrational echo spectroscopy: a probeof molecular dynamics. *Laser Phys. Lett.*, 4(10):704, 2007.

[84] D. E. Rosenfeld and M. D. Fayer. Excitation transfer induced spectral diffusion and the influence of structural spectral diffusion. *J. Chem. Phys.*, 137(6):064109, 2012.

[85] S. J. Strickler and R. A. Berg. Relationship between absorption intensity and fluorescence lifetime of molecules. *The Journal of Chemical Physics*, 37(4):814–822, 1962.

[86] H. R. Drew, R. M. Wing, T. Takano, C. Broka, S. Tanaka, K. Itakura, and R. E. Dickerson. Structure of a b-dna dodecamer: conformation and dynamics. *Proc. Natl. Acad. Sci. USA*, 78:2179, 1981.

[87] S. Sen, D. Andreatta, S. Y. Ponomarev, D. L. Beveridge, and M. A. Berg. Dynamics of water and ions near DNA: Comparison of simulation to time-resolved stokes-shift experiments. *J. Am. Chem. Soc.*, 131:1724, 2009.

[88] S. K. Pal, Liang Zhao, and Ahmed H. Zewail. Water at DNA surfaces: Ultrafast dynamics in minor groove recognition. *Proc. Natl. Acad. Sci. USA*, 100:8113, 2003.

[89] K. E. Furse and S. A. Corcelli. The dynamics of water at DNA interfaces: Computational studies of Hoechst 33258 bound to DNA. *J. Am. Chem. Soc.*, 130:13103, 2008.

[90] K. E. Furse and S. A. Corcelli. Molecular dynamics simulations of DNA solvation dynamics. *J. Phys. Chem. Lett.*, 1:1813, 2010.

[91] B. Guchhait, Y. Liu, T. Siebert, and T. Elsaesser. Ultrafast vibrational dynamics of the DNA backbone at different hydration levels mapped by two-dimensional infrared spectroscopy. *Structural Dynamics*, 3:043202, 2016.

[92] B. Pullman, A. Pullman, and H. Berthod. SCF ab initio study of the "through-water" versus "direct" binding of the Na^+ and Mg^{2+} cations to the phosphate anion. *Int. J. Quantum Chem.*, 14:79, 1978.

[93] M. A. Young, G. Ravishanker, and D. L. Beveridge. A 5-nanosecond molecular dynamics trajectory for B-DNA: analysis of structure, motions, and solvation. *Biophys. J.*, 73:2313, 1997.

[94] P. Mark and L. Nilsson. Structure and dynamics of the TIP3p, SPC, and SPC/E water models at 298 K. *J. Phys. Chem. A*, 105:9954, 2001.

[95] K. E. Furse and S. A. Corcelli. Dynamical signature of abasic damage in DNA. *J. Am. Chem. Soc.*, 133:720, 2011.

[96] S. W. Kowalczyk, D. B. Wells, A. Aksimentiev, and C. Dekker. Slowing down dna translocation through a nanopore in lithium chloride. *Nano Lett.*, 12:1038, 2012.

[97] J. Yoo and A. Aksimentiev. Competitive binding of cations to duplex dna revealed through molecular dynamics simulations. *J. Phys. Chem. B*, 116:12946, 2012.

[98] A. Beneduci. Which is the effective time scale of the fast debye relaxation process in water? *J. Mol. Liq.*, 138:55, 2008.

[99] S. Ashihara, N. Huse, A. Espagne, E. T. J. Nibbering, and T. Elsaesser. Ultrafast structural dynamics of water induced by dissipation of vibrational energy. *J. Phys. Chem. A*, 111:743, 2007.

[100] Y. Maréchal. The molecular structure of liquid water delivered by absorption spectroscopy in the whole IR region completed with thermodynamics data. *J. Mol. Struct.*, 1004:146, 2011.

[101] C. Greve, N. K. Preketes, H. Fidder, R. Costard, B. Koeppe, I. A. Heisler, S. Mukamel, F. Temps, E. T. J. Nibbering, and T. Elsaesser. N-H stretching excitations in adenosine-thymidine base pairsin solution: Pair geometries, infrared line shapes, and ultrafast vibrational dynamics. *J. Phys. Chem. A*, 117:594, 2013.

[102] H. Fidder, M. Yang, E. T. J. Nibbering, T. Elsaesser, K. Röttger, and F. Temps. N-H stretching vibrations of Guanosine-Cytidine base pairs in solution: Ultrafast dynamics, couplings, and line shapes. *J. Phys. Chem. A*, 117:845, 2013.

[103] J. R. Dwyer, Ł. Szyc, E. T. J. Nibbering, and T. Elsaesser. Ultrafast vibrational dynamics of adenine-thymine base pairs in DNA oligomers. *J. Phys. Chem. B*, 112:11194, 2008.

[104] V. Kozich, Ł. Szyc, E.T.J. Nibbering, W. Werncke, and T. Elsaesser. Ultrafast redistribution of vibrational energy after excitation of NH stretching modes in DNA oligomers. *Chem. Phys. Lett.*, 473:171, 2009.

LIST OF PUBLICATIONS

[1] Y. Liu, B. Guchhait, T. Siebert, B. P. Fingerhut, and T. Elsaesser. Molecular couplings and energy exchange between dna and water mapped by femtosecond infrared spectroscopy of backbone vibrations. *Structural Dynamics*, 4:044015, 2017.

[2] B. Guchhait, Y. Liu, T. Siebert, and T. Elsaesser. Ultrafast vibrational dynamics of the DNA backbone at different hydration levels mapped by two-dimensional infrared spectroscopy. *Structural Dynamics*, 3:043202, 2016.

[3] T. Siebert, B. Guchhait, Y. Liu, B. P. Fingerhut, and T. Elsaesser. Range, magnitude, and ultrafast dynamics of electric fields at the hydrated DNA surface. *J. Phys. Chem. Lett.*, 7:3131, 2016.

[4] T. Siebert, B. Guchhait, Y. Liu, R. Costard, and T. Elsaesser. Anharmonic backbone vibrations in ultrafast processes at the DNA-water interface. *J. Phys. Chem. B*, 119:9670, 2015.

[5] B. Guchhait, Y. Liu, T. Siebert, and T. Elsaesser. Hydration of native DNA: Ultrafast structural dynamics and short-range electric fields. In *International Conference on Ultrafast Phenomena*, page UM4A.5. Optical Society of America, 2016.

Declaration of Authorship

I declare that I have completed the thesis independently using only the aids and tools specified. I have not applied for a doctor's degree in the doctoral subject elsewhere and do not hold a corresponding doctor's degree. I have taken due note of the Faculty of Mathematics and Natural Sciences PhD Regulations, published in the Official Gazette of Humboldt-Universität zu Berlin No.17/2012 on 27/06/2012.

Yingliang Liu

Berlin, May 30, 2017